Spring 5-15-2014

Modeling and Development of Iterative Reconstruction Algorithms in Emerging X-ray Imaging Technologies

Jiaofeng Xu
Washington University in St. Louis

Washington University in St. Louis

School of Engineering and Applied Science

Department of Biomedical Engineering

Dissertation Examination Committee:
Mark Anastasio, Chair
Viktor Gruev
Lihong Wang
Mladen Victor Wickerhauser
Deshan Yang

Modeling and Development of Iterative Reconstruction Algorithms in Emerging X-ray Imaging Technologies

by

Jiaofeng Xu

A dissertation presented to
the Graduate School of Arts & Sciences
of Washington University in partial fulfillment of the
requirements for the degree of
Doctor of Philosophy

May 2014

Saint Louis, Missouri

Contents

List of Figures . . . . . **vi**

Acknowledgments . . . . . **xiii**

Abstract . . . . . **xvi**

1 Introduction **1**
1.1 Background and Motivation 1
1.1.1 Differential phase-contrast imaging 1
1.1.2 Grating-based phase-contrast imaging 3
1.1.3 Spectral CT (K-edge imaging) 3
1.1.4 Cone-beam computed tomography 4
1.1.5 In-line phase-contrast tomosynthesis 5
1.2 Overview of the Dissertation 6

2 Investigation of discrete imaging models and iterative image reconstruction in DPCT **8**
2.1 Introduction 8
2.2 Background 10
2.2.1 Data function and imaging model in continuous form 10
2.2.2 General forms of discrete imaging models 12
2.3 Construction of system matrices for iterative image reconstruction in DPCT 14
2.3.1 System matrix construction employing pixel basis functions 14
2.3.2 System matrix construction employing generalized Kaiser-Bessel window functions 16
2.4 Comparison of numerical and statistical properties of system matrices 18
2.4.1 SVD analysis of the system matrices 18
2.4.2 Simulation data and image reconstruction algorithm 21
2.4.3 Empirical determination of image statistics and resolution measures . 25
2.5 Application to few-view image reconstruction 28
2.5.1 Experimental data and image reconstruction algorithm 28
2.5.2 Reconstructed images 29
2.6 Summary 31

3 A multi-channel image reconstruction method for grating-based X-ray phase-contrast computed tomography . . . 35
3.1 Introduction . . . 35
3.2 Basic principles of GB-XPCT . . . 36
3.3 Methods . . . 38
3.3.1 Discrete imaging models for GB-XPCT . . . 38
3.3.2 Interpretation of GB-XPCT as a MC reconstruction problem . . . 42
3.3.3 Description of MC image reconstruction methods . . . 43
3.3.4 Methods for estimating the MC sinogram covariance . . . 45
3.4 Results . . . 45
3.4.1 Measurement data . . . 45
3.4.2 Absorption channel results . . . 46
3.4.3 Darkfield channel . . . 48
3.4.4 Phase channel . . . 52
3.5 Summary and conclusion . . . 56

4 Sparsity-Regularized Image Reconstruction of Decomposed K-Edge Data in Spectral CT . . . 57
4.1 Introduction . . . 57
4.2 Materials and Methods . . . 58
4.2.1 PWLS Image Reconstruction with TV and ℓ_1-norm Regularization . . . 58
4.2.2 Computer-Simulation Studies . . . 60
4.2.3 Assessment of spatial resolution and noise properties . . . 62
4.2.4 Quantitative measurement of different reconstruction algorithms performance . . . 63
4.2.5 Phantom Experiment with Targeted Ytterbium-Nanoparticles . . . 63
4.3 Computer-Simulation Studies . . . 64
4.3.1 Spatial resolution and noise properties . . . 64
4.3.2 Qualitatively assesments . . . 65
4.3.3 SSIM comparison between PWLS-TV and PWLS-TV-ℓ1 . . . 67
4.3.4 Different number of views results for FBP and proposed PWLS-TV-ℓ1 . . . 68
4.4 Phantom Experiment with Targeted Ytterbium-Nanoparticles . . . 71
4.5 Summary . . . 73

5 Accelerated fast iterative shrinkage thresholding algorithms for sparsity-regularized cone-beam CT image reconstruction with ordered subsets . . . 75
5.1 Introduction . . . 75
5.2 Background . . . 77
5.2.1 Discrete imaging model for CBCT . . . 77
5.2.2 PLS image reconstruction using sparsity-promoting penalties . . . 77

5.2.3 FISTA for solving the PLS-TV problem . . . 78
5.2.4 Splitting-based FISTA for solving the PLS-TV-ℓ1 problem . . . 79
5.3 Accelerated FISTAs for image reconstruction in CBCT . . . 80
5.3.1 Motivation and preconditioned ordered subsets acceleration strategies 80
5.3.2 Some technical implementaion details . . . 84
5.4 Computer-simulation studies . . . 86
5.4.1 Numerical phantom and simulated projection data . . . 87
5.4.2 Full-view (360-view) case: Example images and corresponding error maps . . . 89
5.4.3 Sparse-view (45-view) case: Example images and corresponding error maps . . . 89
5.4.4 Convergence and accuracy curves . . . 90
5.4.5 Reconstruction time by using GPUs . . . 93
5.5 Confirmation of algorithm performance using clinical data . . . 93
5.5.1 Experimental data and image reconstruction . . . 94
5.5.2 Demonstration of rapid convergence rate with experimental data . . . 96
5.6 Discussion . . . 98
5.6.1 Convergence rate compared to some previous works . . . 98
5.6.2 Computation complexity and reconstruction time . . . 101
5.6.3 Other recently published OS-type accelerating iterative algorithms with regularizations . . . 102
5.7 Summary and conclusion . . . 103

6 Investigation of in-line X-ray phase-contrast tomosynthesis using an advanced iterative algorithm . . . 105
6.1 Introduction . . . 105
6.2 Background . . . 107
6.2.1 XPC imaging model . . . 107
6.2.2 OS-SART-FISTA-TV (OSSF-TV) iterative algorithm . . . 109
6.2.3 Fourier analysis of XPC tomosynthesis . . . 110
6.3 Descriptions of numerical and experimental studies . . . 111
6.3.1 Computer-Simulation Studies Descriptions . . . 111
6.3.2 Experimental Studies Descriptions . . . 112
6.4 Computer simulation results . . . 114
6.4.1 In-plane image evaluation . . . 114
6.4.2 In-depth image evaluation . . . 114
6.5 Experimental studies . . . 115
6.5.1 In-plane image evaluation . . . 115
6.5.2 Z-resolution property of XPC tomosynthesis . . . 115

6.6 Conclusion and discussion 117

7 Summary 119
7.1 Differential phase-contrast imaging 119
7.2 Grating-based phase-contrast imaging 120
7.3 Spectral-CT (K-edge imaging) 120
7.4 Cone-beam computed tomography 121
7.5 In-line phase-contrast tomosynthesis 122

Appendix A Explicit construction of the pixel-based system matrices . . 123

Appendix B The derivation of Eq.(2.18) in Sec. 2.3.2 126

Appendix C Desription of the FGP algorithm for the 3D case in Sec. 5.2.3 127

Appendix D Description of FISTA-ℓ_1 algorithm for wavelet-ℓ_1 penalty in Sec. 5.2.4 130

Appendix E Hardware acceleration employing single and multiple GPUs in Sec. 5.3.2 132
E.1 Single GPU implementation of the OSSF-TV algorithm for CBCT 132
E.2 Multi-GPU implementation of the OSSF-TV algorithm for CBCT 134

References 138

List of Figures

2.1 A schematic of differential phase-contrast imaging tomography. The black box represents the system of optical elements that is specific to the implementation. 10
2.2 Singular value spectra associated with the system matrices H^{pixel} with pixel size 50μm. 19
2.3 Singular value spectra associated with the system matrices H^{blob} with $m = 2$, relative radius a = 1.5 (physical size 75μm). 20
2.4 Singular value spectra associated with the system matrices H^{blob} with $m = 2$, relative radius a = 2 (physical size 100μm). 20
2.5 Profiles of the differential projection value of one blob with $m = 2$, relative radius a = 2. 21
2.6 The three highest singular value spectra are replotted for comparison. Two of the spectra correspond to H^{blob} with $\alpha = 10.4$, relative radius a = 1.5 and a = 2. The third spectra corresponds to H^{pixel} based on the linear weighting kernel. 22
2.7 The numerical phantom employed in our simulation studies with an ROI indicated 23
2.8 Examples of reconstructed images by use of PLS algorithms based on pixel system matrix H^{pixel} and blob system matrix H^{blob}. Regularization parameter $\gamma = 10$ for both cases. (a) An reconstructed image produced by pixel system matrix with linear interpolation . (b) An reconstructed image produced by blobs with relative radius a = 2 (physical size 100μm), $m = 2$ and $\alpha = 10.4$. 24
2.9 (Color online) Profiles through the center row of the reconstructed images in Fig. 2.8. The solid blue line corresponds to Fig.2.8-(a). The dashed red and dashdotted black lines correspond to Fig.2.8-(b) and the true phantom. . . . 25
2.10 Variance versus resolution curves corresponding to use of the system matrices H^{pixel}. 26
2.11 Variance versus resolution curves corresponding to use of the system matrices H^{blob}. (a) Curves are produced by blobs with relative radius $a = 1.5$ (physical size 75μm), $m = 2$ and varying α. (b) Curves are produced by blobs with relative radius $a = 2$ (physical size 100μm), $m = 2$ and varying α. 27
2.12 The three best variance-resolution curves picked from the pixel and blob cases. 28
2.13 Images reconstructed from 90 projections by use of the (a) FBP (b) ASD-POCS algorithm. The dashed boxes indicate two ROIs chosen for comparison. All images are displayed in the same grey scale window [0 1]. 30

2.14 Images reconstructed from 180 projections by use of the (a) FBP (b) ASD-POCS algorithm Two dashed boxes indicate two ROIs chosen for comparison. All images are displayed in the same grey scale window [0 1]. 31
2.15 Zoomed-in images of the smaller ROIs denoted in Figs. 2.13-(a) and (b), reconstructed from 90 view angles, are displayed in subfigures (a) and (b). Subfigure (c) displays the corresponding reference ROI corresponding to an image reconstructed from 720 projections by use of a DPCT FBP algorithm. All images are displayed in the same grey scale window [0 1] 32
2.16 Zoomed-in images of the smaller ROIs denoted in Figs. 2.14-(a) and (b), reconstructed from 180 view angles, are displayed in subfigures (a) and (b). Subfigure (c) displays the corresponding reference ROI corresponding to an image reconstructed from 720 projections by use of a DPCT FBP algorithm. All images are displayed in the same grey scale window [0 1] 32
2.17 Zoomed-in images of the larger ROIs denoted in Figs. 2.13-(a) and (b), reconstructed from 90 view angles, are displayed in subfigures (a) and (b). Subfigure (c) displays the corresponding reference ROI corresponding to an image reconstructed from 720 projections by use of a DPCT FBP algorithm. All images are displayed in the same grey scale window [0 1] 33
2.18 Zoomed-in images of the larger ROIs denoted in Figs. 2.14-(a) and (b), reconstructed from 180 view angles, are displayed in subfigures (a) and (b). Subfigure (c) displays the corresponding reference ROI corresponding to an image reconstructed from 720 projections by use of a DPCT FBP algorithm. All images are displayed in the same grey scale window [0 1]. 33

3.1 A schematic of grating-based phase-contrast imaging system. 37
3.2 Examples of reconstruced absorption images by FBP method for "noise-free" and "noisy" sinograms. (a) Reference image reconstructed by FBP method from noise-free projection data; (b) Noisy image reconstructed by FBP method from noisy projection data; (c) SSIM mapping for the noisy FBP image when compared to the reference image; 46
3.3 Mean SSIM curves for the absorption channel: MSSIM values as a function of regularization parameters λ. The curves are parametrized by the regularization parameter. (a) Produced by PLS-TV (without noise property) case, (b) Produced by PWLS-TV-SC (dashed curve) and PWLS-TV-MC (solid curve) case. 47
3.4 Examples of absorption images reconstructed by PLS-TV, PWLS-TV-SC and PWLS-TV-MC method with different regularization values. *First Row:* Images produced by PLS-TV method without variance; *Second Row:* Images produced by PWLS-TV-SC method; *Third Row:* Images produced by PWLS-TV-MC method. All images are displayed in the same window. 48
3.5 SSIM images and MSSIM values corresponding to the images in Fig.3.4. All images are dispaly in the same window [0 1]. 49

3.6 Examples of reconstruced darkfield (scattering) images by FBP method for "noise-free" and "noisy" sinograms. (a) Reference image reconstructed by the FBP method from noise-free projection data; (b) Noisy image reconstructed by FBP method from noisy projection data; (c) SSIM mapping for the noisy FBP image when compared to the reference image; 50
3.7 Mean SSIM curves for the darkfield channel: MSSIM values as a function of regularization parameters λ. The curves are parametrized by the regularization parameter. (a) Produced by PLS-TV (without noise property) case, (b) Produced by PWLS-TV-SC (dashed curve) and PWLS-TV-MC (solid cuve) case. 50
3.8 Examples of darkfield images reconstructed by PLS-TV, PWLS-TV-SC and PWLS-TV-MC method with different regularization values. *First Row:* Images produced by PLS-TV method without variance ; *Second Row:* Images produced by PWLS-TV-SC method; *Third Row:* Images produced by PWLS-TV-MC method. All images are displayed in the same window. 51
3.9 SSIM images and MSSIM values corresponding to the images in Fig.3.8. All images are displayed in a window [0 1]. 52
3.10 Examples of reconstruced phase images by FBP method for "noise-free" and "noisy" sinograms. (a) Reference image reconstructed by FBP method from noise-free projection data; (b) Noisy image reconstructed by FBP method from noisy projection data; (c) SSIM mapping for the noisy FBP image when compared to the reference image; 53
3.11 Mean SSIM curves for the phase channel: MSSIM values as a function of regularization parameters λ. The curves are parametrized by the regularization parameter. (a) Produced by PLS-TV (without noise property) case, (b) Produced by PWLS-TV-SC (dashed curve) and PWLS-TV-MC (solid cuve) case. 53
3.12 Examples of phase images reconstructed by PLS-TV, PWLS-TV-SC and PWLS-TV-MC method with different regularization values. *First Row:* Images produced by PLS-TV method without variance; *Second Row:* Images produced by PWLS-TV-SC method; *Third Row:* Images produced by PWLS-TV-MC method. All images are displayed in the same window. 54
3.13 SSIM images and MSSIM values corresponding to the images in Fig.3.12. All images are displayed in a window [0 1]. 55

4.1 The numerical phantom employed in the computer-simulation studies is shown in the left panel and is described in the text. The right panel displays a zoomed-in image of the ytterbium inserts contained within the white box in the left panel. 61

4.2 Physical Phantom Experiment: (a) Conventional CT reconstruction of the physical phantom using a standard filtered backprojection (FBP) algorithm. (b) Decomposed K-edge (ytterbium) sinogram. (c) The estimated sinogram variance. 62
4.3 Computer-simulation studies: Ensemble variances as a function of spatial resolution (FWHM) for different undersampling factors. The curves are parametrized by the regularization parameter. FWHM values are evaluated in horizontal (black) and vertical (gray) orientation at positions shown in Fig. 4.1. The PWLS-TV results (solid) show an improved noise-resolution performance compared to PLS-TV (dashed). 64
4.4 Computer-simulation studies: Examples of reconstructed K-edge images ROIs for the 200-view case corresponding to different regularization parameter values. All images are cropped to size of 300×300 pixels and are displayed in the same grey-scale window. Images reconstructed via PLS-TV (a-d), PWLS-TV (e-h) and PWLS-TV-ℓ_1 (i-h). 65
4.5 Three zoomed-in ROIs of true phantom and corresponding reconstructed images from Fig. 4.4. Each column was obtained from the oringial phantom or one particular reconstructed image, which is indicated by the name shown in first row. All images were displayed in the same grey-scale window. 66
4.6 SSIM images and MSSIM values corresponding to the images in Fig.4.4 (e)-(h) reconstructed by use of the PWLS-TV method are shown in subfigures (a)-(d), respectively. SSIM images and MSSIM values corresponding to the images in Fig.4.4 (i)-(l) reconstructed by use of the PWLS-TV-ℓ_1 method are shown in subfigures (e)-(h), respectively. All images are displayed in the same window [0 1]. 68
4.7 Examples of reconstructed K-edge images via FBP algorithm (a-d) and PWLS-TV-ℓ1 algorithm by use of 100 views (e-h), 200 views (i-l) and 400 views (m-p). All images are displayed in the same window. 69
4.8 SSIM images and MSSIM values corresponding to the images in Fig.4.7 (e)-(h) reconstructed by use of the PWLS-TV-ℓ_1 method with 100 views, are shown in subfigures (a)-(d); SSIM images and MSSIM values corresponding to the images in Fig.4.7 (i)-(l) reconstructed by use of the PWLS-TV-ℓ_1 method with 200 views, are shown in subfigures (e)-(h); SSIM images and MSSIM values corresponding to the images in Fig.4.7 (m)-(p) reconstructed by use of the PWLS-TV-ℓ_1 method with 400 views, are shown in subfigures (i)-(l). All images are displayed in the same window [0 1]. 70
4.9 Physical Phantom Experiment: Reconstructed images of the K-edge material by use of FBP algorithm for 125, 625 and 1250 projection views, respectively. All images are displayed in the same grey-scale window. 71

4.10 Physical Phantom Experiment: Reconstructed images of the K-edge material from 125 projection views. Image reconstructed by use of the PLS-TV method (a-c), PWLS-TV method (d-f), and PWLS-TV-ℓ_1 method (g-i). The arrow in subfigure (b) indicates the tube containing the low-concentration, ytterbium dilution, which becomes more visible in the images estimated by use of the PWLS methods. All images are displayed in the same grey-scale window. . . 72
4.11 Physical Phantom Experiment: Reconstructed images of the K-edge material from 625 projection views. Image reconstructed by use of the PLS-TV method (a-c), PWLS-TV method (d-f), and PWLS-TV-ℓ_1 method (g-i). The arrow in subfigure (b) indicates the tube containing the low-concentration, ytterbium dilution, which becomes more visible in the images estimated by use of the PWLS methods. All images are displayed in the same grey-scale window. . . 73

5.1 NCAT numerical phantom study for the full-view (360-view) case. Examples of images reconstructed by use of the FISTA-TV (top row), OSSF-TV-1-1 (middle row) and OSSF-TV-1-4 (bottom row) algorithms are displayed. Ten algorithm iterations were employed in all cases. 87
5.2 Error maps corresponding to the images displayed in Fig. 5.1. 88
5.3 NCAT numerical phantom study for the sparse-view (45 view) case. Examples of images reconstructed by use of the FISTA-TV (top row), OSSF-TV-1-1 (middle row) and OSSF-TV-1-4 (bottom row) algorithms are displayed. Thirty algorithm iterations were employed in all cases. 90
5.4 Error maps corresponding to the images displayed in Fig. 5.3. 91
5.5 Convergence analysis: Plots of the objective function value as a function of iteration number for the FISTA-TV and OSSF-TV algorithms for the (a) full-view (360-view) case and (b) few-view (45-view) case. 92
5.6 Accuracy analysis: Plots of the image RE as a function of iteration number for the FISTA-TV and OSSF-TV algorithms for the (a) full-view case and (b) few-view case. 92
5.7 Plots of image RE as a function of reconstruction time for (a) full-view case with one GPU, (b) few-view case with one GPU; (c) full-view case with four GPUs, and (d) few-view case with four GPUs; 94
5.8 Example images corresponding to three orthogonal planes reconstructed by a Varian imager system and in-house FDK algorithm. First row: image reconstructed by Varian imager system, Second row: image reconstructed by our in-house FDK algorithm with a simple ramp filter. The transverse images are shown in a soft-tissue window [-300 200]HU. The sagittal and frontal images are shown in a display window [-500 800]HU. 95
5.9 Reference images reconstructed by the standard FISTA-TV (converged) and FISTA-TV-ℓ_1 (converged). First row: reconstructed by standard FISTA-TV algorithm. Second row: reconstructed by the standard FISTA-TV-ℓ_1 algorithm. 96

5.10 Example images corresponding to different iteration numbers (K) for the OSSF-TV algorithm. First Column: the selected transverse slice with soft-tissue display window [-300 200]HU, Second column:the selected sagittal plane with display window [-500 800]HU, Third column: the chosen frontal plane with display window [-500 800]HU. 97
5.11 Error maps corresponding to different iteration numbers (K) for the OSSF-TV algorithm. The display window was [-50 50]HU. First Column: error maps for the selected transverse slice, Second column: error maps for the selected sagittal plane, Third column: error maps for the selected frontal plane. The reference image was produced by running the standard FISTA-TV until convergence. 98
5.12 Example images corresponding to different iteration numbers (K) for the OSSF-TV-ℓ_1 algorithm. First Column: the selected transverse slice with soft-tissue display window [-300 200]HU, Second column:the selected sagittal plane with display window [-500 800]HU, Third column: the chosen frontal plane with display window [-500 800]HU. 99
5.13 Error maps corresponding to different iteration numbers (K) for the OSSF-TV-ell_1 algorithm. The display window was [-50 50]HU. First Column: error maps for the selected transverse slice, Second column: error maps for the selected sagittal plane, Third column: error maps for the selected frontal plane. The reference image was produced by running the FISTA-TV-ℓ_1 algorithm until convergence. 100

6.1 A schematic of the XPC imaging geometry is shown in which the object is fixed in a reference coordinate system (x, y, z). The source (not shown) and detector rotate about the y-axis. 107
6.2 A frequency domain interpretation of tomosynthesis illustrates the reduced spatial resolution in the z-direction of reconstructed images. The shaded region indicates spectral information content of tomosynthesis measurements in the k_x and k_z plane. Region A indicates the (low) frequency information in k_z that is not contained in the measured data. Region B illustrates the preservation of some high frequency components in k_z. 107
6.3 The numerical phantom we employed to investigate XPC tomosynthesis is shown (top view). Diameters of internal spheres range from $80\mu m$ to $160\mu m$. 112
6.4 This figure illustrates the tomosynthesis scanning configuration used in the study. The detector and source rotate about the fixed phantom covering a limited angular range. 112
6.5 The polychromatic spectrum used as input in the tomosynthesis simulations is shown. The y-axis gives the normalized weight for each energy bin. . . . 112

6.6 Comparison of reconstructed in-plane images (top row) and associated profiles (bottom row). (a)The line profiles from conventional tomosynthesis result show similar signals from all internal spheres. (b) The XPC tomosynthesis result reveals edge-enhancement for some of the internal spheres. (c) The true in-plane phantom structure shows that only the edge-enhanced spheres in (b) are actually located in that plane. 113
6.7 The reconstructed in-depth images are given for conventional (panel a) and XPC (panel c) tomosynthesis scans of the phantom shown in Fig 6.3. The dotted regions in (a) and (c) are shown with a close-up view in panels (b) and (d), respectively.The arrows indicate the extent of blur from image features for each case. 115
6.8 Reconstruction for experimental data: extracted mouse lung. CT reconstruction used 200 projections with the angular step of 1 degree; tomosynthesis reconstruction used 40 projections with the angular step of 1 degree. Voxel size: 28 μm 116
6.9 SSIM map for the reconstructed tomosynthesis images. 117
6.10 Experimental studies: comparison of the reconstructed in-planes images between the two types of tomosynthesis in terms of depth resolution. Two branch airways were specified and profiles are ploted to show the presence of edge enhancment. CT reconstruction used 100 projections with the angular step of 2 degrees; tomosynthesis reconstruction used 20 projections with the angular step of 3 degrees. Voxel size: 28 μm 118

E.1 A simple flowchart of the OSSF-TV algorithm with single GPU approach . 133
E.2 One simple scheme of four GPUs implementation for OS-SART part in porposed OSSF-TV and/or OSSF-TV-ℓ_1 algorithms 135

Acknowledgments

First and foremost, I would like to thank my Ph.D. advisor, Professor Mark Anastasio, for supporting me during my Ph.D. study. He is the one who taught me to be a good researcher possessing rigorous thoughts in the medical imaging field. He has been always lively, enthusiastic, and energetic and willing to discuss research projects with me over the past few years. Under his supervision and mentorship, I have learnt how to analyze, design, and evaluate algorithms in most emerging X-ray imaging technologies. In addtion, he has been supportive and has given me the freedom to pursue various projects without objection. I am also very grateful for his scientific advice and knowledge and many insightful discussions and suggestions. He is my primary resource for getting my academic questions answered. I appreciate all his contributions of time, ideas, and funding to make my Ph.D. experience productive and stimulating. The joy and enthusiasm he has for his research was contagious and motivated for me, even during tough times in my Ph.D. pursuit. I am also thankful for the excellent example he has provided as a successful professor.

I would also like to thank other members of my Ph.D. committee, Dr. Lihong Wang, Dr. Miaden Wicikerhauser, Dr. Viktor Gruev, and Dr. Deshan Yang for their helpful career advice and suggestions for my research projects. I would also like to especially thank Dr. Lihong Wang for his personal career advice on several occasions. I would also like to especially thank Dr. Desheng Yang as one of my committee members and also a collaborator for providing patient data and his insightful and inspiring comments on cone-beam computed tomography.

I would also like to thank everyone who taught me in Chicago and helped me have a smooth transition from Chicago to St. Louis, including Professor Vincent Turitto, Professor Miles Wernick, Professor Frank Yin, Ms. Karen Teasdake, and Mr. Glen Reitz.

I would also like to thank some former senior labmates, Dr. Jin Zhang, Dr. Daxin Shi, and Dr. Yin Huang, for their friendly help when I started my journey in Dr. Anastasio group. I would like to thank Dr. Jin Zhang for his arrangement of my accommodations when I landed in Chicago for the first time from China. I would like to thank Dr. Yin Huang for her kind help and advice in my daily life. I would like to especially thank Dr. Daxin Shi for his

practical suggestions on how to successfully complete a Ph.D. program. More importantly, he was the one who trained and guided me early in my research life.

I would also like to thank Dr. Robert W. Schoonover, Dr. Adam Zysk, Dr. Kun Wang, Dr. Xiaofeng Niu, Mr. Chao Huang, and Mr. Wenyuan Qi for their insightful discussions and collaborations on many research projects.

Lastly, I would like to thank my family for all their love and encouragement, especially for my parents who raised me with a love of science and supported me in all my pursuits. I could not have made it this far without my loving, supportive, and encouraging parents during my Ph.D. time. Thank you.

Jiaofeng Xu

Washington University in Saint Louis
May 2014

I dedicate this thesis to
my parents and my family
for their constant support and unconditional love.
I love you all dearly.

ABSTRACT OF THE DISSERTATION

Modeling and Development of Iterative Reconstruction Algorithms
in Emerging X-ray Imaging Technologies

by

Jiaofeng Xu

Doctor of Philosophy in Biomedical Engineering

Washington University in St. Louis, May 2014

Professor Mark Anastasio, Chair

Many new promising X-ray-based biomedical imaging technologies have emerged over the last two decades. Five different novel X-ray based imaging technologies are discussed in this dissertation: differential phase-contrast tomography (DPCT), grating-based phase-contrast tomography (GB-PCT), spectral-CT (K-edge imaging), cone-beam computed tomography (CBCT), and in-line X-ray phase contrast (XPC) tomosynthesis. For each imaging modality, one or more specific problems prevent them being effectively or efficiently employed in clinical applications have been discussed. Firstly, to mitigatethe long data-acquisition times and large radiation doses associated with use of analytic reconstruction methods in DPCT, we analyze the numerical and statistical properties of two classes of discrete imaging models that form the basis for iterative image reconstruction. Secondly, to improve image quality in grating-based phase-contrast tomography, we incorporate 2nd order statistical properties of the object property sinograms, including correlations between them, into the formulation of an advanced multi-channel (MC) image reconstruction algorithm, which

reconstructs three object properties simultaneously. We developed an advanced algorithm based on the proximal point algorithm and the augmented Lagrangian method to rapidly solve the MC reconstruction problem. Thirdly, to mitigate image artifacts that arise from reduced-view and/or noisy decomposed sinogram data in K-edge imaging, we exploited the inherent sparseness of typical K-edge objects and incorporated the statistical properties of the decomposed sinograms to formulate two penalized weighted least square problems with a total variation (TV) penalty and a weighted sum of a TV penalty and an ℓ_1-norm penalty with a wavelet sparsifying transform. We employed a fast iterative shrinkage/thresholding algorithm (FISTA) and splitting-based FISTA algorithm to solve these two PWLS problems. Fourthly, to enable advanced iterative algorithms to obtain better diagnostic images and accurate patient positioning information in image-guided radiation therapy for CBCT in a few minutes, two accelerated variants of the FISTA for PLS-based image reconstruction are proposed. The algorithm acceleration is obtained by replacing the original gradient-descent step by a sub-problem that is solved by use of the ordered subset concept (OS-SART). In addition, we also present efficient numerical implementations of the proposed algorithms that exploit the massive data parallelism of multiple graphics processing units (GPUs). Finally, we employed our developed accelerated version of FISTA for dealing with the incomplete (and often noisy) data inherent to in-line XPC tomosynthesis which combines the concepts of tomosynthesis and in-line XPC imaging to utilize the advantages of both for biological imaging applications. We also investigate the depth resolution properties of XPC tomosynthesis and demonstrate that the z-resolution properties of XPC tomosynthesis is superior to that of conventional absorption-based tomosynthesis. To investigate all these proposed novel strategies and new algorithms in these different imaging modalities, we conducted computer simulation studies and real experimental data studies. The proposed reconstruction methods will facilitate the clinical or preclinical translation of these emerging imaging methods.

Chapter 1

Introduction

Many new promising X-ray-based imaging technologies are emerging over the last two decades, including phase-contrast imaging technologies, spectral CT (K-edge imaging), cone-beam computed tomography for diagnosis and other emerging X-ray technologies [8, 9, 188]. However, one or more specific problems prevent them being effectively or efficiently employed in clinical applications. Five different novel X-ray based imaging technoloiges are discussed in this dissertation, including differential phase-contrast tomography (DPCT), grating-based phase-contrast tomography (GB-PCT), spectral-CT (K-edge imaging), cone-beam computed tomography (CBCT) and in-line X-ray phase contrast (XPC) tomosynthesis. The goal and purposes of this dissertation is to introduce some new approaches and strategies to enable them to thoroughly penetrated and even directly employed for clinical applications. we will briefly review these imaging modalities and their specific problems in the following.

1.1 Background and Motivation

1.1.1 Differential phase-contrast imaging

Differential phase-contrast tomography (DPCT) employing hard X-rays [24,107,113,114,169] refers to a class of imaging method for reconstructing the X-ray refractive index distribution of objects from knowledge of differential projection data. At hard X-ray energies, variations in the real component of the refractive index distribution of a light- or medium-density material are generally several orders of magnitude larger than are the variations in the imaginary

component (i.e., the X-ray absorption). Consequently, DPCT may permit the visualization and quantitation of objects that present very low or no X-ray absorption contrast. In recent years, there have also been advancements [49,134] in implementing the method on the bench top by use of tube-based X-ray sources. This is particular important in order for DPCT to find widespread use in biomedical and nondestructive imaging applications.

The tomographic projection data in DPCT, from which an estimate of the refractive index distribution is reconstructed, correspond to one-dimensional (1D) derivatives with respect to the detector row coordinate of the two-dimensional (2D) Radon transform of the refractive index distribution. These data can be interpreted as the angles in a plane that is perpendicular to the axis of tomographic scanning by which the probing X-ray beams are deflected by the object due to refraction. Several methods are available for implementing DPCT by use of synchrotron- or tube-based X-ray sources. Such methods include those based on diffractive optics [34,133] or interferometry [112]. When DPCT is implemented with optical wavefields, which has been referred to as beam-deflection tomography [51], techniques such as moire deflectometry [154] have been employed for measuring the beam-deflection data.

It has been demonstrated that image reconstruction in DPCT can be achieved by use of modified filtered backprojection (FBP) algorithms [51,78,186]. An important observation by Faris and Byer [51] was that the 1D differentiation of the projection data is prescribed by the classic FBP algorithm. Accordingly, instead of integrating the differential projection data explicitly and then applying the classic FBP algorithm for reconstruction, they proposed a deflection filtered backprojection DFBP algorithm that acts directly on the differential projection data. In order to avoid image artifacts when employing this algorithm and other analytic reconstruction algorithms, tomographic measurements must be typically be acquired at a large number of view angles. This is highly undesirable because it can result in long data-acquisition times, especially in bench top applications where the X-ray tube power is limited, and also may damage the sample due to the large radiation exposure. Iterative image reconstruction algorithms have been widely employed in mature tomographic imaging modalities for mitigating data-incompleteness and noise. However, there is a scarcity of studies of iterative image reconstruction in DPCT [89,134] and there remains an important need to develop robust iterative reconstruction methods for this modality.

1.1.2 Grating-based phase-contrast imaging

Grating-based X-ray phase-contrast (GB-XPC) imaging and tomography [43, 109, 110, 112, 133, 169] is one type of differential phase-contrast imaging. GB-XPC imaging can produce volumetric images that depict three different object properties: X-ray absorption, scattering, and refractive index. Medical imaging applications of GB-XPCT are limited by long data-acquisition times and relatively high radiation doses. A natural way to mitigate these problems is to reduce exposure times and/or the number of tomographic views at which data are acquired. From such data, statistically-principled algorithms can be employed for image reconstruction. Several iterative image reconstruction algorithms for GB-XPCT have been proposed [90, 120, 121, 177]. However, to the best of our knowledge, none of the methods investigated to date take full advantage of the second order statistical properties of the sinogram data corresponding to the three object properties.

1.1.3 Spectral CT (K-edge imaging)

The development of spectral X-ray computed tomography (CT) using binned photon-counting detectors has received great attention in recent years and is prompting a paradigm shift in X-ray CT imaging. These advancements are likely to benefit numerous preclinical and clinical imaging applications. For example, K-edge CT has been investigated as a modality to image contrast agents such as iodine [2, 74], gadolinium [59], bismuth [127], and gold [38]. Ytterbium was recently discussed as a contrast agent for conventional CT [98] in general and K-edge imaging [128].

The task of image reconstruction in spectral CT can be implemented in a two-stage processing scheme. In the first step, estimates of material-decomposed sinograms are obtained from the measured energy-resolved photon counts. In the second step, material images are reconstructed from knowledge of the material sinogram estimates. Statistically-principled reconstruction algorithms have been proposed [55, 144, 146, 158] that seek to minimize a penalized weighted least squares (PWLS) cost function. The weighting matrix employed in the data-fidelity term, which corresponds to the inverse covariance of the computed material sinograms, can be estimated in different ways [53, 139, 182].

While it holds great potential for important preclinical and clinical applications, selective imaging of K-edge materials in spectral CT faces challenges that currently limit its applicability. Implementations of K-edge CT employ photon counting detectors to detect the energies of individual photons. To avoid pulse-pileup in the detector, photon fluxes must be limited, which can result in long data-acquisition times. One way to mitigate long data-acquisition times is to develop image reconstruction algorithms that can produce useful images from few-view and/or noisy decomposed sinogram data. While K-edge images are often sparse, the ability of sparsity-based regularization strategies coupled with knowledge of the object-specific noise properties of the decomposed K-edge sinogram data to improve reconstructed image quality in K-edge CT remains largely unexplored.

1.1.4 Cone-beam computed tomography

X-ray cone-beam computed tomography (CBCT) employing a circular scanning geometry is a widely employed three-dimensional (3D) imaging modality with numerous applications that include image-guided radiation therapy (IGRT), micro-computed tomography (CT), and dental imaging, to name only a few. There exist a vast literature related to the development and application of CBCT image reconstruction methods, and we refer readers to the recent literature for representative examples [19, 36, 72, 82, 85, 123, 130, 138]. The potential advantages of iterative algorithms over analytical algorithms are well-known, and include the flexibility to incorporate physical factors in the imaging model and effectively mitigate data incompleteness and noise. The development of iterative image reconstruction algorithms that implement non-smooth regularizers, including the TV penalty and other sparsity-promoting forms, remains an active and important research area [149, 151]. Even with hardware acceleration, however, the overwhelming majority of the available 3D iterative algorithms that implement non-smooth regularizers remain computationally burdensome and have not been translated for routine use in time-sensitive applications such as IRGT.

The fast iterative shrinkage thresholding algorithm (FISTA) [14, 15] is a state-of-the-art optimization algorithm that possesses several characteristics that are well-suited for iterative CBCT image reconstruction. However, it remains largely unexplored for this important application. Because it can be employed to minimize a cost function that is specified by the sum of a smooth and convex data fidelity term and a convex but possibly non-smooth

penalty, the FISTA can be employed for PLS reconstruction problems in which a TV penalty or other sparsity promoting forms are employed. The FISTA does not require approximate computation of the discretized TV function or the gradient discretized TV term, which most previously proposed algorithms require. The FISTA can also readily incorporate positivity or other bound constraints. Mathematically, it has been proven that the FISTA achieves a second-order convergence rate. It can therefore potentially reduce the number of iterations required to produce an image of a specified image quality as compared to first-order methods such as the steepest decent method. However, because the FISTA employs a gradient-descent step, which is known to limit convergence rates in conventional algorithms, there remains an opportunity to modify it and obtain an accelerated second-order algorithm that will lead to further reductions in image reconstruction times.

1.1.5 In-line phase-contrast tomosynthesis

X-ray phase-contrast (XPC) imaging is a promising technique for visualizing soft tissue features in many biological applications [95, 113, 187]. There are several XPC imaging methods including crystal-based [162] and grating-based [169] varieties. In-line (or propagation-based) XPC is the simplest form to implement, requiring only a small X-ray focal spot, a high resolution detector and a sufficient propagation distance between the object and detector [171]. In practice, these requirements lead to longer acquisition times than conventional absorption-based radiography. These long acquisition times can be prohibitive for extending XPC computerized tomography (XPC CT) to pre-clinical and clinical scenarios. To circumvent this, tomosynthesis methods can be employed to reconstruct volumetric images from a relatively small number of projections at the cost of sacrificing spatial resolution in the depth-direction [47].

Conventional X-ray tomosynthesis, which is a form of limited angle tomography that employs only a few x-ray planar projections in a proper angular range to synthesize a collection of 2D images, has been widely studied for breast imaging and other medical imaging applications. There has been a high degree of research interest in tomosynthesis imaging in the past decade [6, 46, 64, 136]. Tomosynthesis allows for some level of low-resolution discrimination between overlaying structures along the z direction (i.e., in-depth direction perpendicular to the in-plane images), bringing a substantial improvement in the ability to appreciate

abnormal anatomy or disease in tomosynthesis images relative to conventional radiographs. Besides, the resolution of the reconstructed in-plane images is often believed to be superior to CT, at the same time tomosynthesis provides much reduced dose and faster acquisition time than that required for full CT datasets.

In recent years, a small number of studies have explored XPC tomosynthesis imaging techniques. In 2010, Zhang *et al.* published in-line XPC tomosynthesis experimental results from data acquired with synchrotron radiation [181]. A phase retrieval filter was applied to the raw in-line projections so that the reconstruction problem was converted to be the same as conventional tomosynthesis. Hammonds *et al.* investigated in-line XPC tomosynthesis using a micro-focus x-ray tube in 2011 [70] A standard shift-and-add (SAA) algorithm was directly performed in the tomosynthesis reconstruction, and it showed that the reconstructed in-plane images (i.e. x-y plane shown in Fig. 6.1) could retain the edge enhancement that is observed in planar phase-contrast radiographs. Wu *et al.* conducted in-plane spatial resolution measurements of a phase-contrast tomosynthesis prototype using standard resolution test patterns [172], but certain details regarding the data-acquisition and reconstruction were not reported.

1.2 Overview of the Dissertation

In Chapter 2, we analyze the numerical and statistical properties of two classes of discrete imaging models that form the basis for iterative image reconstruction in DPCT. We also investigate the use of one of the models with a modern image reconstruction algorithm for performing few-view image reconstruction of a tissue specimen.

In Chapter 3, we report on the development of an advanced multi-channel (MC) image reconstruction algorithm for grating-based X-ray phase-contrast computed tomography (GB-XPCT). The MC reconstruction method we have developed operates by concurrently, rather than independently as is done conventionally, reconstructing tomographic images of the three object properties (absorption, small-angle scattering, refractive index). By jointly estimating the object properties by use of an appropriately dened penalized weighted least squares (PWLS) estimator, the 2nd order statistical properties of the object property sinograms, including correlations between them, can be fully exploited to improve the variance vs.

resolution tradeo of the reconstructed images as compared to existing methods. Channel-independent regularization strategies are proposed. To solve the MC reconstruction problem, we developed an advanced algorithm based on the proximal point algorithm and the augmented Lagrangian method. By use of experimental and computer-simulation data, we demonstrate that by exploiting inter-channel noise correlations, the MC reconstruction method can improve image quality in GB-XPCT.

In Chapter 4, we describe and investigate sparsity-regularized penalized weighted least squares-based image reconstruction algorithms for reconstructing K-edge images from few-view decomposed K-edge sinogram data. To exploit the inherent sparseness of typical K-edge images, we investigate use of a total variation (TV) penalty and a weighted sum of a TV penalty and an ℓ_1-norm with a wavelet sparsifying transform. Computer-simulation and experimental phantom studies are conducted to quantitatively demonstrate the effectiveness of the proposed reconstruction algorithms.

In Chapter 5, we propose two accelerated variants of the FISTA for PLS-based image reconstruction in CBCT. The algorithm acceleration is obtained by replacing the original gradient-descent step by a sub-problem that is solved by use of the ordered subset simultaneous algebraic reconstruction technique (OS-SART). One algorithm seeks to minimize a PLS cost function involving a TV penalty while the second assumes a penalty formed as the sum of object TV plus a wavelet-sparsified We also present efficient numerical implementions of the proposed algorithms that exploit the massive data parallelism of multiple graphics processings units (GPUs).

In Chapter 6 we develop an advanced iterative algorithm for reconstructing images from incomplete (and noisy) data in XPC tomosynthesis. We also investigate the depth resolution properties of XPC tomosynthesis and demonstrate that the z-resolution properties of XPC tomosynthesis is superior to that of conventional absorption-based tomosynthesis. More specifically, we find in-plane structures display strong boundary-enhancement while out-of-plane structures do not. This effect can facilitate the identification of in-plane structures.

A summary of the dissertation and closing remarks are presented in Chapter 7.

Chapter 2

Investigation of discrete imaging models and iterative image reconstruction in DPCT

2.1 Introduction

Differential phase-contrast tomography (DPCT) employing hard X-rays [24,107,113,114,169] refers to a class of imaging method for reconstructing the X-ray refractive index distribution of objects from knowledge of differential projection data. At hard X-ray energies, variations in the real component of the refractive index distribution of a light- or medium-density material are generally several orders of magnitude larger than are the variations in the imaginary component (i.e., the X-ray absorption). Consequently, DPCT may permit the visualization and quantitation of objects that present very low or no X-ray absorption contrast. In recent years, there have also been advancements [49,134] in implementing the method on the bench top by use of tube-based X-ray sources. This is particular important in order for DPCT to find widespread use in biomedical and nondestructive imaging applications.

The tomographic projection data in DPCT, from which an estimate of the refractive index distribution is reconstructed, correspond to one-dimensional (1D) derivatives with respect to the detector row coordinate of the two-dimensional (2D) Radon transform of the refractive index distribution. These data can be interpreted as the angles in a plane that is perpendicular to the axis of tomographic scanning by which the probing X-ray beams are deflected by the object due to refraction. Several methods are available for implementing DPCT by use of

synchrotron- or tube-based X-ray sources. Such methods include those based on diffractive optics [34, 133] or interferometry [112]. When DPCT is implemented with optical wavefields, which has been referred to as beam-deflection tomography [51], techniques such as moire deflectometry [154] have been employed for measuring the beam-deflection data.

It has been demonstrated that image reconstruction in DPCT can be achieved by use of modified filtered backprojection (FBP) algorithms [51,78,186]. An important observation by Faris and Byer [51] was that the 1D differentiation of the projection data is prescribed by the classic FBP algorithm. Accordingly, instead of integrating the differential projection data explicitly and then applying the classic FBP algorithm for reconstruction, they proposed a deflection filtered backprojection DFBP algorithm that acts directly on the differential projection data. In order to avoid image artifacts when employing this algorithm and other analytic reconstruction algorithms, tomographic measurements must be typically be acquired at a large number of view angles. This is highly undesirable because it can result in long data-acquisition times, especially in bench top applications where the X-ray tube power is limited, and also may damage the sample due to the large radiation exposure. Iterative image reconstruction algorithms have been widely employed in mature tomographic imaging modalities for mitigating data-incompleteness and noise. However, there is a scarcity of studies of iterative image reconstruction in DPCT [89, 134] and there remains an important need to develop robust iterative reconstruction methods for this modality.

In this chapter, we analyze the numerical and statistical properties of two classes of discrete imaging models that form the basis for iterative image reconstruction in DPCT. The models differ in the choice of expansion functions that are employed to discretize the infinite-dimensional refractive index distribution that one seeks to estimate. One model employs conventional pixel expansion functions while the other employs Kaiser-Bessel window functions. The latter choice is shown to have the attractive feature that the 1D derivative operator in the DPCT imaging model can be computed analytically, thereby cirvumventing the need to numerically approximate it. This feature has also recently been identified by Köhler, *et al.* [89]. A modern iterative reconstruction algorithm that seeks to minimize total variation (TV) -norm of the refractive index estimate is employed with a discrete imaging model for few-view image reconstruction. The effectiveness of the reconstruction method is demonstrated by use of experimental DPCT projection data corresponding to a biological tissue specimen.

2.2 Background

We will utilize the parallel-beam tomographic scanning geometry depicted in Fig. 2.1. However, the results that follow can readily be adapted to the case of spherical wave illumination in the paraxial limit [49]. The z-axis of the reference coordinate system (x, y, z) defines the axis of rotation of the tomographic scanning. The rotated coordinate system (x_r, y_r, z) is related to the reference system by by $x_r = x\cos\theta + y\sin\theta, y_r = y\cos\theta - x\sin\theta$, where $\theta \in [0, \pi)$ is the tomographic view angle measured from the positive x-axis. A phase-amplitude object positioned at the origin is irradiated by an X-ray plane-wave with wavelength λ, or equivalently wavenumber $k = \frac{2\pi}{\lambda}$, which propagates in the direction of the positive y_r-axis.

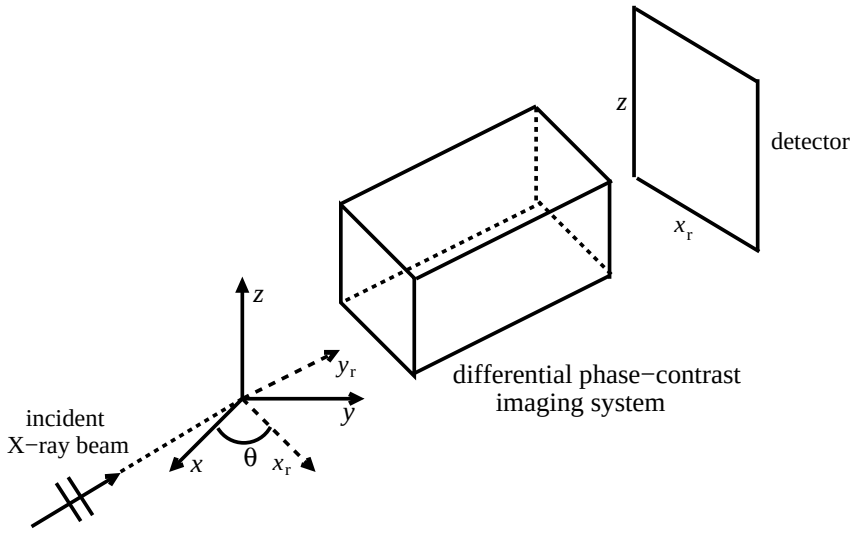

Figure 2.1: A schematic of differential phase-contrast imaging tomography. The black box represents the system of optical elements that is specific to the implementation.

2.2.1 Data function and imaging model in continuous form

Let $\delta(x, y, z) \equiv 1 - n(x, y, z)$ denote the compactly supported and bounded object function we seek to reconstruct, where $n(x, y, z)$ is the real-valued refractive index distribution. We will employ the notation $\delta(\mathbf{r}_2; z) \equiv \delta(x, y, z)$, where $\mathbf{r}_2 = (x, y)$, as a convenient description of a transverse slice of the 3D object function.

In DPCT employing a grating interferometer [108, 109, 112, 133, 169] or X-ray crystal optics [34, 44, 45, 60, 92, 103, 131, 170], the wavefield transmitted through the object is perturbed by one or more optical elements. The intensity of the perturbed wavefield at view angle θ is measured in the (x_r, z) plane located at $y_r = d$ and will be denoted by $I(x_r, z, \theta; K)$. Here K represents an integer-valued index that specifies the state of the imaging system. For example, in crystal analyzer-based systems, distinct values of K would correspond to different orientations of the analyzer crystal. Alternatively, in grating interferometry when a phase-stepping procedure [133,169] is employed, distinct values of K correspond to different translational positions of the grating that is being scanned.

From knowledge of $\{I(x_r, z, \theta; k)\}_{K=1}^{N_K}$ with $N_K \geq 1$, methods are available [40, 155, 169] for computing a data function $g(x_r, z, \theta)$ that, for a fixed value of z, is related to the sought-after object function $\delta(\mathbf{r}_2; z)$ as

$$g(x_r, \theta; z) = \frac{\partial}{\partial x_r} \int_{\infty} dy_r \; \delta(\mathbf{r}_2; z) \equiv \frac{\partial}{\partial x_r} \mathbf{R}\delta(\mathbf{r}_2; z). \tag{2.1}$$

Here, $\mathbf{R}$ denotes the 2D Radon transform operator. Equation (2.1) represents an idealized imaging model for DPCT in its continuous form that assumes a geometrical optics approximation. A discussion of the validity of this approximation is provided in Chapter 2 of reference [126]. Note that the right hand side of Eq. (2.1) corresponds to a stack, along the z-axis, of differentiated 2D Radon transforms of $\delta(\mathbf{r}_2; z)$. The coordinate z can be interpreted as a parameter that specifies a transverse slice and therefore the 3D imaging model can be described by a collection of 2D ones.

The image reconstruction task in DPCT is to determine an estimate of $\delta(\mathbf{r}_2; z)$ from knowledge of $g(x_r, \theta; z)$. When $g(x_r, \theta; z)$ is measured at a large number of view angles θ, this can be accomplished by use of analytic image reconstruction algorithms [4, 51]. However, in the case of noisy and/or few-view measurement data, analytic reconstruction methods are known to be suboptimal and the use of iterative methods is warranted. The construction and investigation of discrete imaging models that form the basis for iterative image reconstruction in DPCT is described in the remainder of the article.

2.2.2 General forms of discrete imaging models

A natural way to obtain a discrete imaging model is to discretize the continuous model in Eq. (2.1). When a digital detector is employed, the measured intensity data and associated data function correspond to an ordered collection of numbers rather than a function of a continuous variable. We will denote the discrete data function as

$$g[s,t;h] \equiv g(x_r,\theta;z)|_{x_r=s\Delta_d,\theta=t\Delta_\theta,z=h\Delta_d}, \tag{2.2}$$

where s and h are integer-valued detector element indices and t is the tomographic view index. Here, $\Delta_d = \frac{L}{Q}$ denotes the detector element dimension in a square detector array of dimension $L \times L$, and Q denotes the number of samples measured in each dimension. The quantity Δ_θ denotes the angular sampling interval between the uniformly distributed view angles. The reconstruction algorithms described below can be applied in the case of non-uniformly sampled measurement data as well. The general forms of the reconstruction algorithms would remain unchanged for the case of non-uniformly sampled measurement data; However, the explicit forms of the system matrices would be changed. Although not indicated in Eq. (2.2), the measured discrete data will also be degraded by the averaging effects of the sampling aperture. Additionally, the effects of finite temporal and spatial beam coherence will effectively blur the data function $g[s,t;h]$. These effects can limit the attainable spatial resolution in the reconstructed DPCT images. Because the reconstruction problem is inherently 2D, we will consider the problem of reconstructing a transverse slice of the object function located at $z = h\Delta_d$. Let the vector $\mathbf{g} \in \mathbb{R}^M$ denote a lexicographically ordered representation of $g[s,h,t]$. The dimension M is defined by the product of the number of detector row elements and the number of view angles.

Many iterative image reconstruction algorithms require a finite-dimensional approximate representation of the object function. A linear N-dimensional approximation of $\delta(\mathbf{r}_2; z = h\Delta_d)$ can be formed as

$$\delta_a(\mathbf{r}_2; z = h\Delta_d) = \sum_{n=0}^{N-1} \mathbf{b}_n^h \phi_n(\mathbf{r}_2), \tag{2.3}$$

where the subscript a indicates that $\delta_a(\mathbf{r_2};\mathbf{z})$ is an approximation of $\delta(\mathbf{r_2};\mathbf{z})$, $\{\phi_n(\mathbf{r}_2)\}$ are a set of expansion functions, and $\{\mathbf{b}_n^h\}$ are the corresponding expansion coefficients that depend on the slice index h. Let the 2D function $\delta_a(\mathbf{r}_2; z = h\Delta_d)$ be contained within a disk

of radius r_0. The discrete data function satisfies

$$g[s,t;h] \approx \frac{\partial}{\partial x_r}\mathbf{R}\delta_a(\mathbf{r}_2; z = h\Delta_d)\Big|_{x_r=s\Delta_d,\theta=t\Delta_\theta}, \tag{2.4}$$

assuming that $\mathbf{R}\delta_a(\mathbf{r}_2; z = h\Delta_d)$ is differentiable $\forall x_r \in (-r_0, r_0)$. For certain choices of the expansion functions, such as the pixels described below, this differentiability requirement will not be met. Moreover, when computing Eq. (2.4), as required by iterative image reconstruction algorithms, the operator $\frac{\partial}{\partial x_r}$ will generally be replaced by a numerical approximation. For use in these cases, a modified version of Eq. (2.4) is given by

$$g[s,t;h] \approx \frac{\partial}{\partial x_r}\mathbf{S}\mathbf{R}\delta_a(\mathbf{r}_2; z = h\Delta_d)\Big|_{x_r=s\Delta_d,\theta=t\Delta_\theta}, \tag{2.5}$$

where $\mathbf{S}$ is a smoothing operator that acts with respect to the x_r coordinate and ensures that $\mathbf{S}\mathbf{R}\delta_a(\mathbf{r}_2; z = h\Delta_d)$ is differentiable. The composite operator $\frac{\partial}{\partial x_r}\mathbf{S}$ can be interpreted as a regularized derivative operator.

In the special case where $\mathbf{R}\phi_n(\mathbf{r}_2)$ is differentiable $\forall x_r \in (-r_0, r_0)$, as satisfied by the Kaiser-Bessel expansion functions investigated below, Eq. (2.4) can be expressed as

$$g[s,t;h] \approx \sum_{n=0}^{N-1} \mathbf{b}_n^h \frac{\partial}{\partial x_r}\big(\mathbf{R}\phi_n(\mathbf{r}_2)\big)(x_r,\theta)|_{x_r=s\Delta_d,\theta=t\Delta_\theta}. \tag{2.6}$$

In matrix form, each of Eqs. (2.4)-(2.6) can be expressed as

$$\mathbf{g} = \mathbf{H}\mathbf{b}, \tag{2.7}$$

where $\mathbf{g}$ is a lexicographically ordered representation of the sampled data function, $\mathbf{H}$ is an $M \times N$ system matrix, and $\mathbf{b}$ is a $N \times 1$ vector of expansion coefficients that has an n-th element given by $\mathbf{b}_n^h$.

Equations (2.5) or (2.6) describe discrete imaging models for DPCT that can be employed with iterative image reconstruction algorithms for estimation of $\mathbf{b}$ from knowledge of $\mathbf{g}$ and $\mathbf{H}$. From the estimated $\mathbf{b}$, the object function estimate - the sought after image - can be obtained by use of Eq. (3.6). In the special case in which the expansion functions are classical

pixels, the estimates of $\mathbf{b}$ and $\delta_a(\mathbf{r}_2; z = h\Delta_d)$ coincide. Explicit forms for the system matrix $\mathbf{H}$ are found by specifying the expansion functions $\phi_n(\mathbf{r}_2)$ and implementation of the operator $\frac{\partial}{\partial x_r}\mathbf{R}$ or $\frac{\partial}{\partial x_r}\mathbf{SR}$.

Below, we investigate the use of two different choices of expansion functions: the pixel basis function and Kaiser-Bessel window functions. Because the 3D reconstruction problem corresponds to a stack of 2D ones, we will focus on the reconstruction of a transverse slice of constant $z = h\Delta_d$ and the discrete index h will be suppressed hereafter. For use with the pixel basis functions, three different discrete implementations of the operator $\frac{\partial}{\partial x_r}\mathbf{SR}$ are implemented and system matrices are established according to Eq. (2.5). For the case of the Kaiser-Bessel window expansion functions, the operator $\frac{\partial}{\partial x_r}\mathbf{R}\phi_n(\mathbf{r}_2)$ can be computed analytically and system matrices are established according to Eq. (2.6).

2.3 Construction of system matrices for iterative image reconstruction in DPCT

2.3.1 System matrix construction employing pixel basis functions

The classic pixel is a commonly employed expansion function and is defined as

$$\phi_n^{pixel}(\mathbf{r_2}) = \mathrm{rect}\big(\frac{x - x_n}{\epsilon}\big)\mathrm{rect}\big(\frac{y - y_n}{\epsilon}\big),$$

where $\mathrm{rect}(x) = 1$ for $|x| \leq \frac{1}{2}$ and zero elsewhere, (x_n, y_n) specifies the coordinate of the nth lattice point on a uniform Cartesian lattice, and ϵ is the spacing between those lattice points. A description of the system matrix construction for use with pixel expansion functions provided below. According to Eq. (2.5), this will require specifying methods for : (1) numerically approximating $\mathbf{R}\delta_a(\mathbf{r_2}; \mathbf{z})$ and (2) computing a regularized discrete derivative operator $\frac{\partial}{\partial x_r}\mathbf{S}$.

Numerous standard numerical methods are available to compute approximations of $\mathbf{R}\delta_a(\mathbf{r_2}; z)$ [86, 99, 148]. Most of these numerical methods compute the projection data as

$$p[s,t] \equiv (\mathbf{R}\delta_a(\mathbf{r}_2))[s,t] = (\mathbf{R}\delta_a(\mathbf{r}_2))(x_r,\theta)|_{x_r=s\Delta_d,\theta=t\Delta_\theta} \approx \sum_{j=0}^{N-1} w_{stj} b_j, \tag{2.8}$$

where w_{stj} is the weighting factor that corresponds to the contribution of the j-th expansion function to the projection data recorded at detector location $[s,t]$, and b_j is the j-th component of $\mathbf{b}$. By defining $\mathbf{p} \in \mathbb{R}^M$ to be a lexicographically ordered representation of $p[s,t]$, Eq. (2.8) can be expressed in matrix form as

$$\mathbf{p} = \mathbf{H}^R \mathbf{b}, \tag{2.9}$$

where

$$[\mathbf{H}^R]_{m=t\times S+s,\ n} = w_{stn}, \tag{2.10}$$

in which S is the total number of discrete projection data for each view and the notation $[\mathbf{H}^R]_{m,n}$ denotes the element of $\mathbf{H}^R$ corresponding to the m-th row and n-th column. In our numerical studies, we adopted a 'ray-driven' method to establish $\mathbf{H}^R$ [148].

We adopted a meshfree method known as smoothed particle hydrodynamics (SPH) [33, 115] for implementing $\frac{\partial}{\partial x_r}\mathbf{S}$. Let $\mathbf{p}' \in \mathbb{R}^{\mathbf{M}}$ denote a 1D discrete derivative of $\mathbf{p}$ that approximates samples of $\frac{\partial}{\partial x_r}\mathbf{S}\mathbf{R}\delta_a(\mathbf{r}_2; z = h\Delta_d)$. The SPH method determines $\mathbf{p}'$ as

$$p'_k = \frac{1}{\rho_k} \sum_{i=k-K/2}^{i=k+K/2} (p_i - p_k) \frac{\partial \mathbf{W}(d_i - d_k, h)}{\partial x_r}, \tag{2.11}$$

where p'_k is the k-th element of $\mathbf{p}'$, K is the total number of neighbouring particles, p_i and p_k are the i-th and k-th elements of $\mathbf{p}$ respectively, and $\mathbf{W}(x_r, h)$ is a kernel function with a smoothing length h. In our studies we employed three different kernel functions of the form: linear, quadratic spline, and cubic spline [33, 115]. Explicit forms of the kernels are provided in the appendix. The density factor ρ_k is defined as

$$\rho_k = \sum_{i=k-K/2}^{i=k+K/2} \mathbf{W}(d_i - d_k, h). \tag{2.12}$$

In matrix form, Eq. (2.11) is expressed as

$$\mathbf{p}' = \mathbf{H}^D \mathbf{p}, \tag{2.13}$$

where explicit forms of $\mathbf{H}^D$ are provided in the appendix that correspond to different choices of $\mathbf{W}(x_r, h)$.

By use of Eqs. (2.9) and (2.13), the discrete imaging models for the case of pixel expansion functions are obtained as

$$\mathbf{g} \approx \mathbf{p}' = \mathbf{H}^{pixel} \mathbf{b}, \tag{2.14}$$

where

$$\mathbf{H}^{pixel} \equiv \mathbf{H}^D \mathbf{H}^R. \tag{2.15}$$

The system matrix $\mathbf{H}^{pixel}$ is generally sparse, since only a few expansion functions contribute to one specific projection value p_i.

2.3.2 System matrix construction employing generalized Kaiser-Bessel window functions

For Kaiser-Bessel window expansion functions, referred to hereafter as "blobs" [96, 97], $\frac{\partial}{\partial x_r}\mathbf{R}\phi_n(\mathbf{r_2})$ is continuous and can be computed analytically. In this case, Eq. (2.6) can be employed to establish the system matrix in which the derivative and Radon transform operators can be computed accurately.

The blob expansion functions are defined as

$$\phi_n^{blob}(\mathbf{r}_2; m, a, \alpha) = \begin{cases} \frac{\left[\sqrt{1-(r_b/a)^2}\right]^m I_m[\alpha\sqrt{1-(r_b/a)^2}]}{I_m(\alpha)}, & \mathbf{r}_b \leq a \\ 0, & \text{otherwise,} \end{cases} \tag{2.16}$$

where $I_m(\cdot)$ is the *m-th* order modified Bessel function, $\mathbf{r}_b \equiv |\mathbf{r}_2 - \mathbf{r}_n|$ with $\mathbf{r}_n = (x_n, y_n)$ denoting the blob center, and a and α determine the blob's radius and specific shape.

Let $\xi \equiv x_r - x_n \cos\theta - y_n \sin\theta$. As demonstrated by Lewitt [96], the 2D Radon transform of one window function is given by

$$\mathbf{R}\phi_n^{blob}(\mathbf{r}_2; m, a, \alpha) = \frac{a}{I_m(\alpha)} \left(\frac{2\pi}{\alpha}\right)^{1/2} \left[\sqrt{1-(\xi/a)^2}\right]^{m+1/2} I_{m+1/2}\left(\alpha\sqrt{1-(\xi/a)^2}\right), \quad (2.17)$$

for $|\xi| \leq a$ and zero otherwise.

As derived in Appendix B, the 1D derivative of this quantity is given by

$$\frac{\partial(\mathbf{R}\phi_n^{blob}(\mathbf{r}_2; m, a, \alpha))}{\partial x_r} = -\frac{(2\pi\alpha)^{1/2}}{I_m(\alpha)} \frac{\xi}{a} \left(\sqrt{1-(\xi/a)^2}\right)^{m-1/2} I_{m-1/2}\left(\alpha\sqrt{1-(\xi/a)^2}\right). \quad (2.18)$$

By use of Eqs. (2.18) and (2.6) the discrete imaging model is given by

$$g[s,t] \approx -\frac{(2\pi\alpha)^{1/2}}{I_m(\alpha)}$$

$$\times \sum_{n=0}^{N-1} \mathbf{b}_n \frac{\xi}{a} \left(\sqrt{1-(\xi/a)^2}\right)^{m-1/2} I_{m-1/2}\left(\alpha\sqrt{1-(\xi/a)^2}\right)\Big|_{\xi = s\Delta_d - x_n\cos(t\Delta_\theta) - y_n\sin(t\Delta_\theta)}, \quad (2.19)$$

or, in matrix form,

$$\mathbf{g} \approx \mathbf{H}^{blob}\mathbf{b}, \quad (2.20)$$

where

$$[\mathbf{H}^{blob}]_{m',n} = [\mathbf{H}^{blob}]_{m'=t\times S+s,\ n} = -\frac{(2\pi\alpha)^{1/2}}{I_m(\alpha)}$$
$$\times \frac{\xi}{a} \left(\sqrt{1-(\xi/a)^2}\right)^{m-1/2} I_{m-1/2}\left(\alpha\sqrt{1-(\xi/a)^2}\right)\Big|_{\xi = s\Delta_d - x_n\cos(t\Delta_\theta) - y_n\sin(t\Delta_\theta)}, \quad (2.21)$$

and S is the total number of discrete projection data for each view. Similar to the pixel case, the system matrix $\mathbf{H}^{\mathbf{blob}}$ is sparse because only a relatively few blobs contribute to each component of $\mathbf{g}$.

Note that the k-th order spatial derivative of $\phi_n^{blob}(\mathbf{r}_2; m, a, \alpha)$ is continuous when $m > k$ [96]. In the studies below, $m = 2$ was chosen. This ensured that the first-order derivatives of the blobs were continuous.

2.4 Comparison of numerical and statistical properties of system matrices

2.4.1 SVD analysis of the system matrices

In order to investigate how the different expansion functions influence the numerical properties of the imaging models described in Sections 2.3.1 and 2.3.2, the singular value decomposition (SVD) was employed. Specifically, the rates of decay of the singular values associated with the different system matrices were examined to gain insights into the stability of the associated reconstruction problems. It is well-known that the stability of a reconstruction problem is adversely affected by a rapid decay of singular values [18]. For the pixel basis function, three system matrices $\mathbf{H}^{pixel}$ were constructed as described in Sec. 2.3.1 for the cases where linear, quadratic spline, and cubic spline kernel functions $\mathbf{W}(x_r, h)$ were employed [33, 52, 115]. Explicit forms of three kernels are provided in the appendix. The scanning configuration assumed 180 equally spaced tomographic views and 256 samples along the detector array. The detector pixel pitch was 25 μm. The window size of h was chosen to be two times detector pixel pitch, three times detector pixel pitch, and four times detector pixel pitch for linear interpolation, quadratic spline and cubic spline kernel, respectively. The object was assumed to be contained within an area of dimension 6.4 mm $\times$ 6.4 mm. For the pixel-based studies, a 128×128 array of 50 μm square pixels was employed to discretize the object. Accordingly, the system matrices $\mathbf{H}^{pixel}$ were of dimension 46080 (256×180) by 16384 (128×128). For the case of blob expansion functions, the same scanning configuration was considered. Six system matrices $\mathbf{H}^{blob}$ were constructed as described in Sec. 2.3.2 for the cases where the blob parameters were chosen as $m = 2$, radius $a = 75$ μm (1.5 times sampling interval) or 100 μm (2 times sampling interval), and $\alpha = 2, 6$, or 10.4. Hereafter, we will refer to the blob radius relative to the image grid spacing. For example, we use indicate a = 1.5 to represent a physical radius of 75 μm and a = 2 to represent a physical radius of 100μm. The value of $\alpha = 10.4$ was chosen because it results in a quasi-bandlimited blob function that has been demonstrated to suppress artifacts in other tomographic image reconstruction applications [97, 105].

Similar values were employed in references [106, 125]. The distance between the centers of two neighboring blobs was fixed at 50 μm. The dimension of $\mathbf{H}^{blob}$ is the same as that of $\mathbf{H}^{pixel}$. The spectrum of singular values was computed for all system matrices using the Matlab programming environment [73].

Figures 2.2 - 2.4 display the computed normalized singular value spectra. Figure 2.2 shows the normalized singular spectra for the different system matrices $\mathbf{H}^{pixel}$ for the three different weighting kernels. The matrix constructed by use of the cubic spline kernel is the most ill-conditioned, while the system matrix constructed by use of the linear kernel is the least ill-conditioned. This behavior is expected since the cubic spline kernel imposes the most smoothness on the data, followed by the quadratic spline and linear kernels.

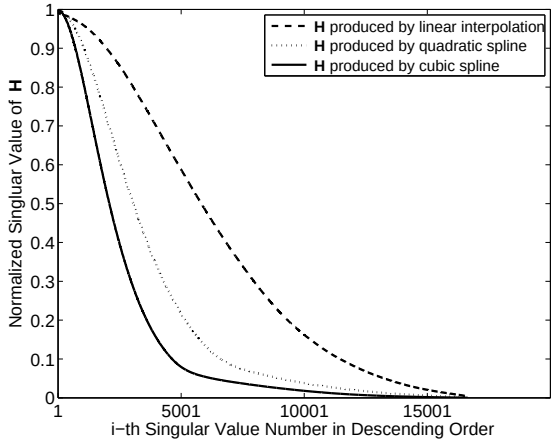

Figure 2.2: Singular value spectra associated with the system matrices H^{pixel} with pixel size 50μm.

The spectra for the blob system matrices are shown in Figs. 2.3 and 2.4. Figure 2.3 displays the spectra when the blobs had a relative radius $a = 1.5$ and varying shape parameter α. These results indicate that the parameter α will generally affect the stability of the system matrix. In this case, $\alpha = 2.0$ corresponds to the most poorly conditioned system matrix while $\alpha = 10.4$ corresponds to the best conditioned system matrix. The spectra for the case when the blob relative radius a was increased to 2 (physical size 100 μm) are displayed in Fig. 2.4. The parameter α is again observed to have a significant effect on the stability of the system matrices. The system matrix corresponding to $\alpha = 2$ is the most ill-conditioned, while the one corresponding to $\alpha = 10.4$ is the least ill-conditioned. In order to gain insight

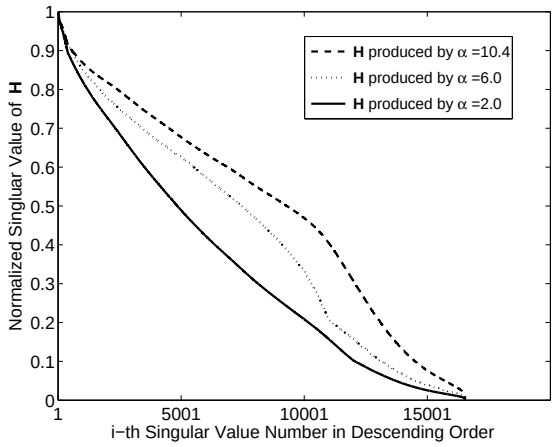

Figure 2.3: Singular value spectra associated with the system matrices H^{blob} with $m = 2$, relative radius a = 1.5 (physical size 75μm).

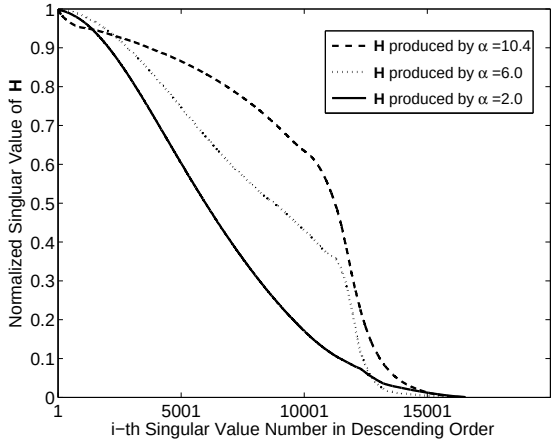

Figure 2.4: Singular value spectra associated with the system matrices H^{blob} with $m = 2$, relative radius a = 2 (physical size 100μm).

into this behavior, one can examine the normalized differential projection profile of one blob as shown in Fig. 2.5. One observes that the profile is more localized when α increases from 2 to 10.4, which results in a better conditioned system matrix.

In order to facilitate the comparison of the pixel- and blob-based results, the three highest singular value spectra from Figs. 3-5 were re-plotted together in Fig. 2.6. Two of these spectra correspond to different $\mathbf{H}^{blob}$ with $\alpha = 10.4$. and relative radius $a = 1.5$ and $a = 2$

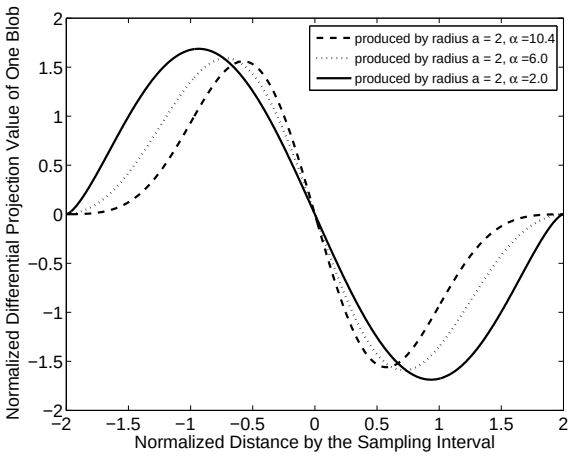

Figure 2.5: Profiles of the differential projection value of one blob with $m = 2$, relative radius a = 2.

and the third to $\mathbf{H}^{pixel}$ employing the linear weighting kernel. The two blob-based spectra possess a slower rate of decay than the pixel-based spectra, indicating that that the blob-based system matrices will yield more stable reconstruction problems than will pixel-based ones.

2.4.2 Simulation data and image reconstruction algorithm

Computer-simulation studies were conducted to investigate the trade-offs between image variance and spatial resolution for images reconstructed by use of the different system matrices. The 2D numerical phantom displayed in Fig. 2.7 was employed to represent our object function $\delta(\mathbf{r}_2; z)$. The physical size of the phantom was 25.6 mm $\times$ 25.6 mm. The phantom was composed of nine uniform disks possessing different values and physical sizes, which were blurred with a Gaussian kernel of width 0.15 mm. From knowledge of the phantom, the elements of the differential projection data $\mathbf{g}$ were computed analytically. The scanning geometry employed assumed 180 tomographic views that were uniformly spaced over a π angular range. At each view, the detector was assumed to possess 1024 elements of pitch 25 μm.

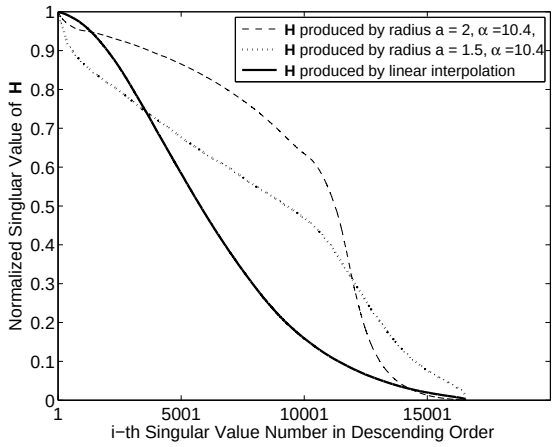

Figure 2.6: The three highest singular value spectra are replotted for comparison. Two of the spectra correspond to H^{blob} with $\alpha = 10.4$, relative radius a = 1.5 and a = 2. The third spectra corresponds to H^{pixel} based on the linear weighting kernel.

There are several sources of noise in X-ray DPCT [137] that include phase stepping jitter, quantum noise, and noise from the detection electronics. One hundred noisy data vectors were computed as realizations of an uncorrelated zero-mean Gaussian random vector [91]. The standard deviation σ_n of each element of the random vector was constant and was set according to the rule $\sigma_n = 0.2|\mathbf{g}|_{mean}$, where $|\mathbf{g}|_{mean} = \frac{1}{M}\sum_{m=1}^{M}|g_m|$ with g_m denoting the *m-th* component of the noiseless data vector $\mathbf{g}$.

From the 100 noisy differential projection data vectors, the penalized least-squares (PLS) algorithm described in reference [54] was employed to reconstruct 100 noisy coefficient estimates $\hat{\mathbf{b}}$. The analytic solution of the PLS algorithm with L_2 regularization can be written as a pseudo-inverse operator $\mathbf{H}^+$ acting on $\mathbf{g}$. The pseudo-inverse operator $\mathbf{H}^+$ can be decomposed as a linear combination of certain outer-product operators, whose coefficients are the reciprocals of the singular values of the operator $\mathbf{H}$ [12, 18] that were analyzed in Sec. 2.4.1. The estimates $\hat{\mathbf{b}}$ represent approximate solutions of the optimization program

$$\hat{\mathbf{b}} = \arg\min_{\mathbf{b}} ||\mathbf{g} - \mathbf{H}\mathbf{b}|| + \gamma L(\mathbf{b}), \tag{2.22}$$

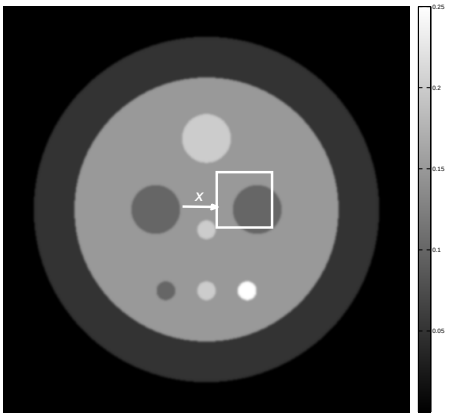

Figure 2.7: The numerical phantom employed in our simulation studies with an ROI indicated

where γ is a regularization parameter,

$$L(\mathbf{b}) = \sum_{n=0}^{N-1} \sum_{k \in \mathcal{N}_n} \left([\mathbf{b}]_n - [\mathbf{b}]_k \right)^2, \tag{2.23}$$

with the set $\mathcal{N}_n$ containing the index values of the four neighbour points of the nth value of $\mathbf{b}$. From knowledge of $\hat{\mathbf{b}}$, estimates of the object function $\delta_a(\mathbf{r}_2; z)$ were obtained by use of Eq. (3.6). For the cases where blob expansion functions were employed, the estimates of $\delta_a(\mathbf{r}_2; z)$ were sampled by use of a 2D Dirac delta sampling function onto a Cartesian grid and the resulting values stored as a matrix for analysis and display.

Sets of images were reconstructed by use of different system matrices $\mathbf{H}^{pixel}$ or $\mathbf{H}^{blob}$. For the pixel-based studies, the object was represented by a 512×512 pixel array with a 50 μm pitch. Three different pixel-based matrices $\mathbf{H}^{pixel}$ were constructed corresponding to the weighting kernel functions described in Sec. 2.3.1. For the blob-based studies, six different system matrices were employed that corresponded to blob parameters relative radius a = 1.5 (physical size 75 μm), relative radius a = 2 (physical size 100 μm), and $\alpha = 2, 6$, or 10.4. In all cases, 512×512 blobs were employed to represent the object function and the distance (sampling interval) between the blobs was 50 μm. For each system matrix, five sets of 100

noisy images were reconstructed for distinct values of the regularization parameter specified by $\gamma = 10, 200, 1000, 2000$, or 5000.

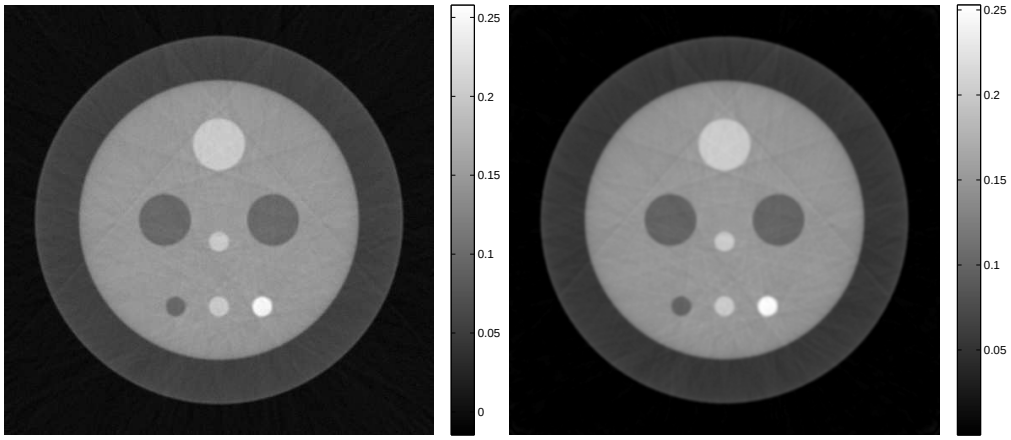

(a) (b)

Figure 2.8: Examples of reconstructed images by use of PLS algorithms based on pixel system matrix H^{pixel} and blob system matrix H^{blob}. Regularization parameter $\gamma = 10$ for both cases. (a) An reconstructed image produced by pixel system matrix with linear interpolation . (b) An reconstructed image produced by blobs with relative radius a = 2 (physical size $100\mu m$), $m = 2$ and $\alpha = 10.4$.

Computer-simulation studies were conducted to validate our reconstruction algorithm implementations that utilized the system matrices $\mathbf{H}^{pixel}$ and $\mathbf{H}^{blob}$. Example images reconstructed from noisy data sets by use of $\mathbf{H}^{pixel}$ and $\mathbf{H}^{blob}$ are shown in Figs. 2.8-(a) and (b). The system matrix $\mathbf{H}^{pixel}$ utilized linear interpolation and $\mathbf{H}^{blob}$ utilized blob parameters relative radius $a = 2$, $m = 2$, and $\alpha = 10.4$. The regularization parameter was set at $\gamma = 10$ for both cases. Horizontal profiles through the centers of the images in Figs. 2.8-(a) and (b) are shown in Fig. 2.9. The solid blue line (pixel-based result) appears to overshoot some of the boundaries and has more oscillations than the dashed red line (blob-based result). Note that the grey levels of the true object were recovered with good fidelity due to the fact that the object was contained within the field-of-view of the simulated imaging system and therefore there was no truncation of the data function with respect to the detector coordinate.

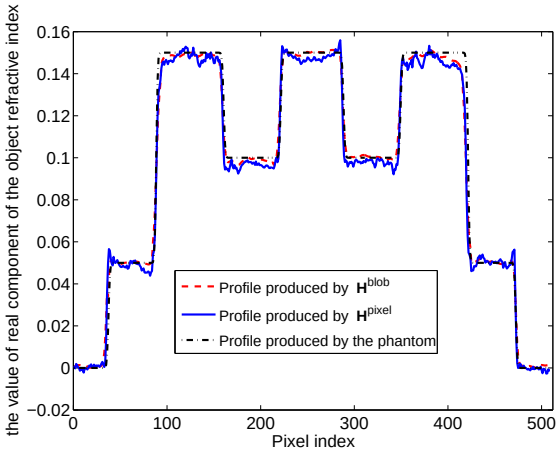

Figure 2.9: (Color online) Profiles through the center row of the reconstructed images in Fig. 2.8. The solid blue line corresponds to Fig.2.8-(a). The dashed red and dashdotted black lines correspond to Fig.2.8-(b) and the true phantom.

2.4.3 Empirical determination of image statistics and resolution measures

For each combination of system matrix and regularization parameter, the mean image and image variance were estimated [3] from the associated set of 100 noisy images within the 70×70 pixel region-of-interest (ROI) indicated by the white box in Fig. 2.7. The average value of the image variance map was computed to establish a scalar summary measure of the variance associated with the ROI. To quantify the spatial resolution, we fitted the profile in the mean image corresponding to the boundary indicated in Fig. 2.7. The profile was fit to a cumulative Gaussian function [180]:

$$G(x) = I_1 + \frac{I_2 - I_1}{2}\Big(1 + \mathrm{erf}\big(\frac{x-\mu}{\sigma\sqrt{2}}\big)\Big), \tag{2.24}$$

where x denotes the coordinate along the image profile, I_1 and I_2 indicate the image values on the two sides of the boundary with $I_1 < I_2$, μ is the true boundary location, and $\mathrm{erf}(x)$ is the error function, and σ is the associated standard deviation. We adopted the full-width at half-maximum (FWHM) value of the fitted error function as a summary measure of spatial resolution [180] at that location in image space, with smaller values indicating higher spatial resolution. Repeating these procedures for different choices of the regularization parameter γ

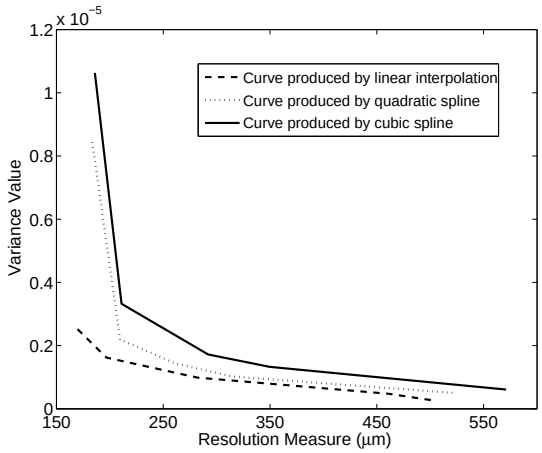

Figure 2.10: Variance versus resolution curves corresponding to use of the system matrices H^{pixel}.

produced a collection of (variance, FWHM) pairs for each system matrix, which were plotted to characterize the trade-offs between spatial resolution and noise levels in the reconstructed images.

The variance-resolution curves for the pixel- and blob-based system matrices are shown in Figs. 2.10 and 2.11, respectively. The left-most point on each curve corresponds to $\gamma = 10$, while the right-most point on each curve corresponds to $\gamma = 5000$. As expected, when the value of γ increases, the image variance decreases at the cost of spatial resolution.

For the pixel-based case, Fig. 2.10 reveals that the curve corresponding to the use of a linear weighting kernel is the lowest, followed by those corresponding to the quadratic and cubic spline kernels. Stated otherwise, the use of the linear interpolation-based system matrix $\mathbf{H}^{pixel}$ produced images with smaller variances at any of the attained spatial resolution values than did the other two system matrices. These observations are consistent with the singular value spectra displayed in Fig. 2.2, where the linear and cubic spline-based system matrices were demonstrated to yield the best and worst, respectively, conditioned system matrices for the pixel-based studies.

For the blob-based cases shown in Fig. 2.11, the variance-resolution curves corresponding to the shape parameter $\alpha = 10.4$ were lower than those corresponding to the other α values for both relative radius $a = 1.5$ [Fig. 2.11-(a)] and relative radius $a = 2$ [Fig. 2.11-(b)]. The

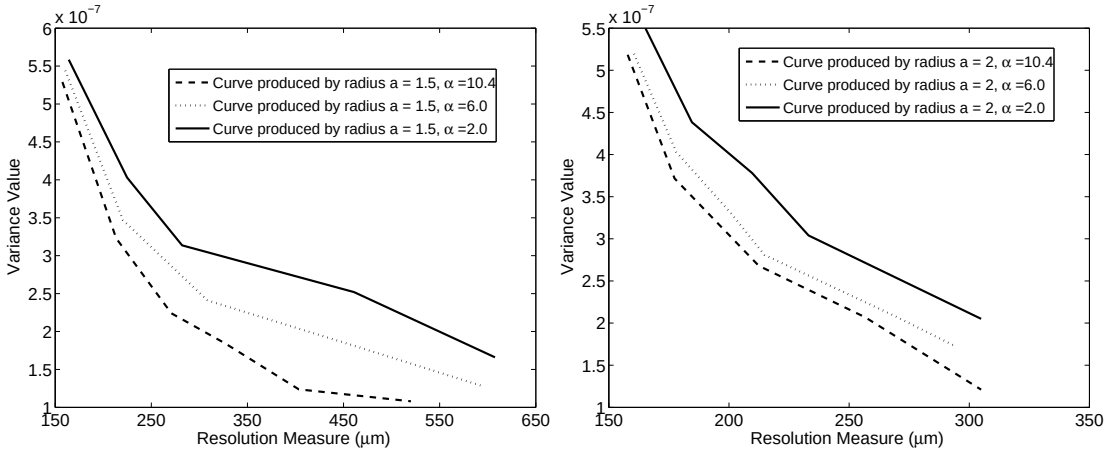

(a) height=5cm (b) height=5cm

Figure 2.11: Variance versus resolution curves corresponding to use of the system matrices H^{blob}. (a) Curves are produced by blobs with relative radius $a = 1.5$ (physical size $75\mu m$), $m = 2$ and varying α. (b) Curves are produced by blobs with relative radius $a = 2$ (physical size $100\mu m$), $m = 2$ and varying α.

curves corresponding to the shape parameter $\alpha = 2.0$ were higher than the others for both values of a. These observation are consistent with the singular value spectra displayed in Figs. 2.3 and 2.4, where the system matrices $\mathbf{H}^{blob}$ corresponding to $\alpha = 10.4$ and $\alpha = 2.0$ were demonstrated to yield the best and worst, respectively, conditioned system matrices for the blob-based studies.

In order to facilitate the comparison of the pixel- and blob-based results, the three best variance-resolution curves from Figs. 2.10 and 2.11 were superimposed and replotted in Fig. 2.12. Two of these curves correspond to different $\mathbf{H}^{blob}$ with $\alpha = 10.4$ and relative radius $a = 1.5$ and relative radius $a = 2$ and the third to $\mathbf{H}^{pixel}$ employing the linear weighting kernel. The two blob-based curves are everywhere lower than the pixel-based curve, indicating images produced by use of $\mathbf{H}^{blob}$ can possess improved variance-resolution trade offs than those produced by use of $\mathbf{H}^{pixel}$. Below we demonstrate and investigate the use of $\mathbf{H}^{blob}$ for reconstructing images of biological tissue from few-view experimental differential projection data.

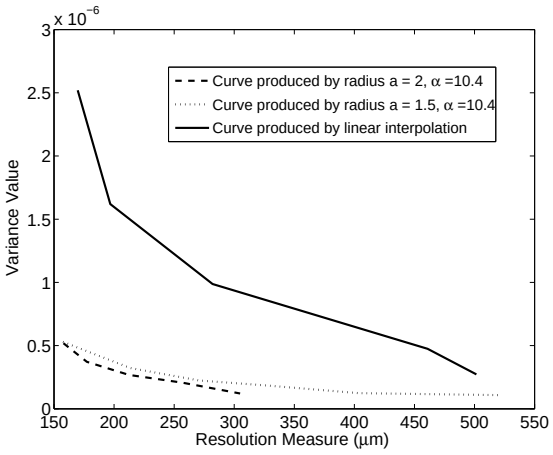

Figure 2.12: The three best variance-resolution curves picked from the pixel and blob cases.

2.5 Application to few-view image reconstruction

2.5.1 Experimental data and image reconstruction algorithm

In our studies of few-view image reconstruction, we utilized experimental DPCT data that were acquired previously [107] using a grating-based phase-contrast imaging system at the Swiss Light Source. A tissue sample corresponding to a rat brain was the imaged object. The tomographic scanning consisted of 720 tomographic view angles that were uniformly distributed over a 180 degree angular range. The differential projection data contained 1621 samples at each view angle corresponding to a detector pitch of 7μm. In the studies described below, certain subsets of these data were employed for few-view image reconstruction. A phase-stepping procedure was employed, which utilized four steps, to compute the differential projection data at each tomographic view angle. We refer the reader to reference [107] for additional details regarding the data-acquisition and sample preparation.

To obtain an estimate of the object function based on Eq. (2.20), the constrained, total variation minimization (TV) program [28, 29, 149] was employed:

$$\hat{\mathbf{b}} = \arg\min_{\mathbf{b}} \|\mathbf{b}\|_{\text{TV}} \quad \text{s.t.} \quad |\mathbf{g} - \mathbf{H}^{blob}\mathbf{b}| \leq \epsilon, \tag{2.25}$$

in which $\|\mathbf{b}\|_{\text{TV}}$ represents the TV norm of the vector $\mathbf{b}$ and ϵ is the specified data tolerance. It has been demonstrated that this image reconstruction strategy can be highly effective at mitigating data-incompleteness for certain classes of objects [71,149,151,174]. The adaptive steepest-descent-projection onto convex sets (ASD-POCS) algorithm proposed by Sidky and Pan [151] was employed to determine approximate solutions of Eq. (2.25). Details regarding this algorithm and its implementation can be found in reference [151]. The system matrix $\mathbf{H}^{blob}$ with $m = 2$, relative radius a = 2 (physical size 14μm, which is twice the sampling interval 7μm) and $\alpha = 10.4$ was constructed as described in Sec. 2.3.2. The values of the data tolerance ϵ employed were 43.8 and 58.2 for the reconstruction problems involving 90 and 180 view angles, respectively. From knowledge of $\hat{\mathbf{b}}$, estimates of $\delta_a(\mathbf{r}_2; z)$ were obtained by use of Eq. (3.6) and were subsequently sampled by use of a 2D Dirac delta sampling function with a period of 7 μm onto a Cartesian grid for display. Because it is commonly employed in current applications of DPCT, we also reconstructed images by use of a modified FBP algorithm that acts directly on the differential projection data [51].

2.5.2 Reconstructed images

The images reconstructed by use of the FBP algorithm and the TV algorithm from 90 view angles are displayed in Figs. 2.13-(a) and (b). The corresponding images reconstructed from 180 view angles are displayed in Fig. 2.14. All of the images are displayed in the same grey scale window. The images reconstructed by use of the FBP algorithm [Figs. 2.13-(a) and 2.14-(a)] have streak artifacts due to the limited number of view angles employed, while those artifacts are suppressed in the images reconstructed by use of the ASD-POCS algorithm [Figs. 2.13-(b) and 2.14-(b)]. Because the object was embedded in a container that did not fit entirely in the field-of-view, there was effectively projection truncation. Therefore, we expect that our reconstruction algorithm will reconstruct $\delta(\mathbf{r})$ only up to a constant. Because the true values of $\delta(\mathbf{r})$ were not available, we did not investigate this. All the images presented were normalized into the same scale.

In order to more easily visualize differences in the reconstructed images, two ROIs indicated by black dashed boxes in Fig. 2.13-(a) were displayed. Figures 2.15-(a) and (b) display the smaller ROIs corresponding to images in Figs. 2.13-(a) and (b), respectively, for the 90 view angle case. Subfigure (c) displays the smaller ROI extracted from an FBP image

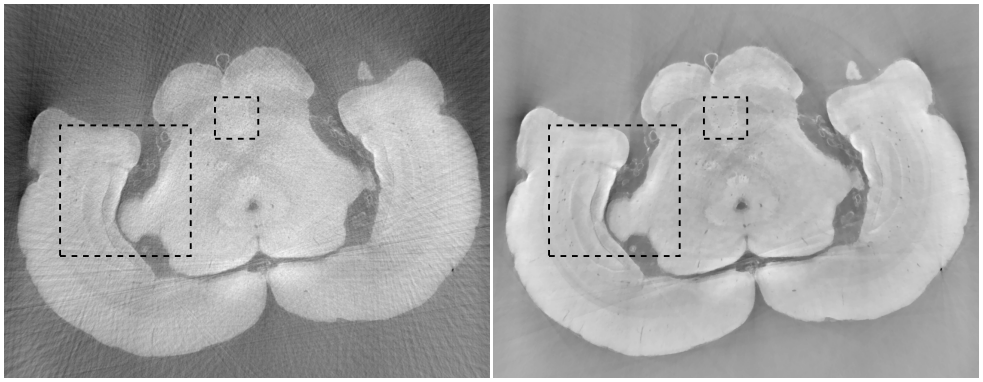

(a) (b)

Figure 2.13: Images reconstructed from 90 projections by use of the (a) FBP (b) ASD-POCS algorithm. The dashed boxes indicate two ROIs chosen for comparison. All images are displayed in the same grey scale window [0 1].

reconstructed from 720 view angles, which serves as a reference image. Figures 2.16-(a) and (b) display the smaller ROIs corresponding to Figs. 2.14-(a) and (b), respectively, for the 180 view angle case. Figure 2.16-(c) displays the smaller ROI from the FBP reference image. As shown in Fig. 2.15-(a) the visual appearance of the image reconstructed by use of the FBP algorithm from 90 projections is significantly degraded by noise and other artifacts. Some of the blood vessels (dark hole-like structures) may be difficult to detect due to the high artifact and noise levels in these image. The images reconstructed by use of the ASD-POCS algorithm from 90 tomographic views, shown in Figs. 2.15-(b) has significantly reduced noise and artifact levels and possesses a visual appearance similar to the reference image that was reconstructed from the complete data set containing 720 views. Similar observations hold for the smaller ROI images corresponding to the 180 view angle case displayed in Fig. 2.16.

The larger ROIs are shown in Figs. 2.17 and 2.18. Figures 2.17-(a) and (b) display the larger ROIs corresponding to images in Figs. 2.13-(a) and (b), respectively, for the 90 view angle case. Subfigure (c) displays the larger ROI extracted from the FBP image reconstructed from 720 view angles, which again serves as a reference image. Figures 2.18-(a) and (b) display the larger ROIs corresponding to images in Figs. 2.14-(a) and (b), respectively, for the 180 view angle case. Subfigure (c) displays the larger ROI from the FBP reference image.

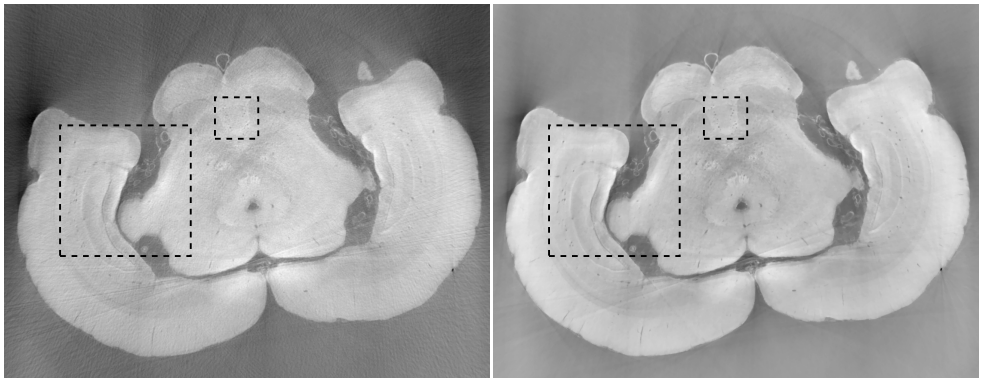

(a) (b)

Figure 2.14: Images reconstructed from 180 projections by use of the (a) FBP (b) ASD-POCS algorithm Two dashed boxes indicate two ROIs chosen for comparison. All images are displayed in the same grey scale window [0 1].

Again, we observe that the images reconstructed by use of the ASD-POCS algorithm from 90 tomographic views, shown in Figs. 2.17-(b) has significantly reduced noise and artifact levels and possesses a visual appearance similar to the reference image that was reconstructed from the complete data set containing 720 views. Similar observations hold for the larger ROI images corresponding to the 180 view angle case displayed in Fig. 2.18.

2.6 Summary

We have analyzed the numerical and statistical properties of two classes of discrete imaging models that form the basis for iterative image reconstruction in DPCT [177]. The models differ in the choice of expansion functions that were utilized to discretize the sought-after object function. The models based on Kaiser-Bessel window functions ("blobs") were demonstrated to produced images that possess more favorable variance-resolution trade-offs than images reconstructed by use of pixel-based imaging models. This observation was consistent with the results of an SVD analysis of the system matrices, which demonstrated that the blob-based system matrices can yield more stable reconstruction problems than do pixel-based ones.

(a) (b) (c)

Figure 2.15: Zoomed-in images of the smaller ROIs denoted in Figs. 2.13-(a) and (b), reconstructed from 90 view angles, are displayed in subfigures (a) and (b). Subfigure (c) displays the corresponding reference ROI corresponding to an image reconstructed from 720 projections by use of a DPCT FBP algorithm. All images are displayed in the same grey scale window [0 1] .

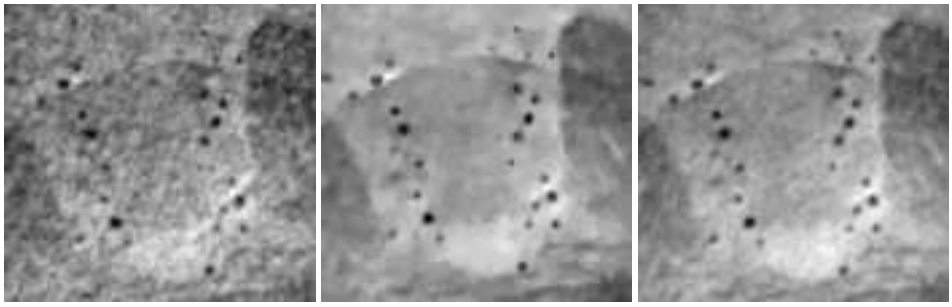

(a) (b) (c)

Figure 2.16: Zoomed-in images of the smaller ROIs denoted in Figs. 2.14-(a) and (b), reconstructed from 180 view angles, are displayed in subfigures (a) and (b). Subfigure (c) displays the corresponding reference ROI corresponding to an image reconstructed from 720 projections by use of a DPCT FBP algorithm. All images are displayed in the same grey scale window [0 1] .

A reconstruction algorithm that seeks solutions of a constrained TV minimization optimization program was employed with a blob-based imaging model for few-view image reconstruction. By use of few-view experimental data, it was demonstrated that this algorithm can produce images with significantly weaker artifacts and lower noise levels than the FBP algorithm that has been utilized the majority of previously published studies. To our knowledge,

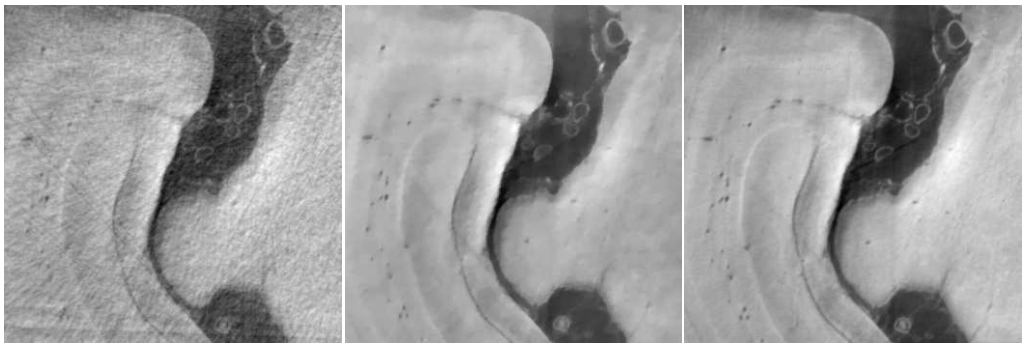

(a) (b) (c)

Figure 2.17: Zoomed-in images of the larger ROIs denoted in Figs. 2.13-(a) and (b), reconstructed from 90 view angles, are displayed in subfigures (a) and (b). Subfigure (c) displays the corresponding reference ROI corresponding to an image reconstructed from 720 projections by use of a DPCT FBP algorithm. All images are displayed in the same grey scale window [0 1] .

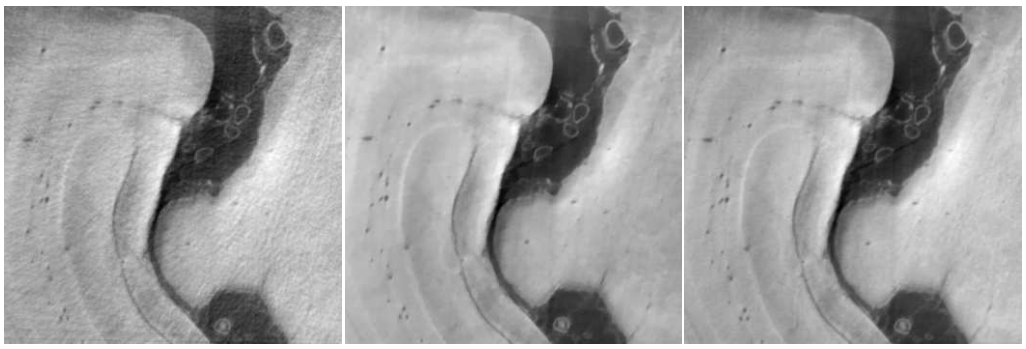

(a) (b) (c)

Figure 2.18: Zoomed-in images of the larger ROIs denoted in Figs. 2.14-(a) and (b), reconstructed from 180 view angles, are displayed in subfigures (a) and (b). Subfigure (c) displays the corresponding reference ROI corresponding to an image reconstructed from 720 projections by use of a DPCT FBP algorithm. All images are displayed in the same grey scale window [0 1].

this was the first published application of an iterative reconstruction method in X-ray DPCT for reconstruction of a biological specimen [177]. We expect that the findings of our study will benefit the continued development of DPCT imaging systems by permitting reduction

of data-acquisition times and radiation doses. Future research efforts will be required to identify blob parameters that are optimal for specific imaging tasks.

Chapter 3

A multi-channel image reconstruction method for grating-based X-ray phase-contrast computed tomography

3.1 Introduction

Grating-based X-ray phase-contrast tomography (GB-XPCT) is an emerging modality that can produce volumetric images that depict three different object properties: X-ray absorption, scattering, and refractive index. Medical imaging applications of GB-XPCT are limited by long data-acquisition times and relatively high radiation doses. A natural way to mitigate these problems is to reduce exposure times and/or the number of tomographic views at which data are acquired. From such data, statistically-principled algorithms can be employed for image reconstruction. Several iterative image reconstruction algorithms for GB-XPCT have been proposed [90, 120, 121, 177]. However, to the best of our knowledge, none of the methods investigated to date take full advantage of the second order statistical properties of the sinogram data corresponding to the three object properties.

In this work, an advanced multi-channel (MC) image reconstruction algorithm for GB-XPCT is proposed and investigated [175]. This method operates by concurrently, rather than independently as is done conventionally, reconstructing tomographic images of the three object properties (absorption, scattering, refractive index). In this way, the 2nd order statistical properties of the object property sinograms, including correlations between them, can be

fully exploited to improve the variance vs. resolution tradeoff of the reconstructed images as compared to existing methods.

3.2 Basic principles of GB-XPCT

The canonical GB-XPCT imaging geometry is shown in Fig. 3.1. The imaging system assumes a coherent X-ray source and utilizes a Talbot interferometer consisting of a phase grating G1 and an absorption grating G2. The phase grating G1 approximately splits the incident X-ray beam into its first two diffraction orders. Based on the Talbot effect [65, 156], a periodic interference pattern will be formed in planes corresponding the Talbot distances, one of which corresponds to the plane containing G2. An object placed in front of the phase grating G1 will produce slight refraction and therefore distort the original wavefront. The distortion results in variations of the locally transmitted intensity behind the absorption grating G2. When the phase grating G1 is displaced along the transverse direction x_g, the recorded intensity for each detector pixel can be approximately described as

$$I(s,h,x_g) \approx A(s,h)\sin\left(2\pi\frac{x_g}{p_2}+\varphi(s,h)\right)+\bar{I}(s,h). \tag{3.1}$$

Here, (s,h) specifies a pixel location on the 2D detector, x_g is the location of the phase grating G1, p_2 is the period of the absorption grating G2, $A(s,h)$ represents the amplitude coefficient for the sinusoid function and relates to the scattering strength of the object, $\varphi(s,h)$ represents the phase coefficient and is proportional to the gradient of the projected object phase, and $\bar{I}(s,h)$ represents the average intensity for the sinusoid function and can be treated as a measurement from convertional X-ray radiography.

To obtain seperate estimates of the amplitude coefficient $A(s,h)$, the phase coefficient $\varphi(s,h)$ and the average intensity $\bar{I}(s,h)$, a phase stepping procedure is generally conducted [169]. The phase grating G1 is scanned transversely along the direction x_g to acquire projections for evenly spaced positions to cover at least one period of the grating G2. In this case, a series of $\bar{I}(s,h,x_g)$ can be obtained at different locations x_g. A Fourier series analysis or a least squares algorithm can be directly employed to obtain the three different images, which will be discussed below, by use of those projections acquired at evenly spaced steps [169].

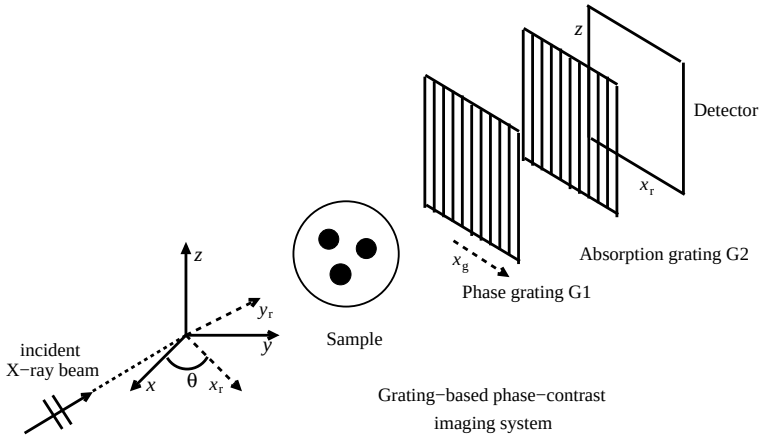

Figure 3.1: A schematic of grating-based phase-contrast imaging system.

The normalized average transmission image for each pixel can be formulated as

$$T(s,h) = \frac{\bar{I}_{obj}(s,h)}{\bar{I}_{ref}(s,h)}, \tag{3.2}$$

where the superscript *obj* and *ref* denote the values measured when the object is present and absent, respectively. The calculated $T(s,h)$ can be treated as the normalized measurement conducted with conventional X-ray radiography.

The dark-field image [132] that reflects the small-angle (and ultra-small) X-ray scattering (SAXS) property of the object can also be obtained with this grating-based setup. The scattering information of the object is embedded in the higher orders of the oscillation pattern. When X-rays are reflected or scattered by the inhomogeneities of the object, the amplitude coefficient $A(s,h)$ of the sinusoidal function will be decreased. A quantitative expression for the normalized dark-field signal [13, 132] is given by

$$V(s,h) = \frac{V_{obj}(s,h)}{V_{ref}(s,h)} = \frac{A_{obj}(s,h)/\bar{I}_{obj}(s,h)}{A_{ref}(s,h)/\bar{I}_{ref}(s,h)} = \frac{A_{obj}(s,h)\bar{I}_{ref}(s,h)}{A_{ref}(s,h)\bar{I}_{obj}(s,h)}. \tag{3.3}$$

When the imaged object contains inhomogeneities, it will produce strong SAXS signals and cause significant decrease of visibility. In gereral, the quantity $V(s,h)$ can be considered as an inverse measure for the SAXS signal strength of the object.

The differential phase-contrast image [112, 133], which represents the gradient of the projected phase profile $\Phi(s,h)$ of the object, can also be estimated. It is determined by the phase coefficient of the oscillation curve at each pixel $\varphi(s,h)$ as

$$\frac{\lambda d}{p_2}\nabla_{x_g}\Phi(s,h) = \varphi_{ref}(s,h) - \varphi_{obj}(s,h), \tag{3.4}$$

where ∇_{x_g} is a gradient operator along the direction x_g which is perperdicular to the incident X-ray beams and λ is the wavelength. The differential phase-contrast image permits the visualization of objects that present very low absorption contrast.

3.3 Methods

3.3.1 Discrete imaging models for GB-XPCT

All three extracted projection images can be directly linked to three physical properties of the object. When tomography is performed, three images that depict the object properties can be reconstructed. We will utilize the parallel-beam tomographic scanning geometry shown in Fig. 3.1. However, the results that follow can readily be adapted to the case of spherical wave illumination in the paraxial limit [49]. The rotation axis of the tomographic scanning is defined by the z-axis of the reference coordinate system (x,y,z). The rotated coordinate system (x_r, y_r, z) is related to the reference system by $x_r = x\cos\theta + y\sin\theta, y_r = y\cos\theta - x\sin\theta$, where $\theta \in [0,\pi)$ is the tomographic view angle measured from the positive x-axis. A phase-amplitude object positioned at the origin is irradiated by an X-ray plane-wave with wavelength λ, or equivalently wavenumber $k = \frac{2\pi}{\lambda}$, which propagates in the direction of the positive y_r-axis.

Let $n(x,y,z) = 1 - \delta(x,y,z) + i\beta(x,y,z)$ denote the complex refractive index distribution of the object, where $\delta(x,y,z)$ is the real-valued refractive index distribution and $\beta(x,y,z)$ is the absorption index of the object. In addtiion, let $\mu_{saxs}(x,y,z)$ be the parameter related to the strength of the SAXS produced by the object. It has been shown that $\mu_{saxs}(x,y,z)$ is directly proportional to the small-angle scattering cross section and the number density of the small-angle scatters of the object [35]. We will employ the notation $\delta(\mathbf{r}_2; z) \equiv \delta(x,y,z)$,

$\beta(\mathbf{r}_2; z) \equiv \beta(x, y, z)$ and $\mu_{saxs}(\mathbf{r}_2; z) \equiv \mu_{saxs}(x, y, z)$, where $\mathbf{r}_2 = (x, y)$, as a convenient description of one transverse slice of the 3D object function. The discrete image model for the projected absorption is briefly discussed first and the discrete image models for the dark-field and the differential phase are presented subsequently.

When a digital detector is employed, the measured intensity data and associated data function correspond to an ordered collection of numbers. When a parallel-beam tomographic geometry is adopted, the reconstructed problem is inherently 2D. We will only consider the problem of reconstructing a transverse slice of the object function located at a fixed $z = h\Delta_d$ position, where Δ_d denotes the detector pixel size. The projected absorption image relates to the Radon transform of the absorption index $\beta(\mathbf{r}_2, z)$ and we will denote the discrete data function as

$$g_1[s, t; h] = -\ln T(s, t; h) \approx \frac{4\pi}{\lambda}\big(\mathbf{R}\beta(\mathbf{r}_2; z = h\Delta_d)\big)(x_r, \theta)\Big|_{x_r = s\Delta_d, \theta = t\Delta_\theta}, \tag{3.5}$$

where s and h are integer-valued detector element indices and t is the tomographic view index, T has the same meaning with the one in Eq. (3.2), $\mathbf{R}$ denotes the 2D Radon transform operator, and the quantity Δ_θ denotes the angular sampling interval between the uniformly distributed view angles.

To develop iterative image reconstruction algorithms, a finite-dimensional approximate representation of the object function is required for most cases. A general linear N-dimensional approximation of $\beta(\mathbf{r}_2; z = h\Delta_d)$ can be formed as

$$\beta_a(\mathbf{r}_2; z = h\Delta_d) = \sum_{n=0}^{N-1} b_1^n \phi_n(\mathbf{r}_2), \tag{3.6}$$

where the subscript a indicates that $\beta_a(\mathbf{r_2}; z = h\Delta_d)$ is an approximation of $\beta(\mathbf{r}_2; z = h\Delta_d)$, $\{\phi_n(\mathbf{r}_2)\}$ are a set of expansion functions, and $\{b_1^n\}$ are the corresponding expansion coefficients that depend on the slice index h. The discrete data function satisfies

$$g_1[s, t; h] = -\ln T(s, t; h) \approx \frac{4\pi}{\lambda}\mathbf{R}\beta_a(\mathbf{r}_2; z = h\Delta_d) = \frac{4\pi}{\lambda}\sum_{n=0}^{N-1} b_1^n \big(\mathbf{R}\phi_n(\mathbf{r}_2)\big)(x_r, \theta)\Big|_{x_r = s\Delta_d, \theta = t\Delta_\theta}, \tag{3.7}$$

Let the vector $\mathbf{g}_1 \in \mathbb{R}^M$ denote a lexicographically ordered representation of $g_1[s,t;h]$. The dimension M is defined by the product of the number of detector row elements and the number of view angles. In matrix form, Eq. (3.7) can be expressed as

$$\mathbf{g}_1 = \mathbf{H}_1 \mathbf{b}_1, \tag{3.8}$$

where $\mathbf{H}_1$ is an $M \times N$ system matrix for the absorption model, and $\mathbf{b}_1$ is a $N \times 1$ vector of expansion coefficients whose n-th element is given by b_1^n. The explicit forms for the system matrix $\mathbf{H}_1$ will be determined by specifying the expansion functions $\phi_n(\mathbf{r}_2)$. Kaier-Bessel window expansion functions, referred to hereafter as "blobs" [96, 97], were employed in our study since the Radon transform operators and their derivatives [90, 177] can be analytically computed for these blobs functions. In addition, based on previous studies in computed tomography [96, 97] and our previous study [177] (see Chapter 2) for differential phase contrast tomography, blobs have shown some advantages in representing the object functions.

The blob expansion functions are defined as

$$\phi_n^{blob}(\mathbf{r}_2; m, a, \alpha) = \begin{cases} \frac{\left[\sqrt{1-(r_b/a)^2}\right]^m I_m[\alpha\sqrt{1-(r_b/a)^2}]}{I_m(\alpha)}, & \mathbf{r}_b \leq a \\ 0, & \text{otherwise}, \end{cases} \tag{3.9}$$

where $I_m(\cdot)$ is the *m-th* order modified Bessel function, $\mathbf{r}_b \equiv |\mathbf{r}_2 - \mathbf{r}_n|$ with $\mathbf{r}_n = (x_n, y_n)$ denoting the blob center, and a and α determine the blob's radius and specific shape. Let $\xi \equiv x_r - x_n \cos\theta - y_n \sin\theta$. As demonstrated by Lewitt [96], the 2D Radon transform of one blob function is given by

$$\mathbf{R}\phi_n^{blob}(\mathbf{r}_2; m, a, \alpha) = \frac{a}{I_m(\alpha)} \left(\frac{2\pi}{\alpha}\right)^{1/2} \left[\sqrt{1-(\xi/a)^2}\right]^{m+1/2} I_{m+1/2}\left(\alpha\sqrt{1-(\xi/a)^2}\right), \tag{3.10}$$

for $|\xi| \leq a$ and zero otherwise. By use of Eqs. (3.7) and (3.10), the discrete imaging model for the projected absorption property is given by

$$g_1[s,t;h] = -\ln T(s,t;h) \approx \frac{4\pi}{\lambda} \tag{3.11}$$

$$\times \sum_{n=0}^{N-1} \mathbf{b}_n \frac{a}{I_m(\alpha)} \left(\frac{2\pi}{\alpha}\right)^{1/2} \left[\sqrt{1-(\xi/a)^2}\right]^{m+1/2} I_{m+1/2}\left(\alpha\sqrt{1-(\xi/a)^2}\right)\Big|_{\xi=s\Delta_d - x_n\cos(t\Delta_\theta) - y_n\sin(t\Delta_\theta)}, \tag{3.12}$$

or, in the matrix-vector form,

$$\mathbf{g}_1 = \mathbf{H}_1 \mathbf{b}_1, \tag{3.13}$$

where

$$[\mathbf{H_1}]_{m',n} = [\mathbf{H}_1]_{m'=t\times S+s,\ n} = \frac{4\pi}{\lambda}\frac{a}{I_m(\alpha)}\left(\frac{2\pi}{\alpha}\right)^{1/2}$$

$$\times \left(\sqrt{1-(\xi/a)^2}\right)^{m+1/2} I_{m+1/2}\left(\alpha\sqrt{1-(\xi/a)^2}\right)\Big|_{\xi=s\Delta_d - x_n\cos(t\Delta_\theta) - y_n\sin(t\Delta_\theta)}, \tag{3.14}$$

and S is the total number of discrete projection data.

For the projected SAXS property, similar to the above analysis, the discrete data function is given by

$$g_2[s,t;h] = -\ln V(s,t;h) = \big(\mathbf{R}\mu_{saxs}(\mathbf{r}_2; z = h\Delta_d)\big)(x_r,\theta)\Big|_{x_r = s\Delta_d, \theta = t\Delta_\theta}, \tag{3.15}$$

where V has the same meaning with the one in Eq. (3.3). The same blobs expansion functions will be employed and the discrete image model is given in matrix form as,

$$\mathbf{g}_2 = \mathbf{H}_2 \mathbf{b}_2, \tag{3.16}$$

where $\mathbf{b}_2$ are the corresponding expansion coefficients and the system matrix is given by

$$[\mathbf{H_2}]_{m',n} = [\mathbf{H}_2]_{m'=t\times S+s,\ n} = \frac{a}{I_m(\alpha)}\left(\frac{2\pi}{\alpha}\right)^{1/2}$$

$$\times \left(\sqrt{1-(\xi/a)^2}\right)^{m+1/2} I_{m+1/2}\left(\alpha\sqrt{1-(\xi/a)^2}\right)\Big|_{\xi=s\Delta_d - x_n\cos(t\Delta_\theta) - y_n\sin(t\Delta_\theta)}. \tag{3.17}$$

For the differential phase image, the discrete data function is given as

$$g_3[s,t;h] = \varphi_{ref}(s,t;h) - \varphi_{obj}(s,t;h) = \frac{\lambda d}{p_2}\frac{\partial}{\partial x_r}\big(\mathbf{R}\delta(\mathbf{r}_2; z = h\Delta_d)\big)(x_r,\theta)\Big|_{x_r = s\Delta_d, \theta = t\Delta_\theta}, \quad (3.18)$$

where φ has the same meaning in Eq. (3.4). The same blobs expansion functions will be employed to represent $\delta(\mathbf{r}_2; z = h\Delta d)$. According to our previous study (see Chapter 2) [177], the discrete image model is given in matrix form as,

$$\mathbf{g}_3 = \mathbf{H}_3\mathbf{b}_3, \quad (3.19)$$

where $\mathbf{b}_3$ are the corresponding expansion coefficients and the system matrix is given by

$$[\mathbf{H}_3]_{m',n} = [\mathbf{H}_3]_{m'=t\times S+s,\ n} = -\frac{\lambda d}{p_2}\frac{(2\pi\alpha)^{1/2}}{I_m(\alpha)} \times \frac{\xi}{a}\left(\sqrt{1-(\xi/a)^2}\right)^{m-1/2} I_{m-1/2}\left(\alpha\sqrt{1-(\xi/a)^2}\right)\Big|_{\xi = s\Delta_d - x_n\cos(t\Delta_\theta) - y_n\sin(t\Delta_\theta)}. \quad (3.20)$$

Note that the k-th order spatial derivative of the Radon transform of these blobs is continuous when $m > k$ [96]. In our study, $m = 2$ was chosen and $\alpha = 10.4$. This ensures that the first-order derivatives of the blobs are continuous, and the blobs can produce a better representation of the object.

3.3.2 Interpretation of GB-XPCT as a MC reconstruction problem

To adopt standard image processing terminology, each of these three object properties will be associated with a 'channel'. The projected object properties corresponding to a collection of tomographic view angles will be referred to as the channel sinograms. Existing XPCT reconstruction approaches independently reconstruct each object property from knowledge of the associated channel sinogram. Because that reconstruction process involves only a single channel, it will be referred to as a single-channel (SC) approach. More specifically, from the discrete image models, the absorption property information $\mathbf{b}_1$, the phase information $\mathbf{b}_2$,

and SAXS information $\mathbf{b}_3$ will be independently reconstructed from their associated channel sinograms $\mathbf{g}_1$, $\mathbf{g}_2$ and $\mathbf{g}_3$.

An important observation is that, because these three sinograms are computed from the same phase-stepping data, statistical correlations exist between the channel sinograms. Because they ignore these cross-channel statistical correlations, SC reconstructions are statistically suboptimal. The MC approaches we describe below circumvent this limitation by jointly reconstructing the three object properties from knowledge of the three channel sinograms. By concurrently reconstructing the three object properties by use of an appropriately defined penalized weighted least squares (PWLS) estimator, the 2nd order statistical properties of the channel sinograms, including correlations between them, can be fully exploited to improve the variance vs. resolution tradeoff of the resulting images as compared to those obtained by use of SC methods. The advantages of MC image reconstruction and restoration are well known in the traditional image processing community but remain entirely unexplored within the context of XPCT imaging.

3.3.3 Description of MC image reconstruction methods

Let the lexicographically ordered vectors $\mathbf{g}_l \in \mathbb{R}^{M\times 1}$ and $\mathbf{b}_l \in \mathbb{R}^{N\times 1}$ represent the l-th channel ($l = 1, 2, 3$) sinogram and a discrete representation of the associated object property. The MC vectors $\mathbf{g} = (\mathbf{g}_1^T, \mathbf{g}_2^T, \mathbf{g}_3^T)^T$ and $\mathbf{b} = (\mathbf{b}_1^T, \mathbf{b}_2^T, \mathbf{b}_3^T)^T$ represent stacks of the three channel sinograms and object properties coefficients. The MC imaging model for GB-XPCT is given by $\mathbf{g} = \mathbf{H}\mathbf{b}$, where $\mathbf{H}$ is the MC imaging operator that is defined as

$$\mathbf{H} = \begin{bmatrix} \mathbf{H}_1 & \mathbf{0} & \mathbf{0} \\ \mathbf{0} & \mathbf{H_2} & \mathbf{0} \\ \mathbf{0} & \mathbf{0} & \mathbf{H_3} \end{bmatrix}.$$

Here, $\mathbf{H}_1$, $\mathbf{H_2}$ and $\mathbf{H_3}$ are defined in Eqs. (3.14), (3.17) and (3.20) and $\mathbf{0}$ denotes the $M \times N$ zero matrix.

We have developed and implemented novel MC image reconstruction algorithms that facilitate accurate XPCT imaging of the three object properties. In our approach, PWLS

estimates of $\mathbf{b}$ are computed by solving the optimization problem

$$\frac{1}{2}\|\mathbf{g}-\mathbf{H}\mathbf{b}\|^2_{\Sigma^{-1}}+R(\mathbf{b}) \quad \rightarrow \quad \min_{\mathbf{b}\in\mathbf{C}}\,, \tag{3.21}$$

where the set C is a closed convex subset of $\mathbb{R}^{3N\times 1}$ and may include additional constraints such as a non-negativity condition. The quantity $\|\cdot\|^2_{\Sigma^{-1}}$ denotes a weighted L_2-norm, where the weight matrix Σ^{-1} is the inverse of the MC covariance matrix corresponding to $\mathbf{g}$, which will be estimated as described below. In GB-XPCT, Σ is a non-diagonal block matrix with the off-diagonal block elements describing information about the noise correlations between the different channel sinograms.

The penalty term $R(\mathbf{b})$ was defined as

$$R(\mathbf{b})=\sum_{l=1}^{3}\sum_{n=1}^{N}\alpha_l\kappa_{ln}\psi\left(|[\nabla\mathbf{b}_l]_n|_{\ell^2}\right) \tag{3.22}$$

where α_l is the regularization parameter for the l-th channel, κ_{ln} are user-provided weights [58] that relate to the weight matrix Σ^{-1} in our study, $[\nabla\mathbf{b}]_n$ represents the $n-$th component of the discrete gradient of the vector $\mathbf{b}$, and $|\cdot|_{\ell^2}$ is the Euclidean vector norm. The potential function ψ characterizes *a priori* information and should be chosen such that it results in a convex regularizer R. This form of penalty function indicates that a spatial adaptive regularization energy is applied on each object property channel individually. In our preliminary studies we considered this form of the penalty because it includes the popular non-smooth total variation function as well as a variety of smooth edge-preserving penalties such as the Huber penalty. For simiplicity, we adopted the total variation function as our first penalty term to test our proposed MC methods and we referred to the MC method as PWLS-TV-MC.

To solve the MC optimization problem defined above, we developed an advanced algorithm based on the proximal point algorithm and the augmented Lagrangian method. It can be interpreted as a preconditioned version of the alternating direction method of multipliers (ADMM). [23, 62] There are numerous standard algorithms available for solving PWLS optimization problem that could be adopted for MC reconstruction. However, they generally converge slowly when the dynamic range of the weighting matrix in the data-fidelity term is large, which is precisely the case in the MC problem where the weighting matrix corresponds to the inverse covariance matrix of the MC data vector. The design of our algorithm will

circumvent the problem of slow convergence and permit accurate image reconstruction in a practical setting.

3.3.4 Methods for estimating the MC sinogram covariance

The MC reconstruction method requires knowledge of the covariance matrix Σ. When the channel sinograms are formed by use of a (weighted) least square minimization problem, which match the measured intensities for a detector pixel as a function of the phase grating step position, the framework proposed by Fessler [56] can be employed to establish an explicit expression for Σ. When the Fourier series method is employed to compute the channel sinograms, explicit expressions for the covariance can be established. The statistical properties of the raw measurement data, which are propagated through the sinogram estimation process [137, 168], will be characterized experimentally by repeated physical phantom studies. The estimated full MC sinogram covariance indicated that the absorption and dark-field channel are correlated, and the phase channel is statistically independent with the other two channels.

3.4 Results

3.4.1 Measurement data

An experimental synchrotron-based GB-XPCT data set acquired previously at the Swiss Light Source was utilized in this preliminary study. The imaged object corresponded to a rat brain. The data set contained 720 tomographic views that were evenly distributed over a 180 degree angular range. The detector pixel pitch was 7μm. At each tomographic view angle, intensity data corresponding to 4 phase-steps were recorded. We refer the readers to reference [107] for additional details regarding the data-acquisition and sample preparation. From these data, a standard Fourier decomposition method was employed to estimate the channel sinograms corresponding to the three object properties.

Because the synchrotron-based image data contained relatively low noise levels, we regard the data set as being effectively noise-free and refer this as "noise-free" data. The extracted sinograms are referred as to the "noise-free" sinograms. To emulate the high-noise condition, Gaussian noise was added to the "noise-free" measured phase-stepping intensity data. Subsequently, estimates of the channel sinograms that contained elevated noise levels were computed from these data. The produced corresponding sinograms are refrred as to the "noisy" sinograms. An empirical estimate of the covariance matrix Σ of the MC sinogram vector $\mathbf{g}$ was computed by generating an ensemble of 500 noisy phase-stepping data sets as described above and reconstructing noisy channel sinograms.

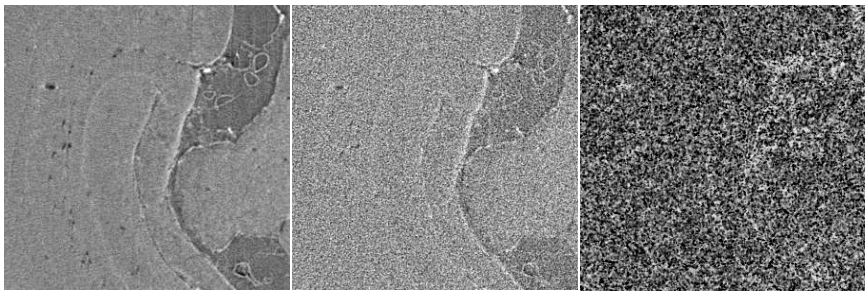

(a) (b) (c) MSSIM = 0.3673

Figure 3.2: Examples of reconstruced absorption images by FBP method for "noise-free" and "noisy" sinograms. (a) Reference image reconstructed by FBP method from noise-free projection data; (b) Noisy image reconstructed by FBP method from noisy projection data; (c) SSIM mapping for the noisy FBP image when compared to the reference image;

3.4.2 Absorption channel results

For the absorption channel, the FBP reconstructed image from the "noise-free" sinogram is treated as our reference image. One region-of-interest (ROI) was selected for visual inspection and quantitative comparison, and it is shown in Fig. 3.2 (a). The noisy ROI image reconstructed by FBP method is shown in Fig. 3.2 (b) and its corresponding SSIM mapping is shown in Fig. 3.2 (c). As can be seen, the FBP reconstructed image from "noisy" sinograms was heavily deteriorated by high-level noise. and the MSSIM value is only 0.3673.

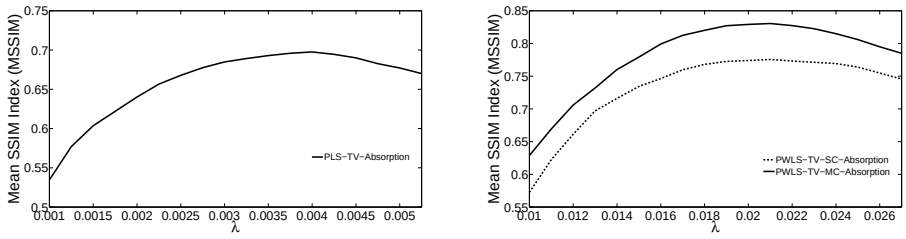

(a) (b)

Figure 3.3: Mean SSIM curves for the absorption channel: MSSIM values as a function of regularization parameters λ. The curves are parametrized by the regularization parameter. (a) Produced by PLS-TV (without noise property) case, (b) Produced by PWLS-TV-SC (dashed curve) and PWLS-TV-MC (solid curve) case.

On the other hand, three MSSIM curves as a function of regularization parameters produced by PLS-TV, PWLS-TV-SC and PWLS-TV-MC for the absorption images are shown in Fig. 3.3. The regularization parameters were selected in a proper range to control the smoothness of the images from noisy to oversmooth. As can be seen, both SC and MC cuves shown in Fig. 3.3 (b) can obtain higher MSSIM values range than the PLS-TV case without incorporating noise property. In addition, the solid MC curve is above the dashed SC cure everywhere. This indicates that the MC approach produces images that are more similar to the reference image than those produced by the SC approach.

To visually compare the reconstructed images, four reconstructed images were selected from each curve, and they are shown in Fig. 3.4. As can be seen, the PWLS-TV-MC image visually seems to have stronger ability to perserve some small structures, such as blood vessels and other edge structures, and obtain higher contrast for those structures. To quantitatively estimate those difference, the corresponding SSIM mapping for Fig. 3.4 are shown in Fig. 3.5. Based on those SSIM images, we could clearly see the SSIM images from MC approach have brighter appearance for blood vessels and others small structures, which indicate the superior similarities obtained for MC approach. These SSIM images confirm our observation about the lower noise level and higher contrast for the small structures can be obtained in PWLS-TV-MC. Meanwhile, the mean SSIM (MSSIM) values also quantitatively confirm our observation and conclusion.

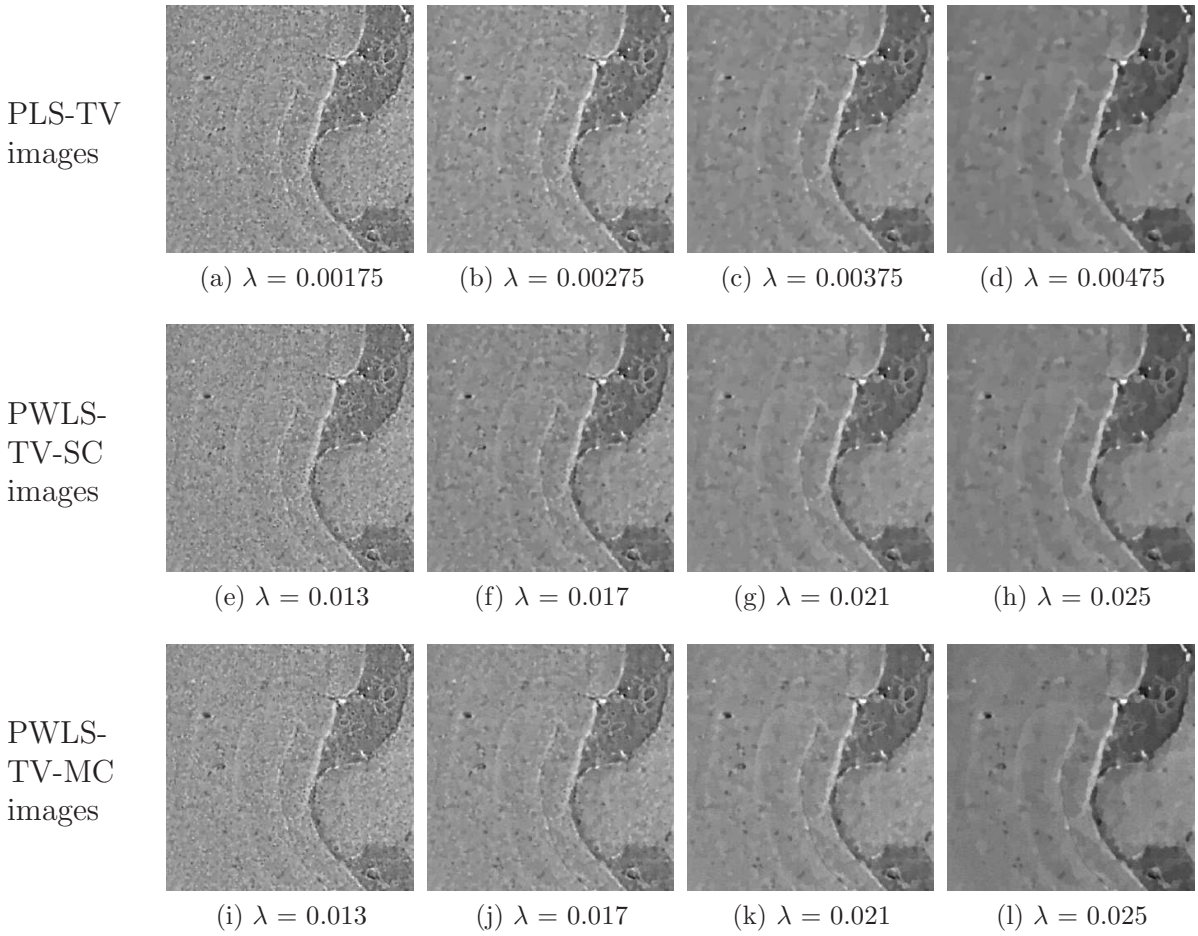

Figure 3.4: Examples of absorption images reconstructed by PLS-TV, PWLS-TV-SC and PWLS-TV-MC method with different regularization values. *First Row:* Images produced by PLS-TV method without variance; *Second Row:* Images produced by PWLS-TV-SC method; *Third Row:* Images produced by PWLS-TV-MC method. All images are displayed in the same window.

3.4.3 Darkfield channel

For the darkfield channel, the FBP reconstructed image from the "noise-free" sinogram is treated as our reference image. One region-of-interest (ROI) was selected for visual inspection and quantitative comparison, and it is shown in Fig. 3.6 (a). The noisy ROI image

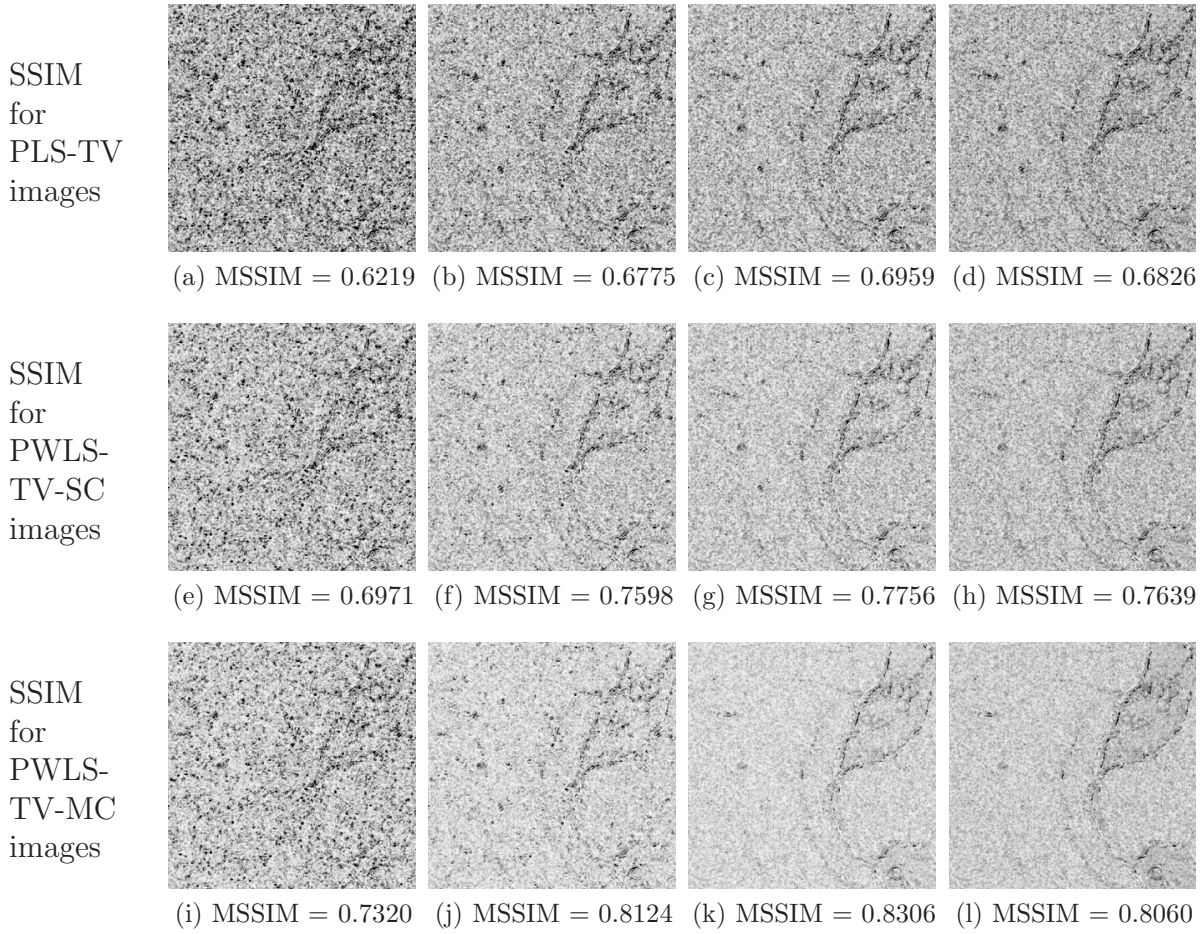

(a) MSSIM = 0.6219 (b) MSSIM = 0.6775 (c) MSSIM = 0.6959 (d) MSSIM = 0.6826

(e) MSSIM = 0.6971 (f) MSSIM = 0.7598 (g) MSSIM = 0.7756 (h) MSSIM = 0.7639

(i) MSSIM = 0.7320 (j) MSSIM = 0.8124 (k) MSSIM = 0.8306 (l) MSSIM = 0.8060

Figure 3.5: SSIM images and MSSIM values corresponding to the images in Fig.3.4. All images are dispaly in the same window [0 1].

reconstructed by FBP method is shown in Fig. 3.6 (b) and its corresponding SSIM mapping is shown in Fig. 3.6 (c). As can be seen, the FBP reconstructed image from "noisy" sinograms was heavily deteriorated by noise. and the MSSIM value was only 0.4378.

On the other hand, three MSSIM curves as a function of regularization parameters produced by PLS-TV, PWLS-TV-SC and PWLS-TV-MC for the scattering images are shown in Fig. 3.7. The regularization parameters were selected in a proper range to control the smoothness of the images from noisy to oversmooth. As can be seen, both SC and MC curves shown in Fig. 3.7 (b) obtain higher MSSIM values than the PLS-TV case without

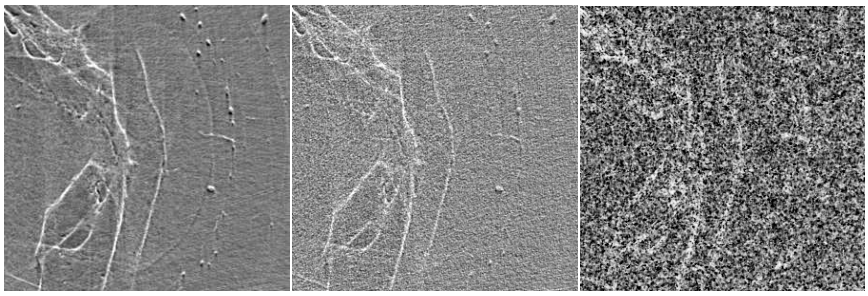

(a) (b) (c) MSSIM =0.4378

Figure 3.6: Examples of reconstruced darkfield (scattering) images by FBP method for "noise-free" and "noisy" sinograms. (a) Reference image reconstructed by the FBP method from noise-free projection data; (b) Noisy image reconstructed by FBP method from noisy projection data; (c) SSIM mapping for the noisy FBP image when compared to the reference image;

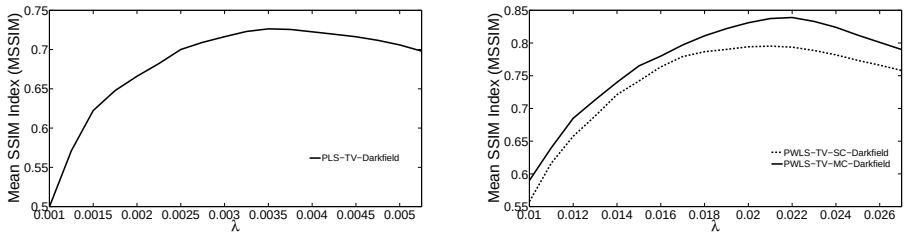

(a) (b)

Figure 3.7: Mean SSIM curves for the darkfield channel: MSSIM values as a function of regularization parameters λ. The curves are parametrized by the regularization parameter. (a) Produced by PLS-TV (without noise property) case, (b) Produced by PWLS-TV-SC (dashed curve) and PWLS-TV-MC (solid cuve) case.

incorporating noise property. In addition, the solid MC curve is above the dashed SC curve everywhere. This indicates that the MC approach produces images that are more similar to the reference image than those produced by the SC approach.

To visually compare the reconstructed images, four reconstructed darkfield images were selected from each curve, and they are shown in Fig. 3.8. As can be seen, the PWLS-TV-MC image perserves some small structures, such as blood vessels and other edge structures, and obtain higher contrast for those structures. To quantitatively estimate those difference,

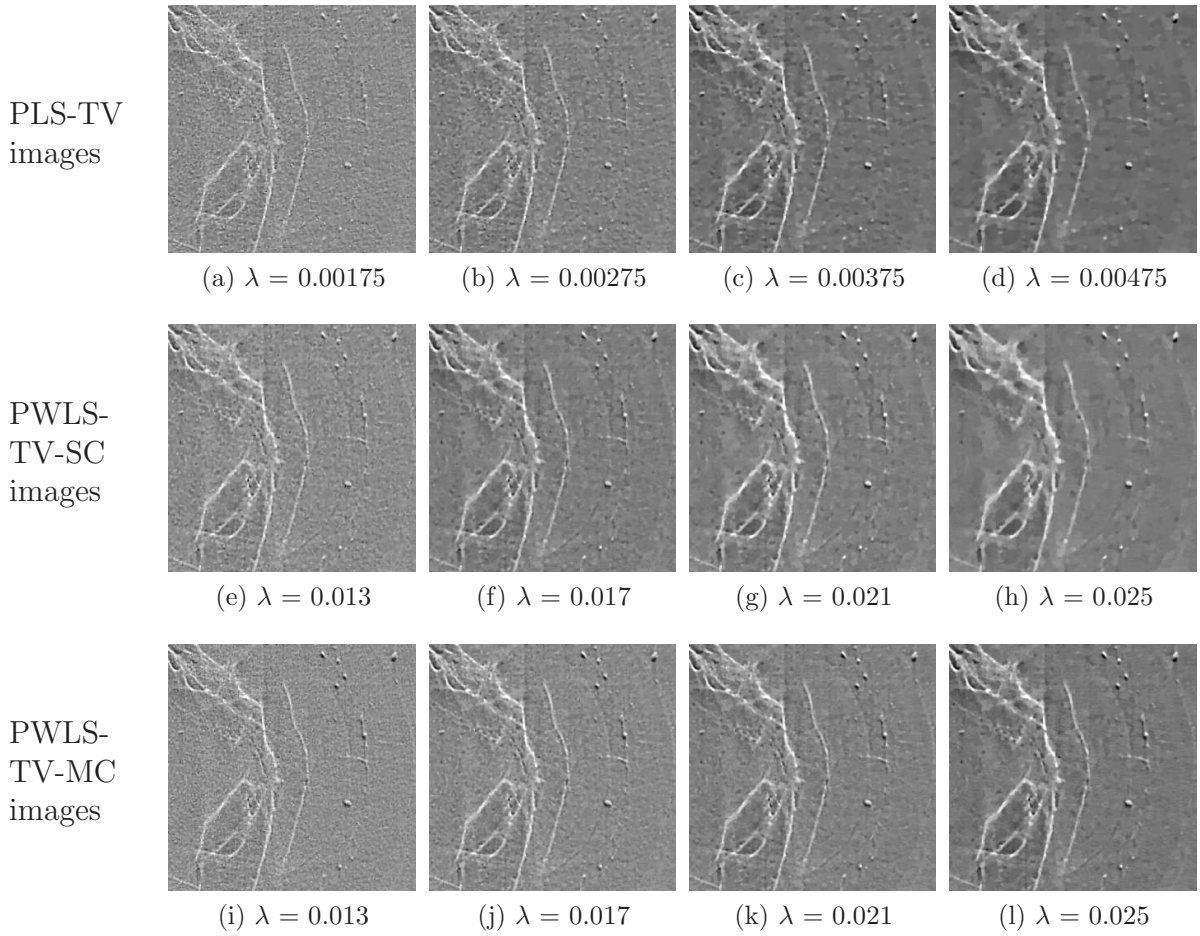

Figure 3.8: Examples of darkfield images reconstructed by PLS-TV, PWLS-TV-SC and PWLS-TV-MC method with different regularization values. *First Row:* Images produced by PLS-TV method without variance ; *Second Row:* Images produced by PWLS-TV-SC method; *Third Row:* Images produced by PWLS-TV-MC method. All images are displayed in the same window.

the corresponding SSIM mapping for Fig. 3.8 are shown in Fig. 3.9. Based on those SSIM images, we could clearly see the SSIM images from MC approach have brighter appearances for blood vessels and others small structures, which indicate the superior similarities obtained for MC approach. These SSIM images confirm our observation about the lower noise level and higher contrast for the small structures can be obtained by use of PWLS-TV-MC method. Meanwhile, the mean SSIM (MSSIM) values also quantitatively confirm our observations and conclusions.

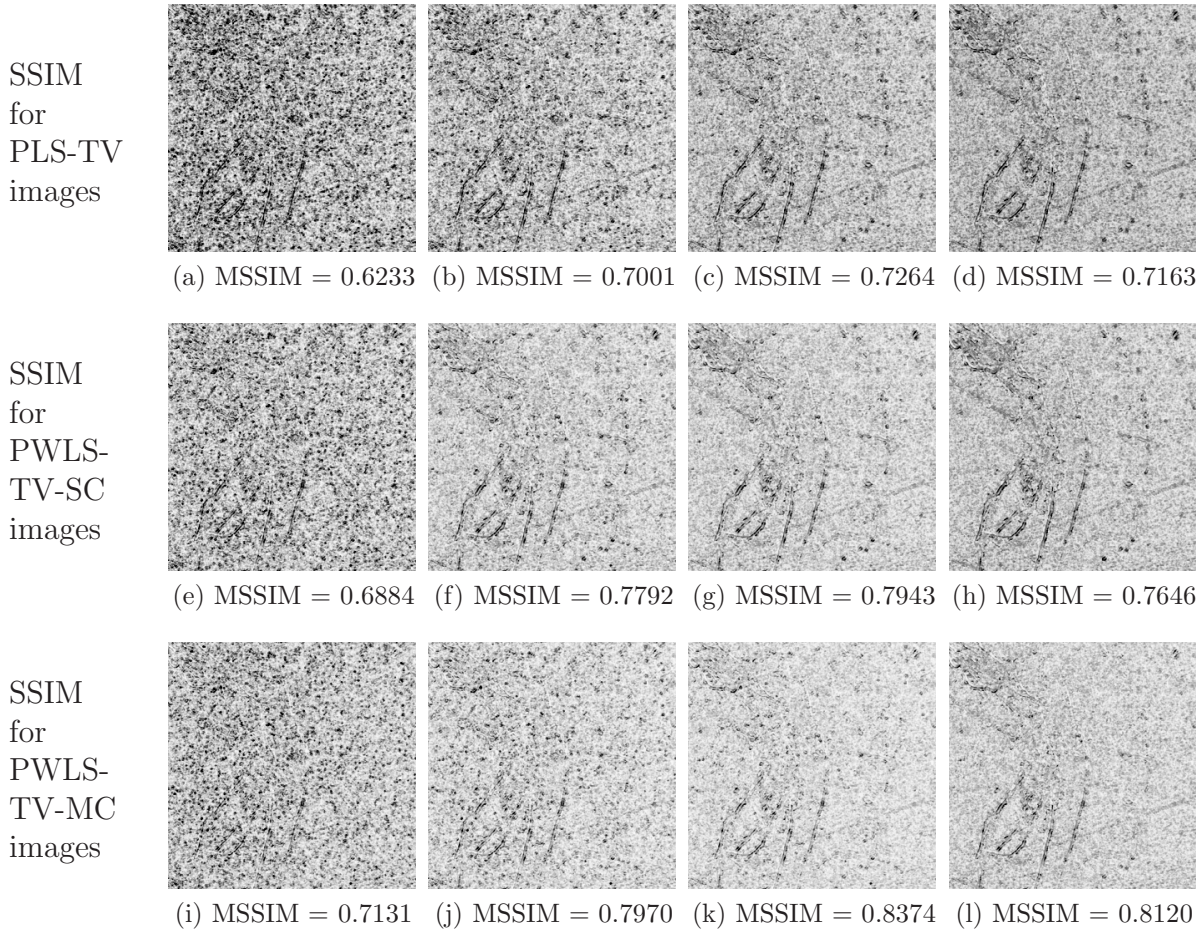

Figure 3.9: SSIM images and MSSIM values corresponding to the images in Fig.3.8. All images are displayed in a window [0 1].

3.4.4 Phase channel

Similar studies were also conducted for the phase channel. The FBP image reconstructed from the "noise-free" sinogram was treated as our reference image. One region-of-interest (ROI) was selected for visual inspection and quantitative comparison, and it is shown in Fig. 3.10 (a). The noisy ROI image reconstructed by FBP method is shown in Fig. 3.10 (b) and its corresponding SSIM mapping is shown in Fig. 3.10 (c). As can be seen, the FBP reconstructed image from "noisy" sinograms was heavily deteriorated by high-level noise. and

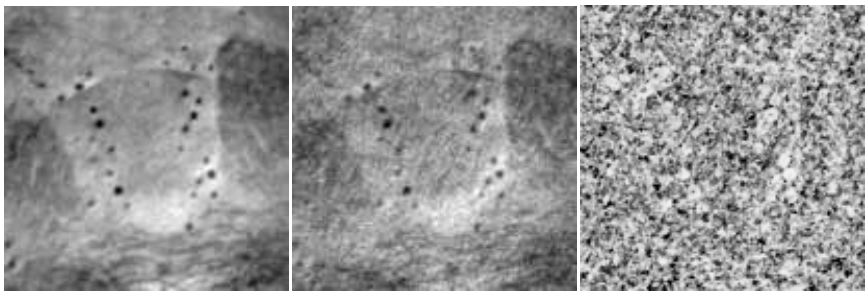

(a) (b) (c) MSSIM = 0.6133

Figure 3.10: Examples of reconstruced phase images by FBP method for "noise-free" and "noisy" sinograms. (a) Reference image reconstructed by FBP method from noise-free projection data; (b) Noisy image reconstructed by FBP method from noisy projection data; (c) SSIM mapping for the noisy FBP image when compared to the reference image;

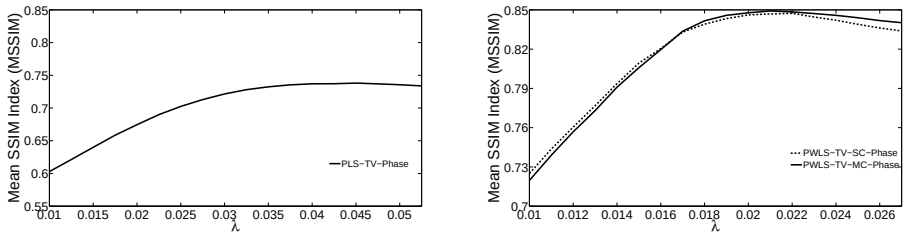

(a) (b)

Figure 3.11: Mean SSIM curves for the phase channel: MSSIM values as a function of regularization parameters λ. The curves are parametrized by the regularization parameter. (a) Produced by PLS-TV (without noise property) case, (b) Produced by PWLS-TV-SC (dashed curve) and PWLS-TV-MC (solid cuve) case.

the MSSIM value is 0.6133, which is considerable higher than the absorption and darkfield channel.

On the other hand, three MSSIM curves as a function of regularization parameters produced by PLS-TV, PWLS-TV-SC and PWLS-TV-MC for the phase images are shown in Fig. 3.11. The regularization parameters were selected in a proper range to control the smoothness of the images from noisy to oversmooth. As can be seen, As can be seen, both SC and MC cuves shown in Fig. 3.11 (b) can obtain higher MSSIM values range than the PLS-TV case without incorporating noise property. However, different to the absorption and dark-field

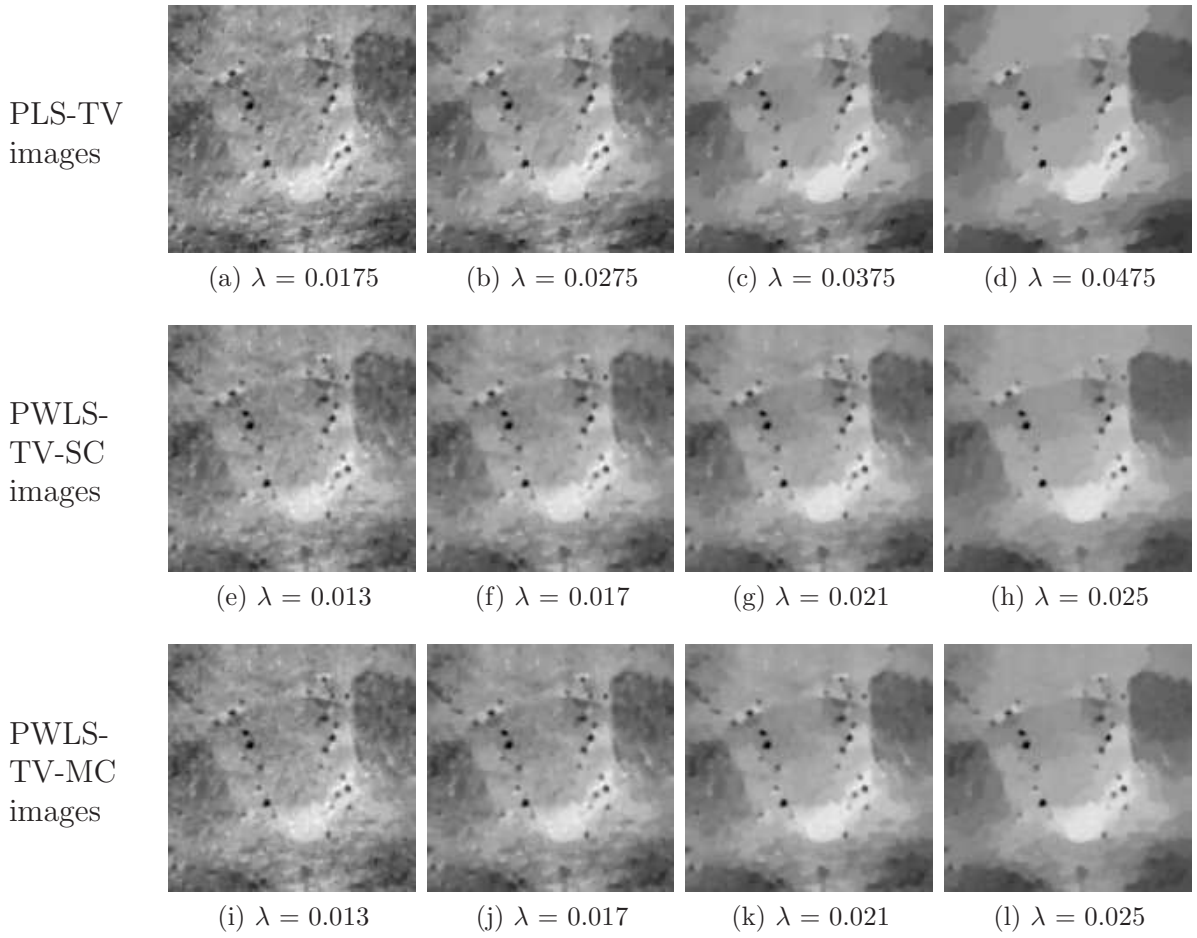

Figure 3.12: Examples of phase images reconstructed by PLS-TV, PWLS-TV-SC and PWLS-TV-MC method with different regularization values. *First Row:* Images produced by PLS-TV method without variance; *Second Row:* Images produced by PWLS-TV-SC method; *Third Row:* Images produced by PWLS-TV-MC method. All images are displayed in the same window.

channel, the two MSSIM curves from PWLS-TV-SC and PWLS-TV-MC methods are very close to each other and have very similar value ranges in this appropriate regularization coefficient range.

To visually compare the reconstructed images, four reconstructed phase images were selected from each curve, and they are shown in Fig. 3.12. As can be seen, both PWLS-TV-SC and

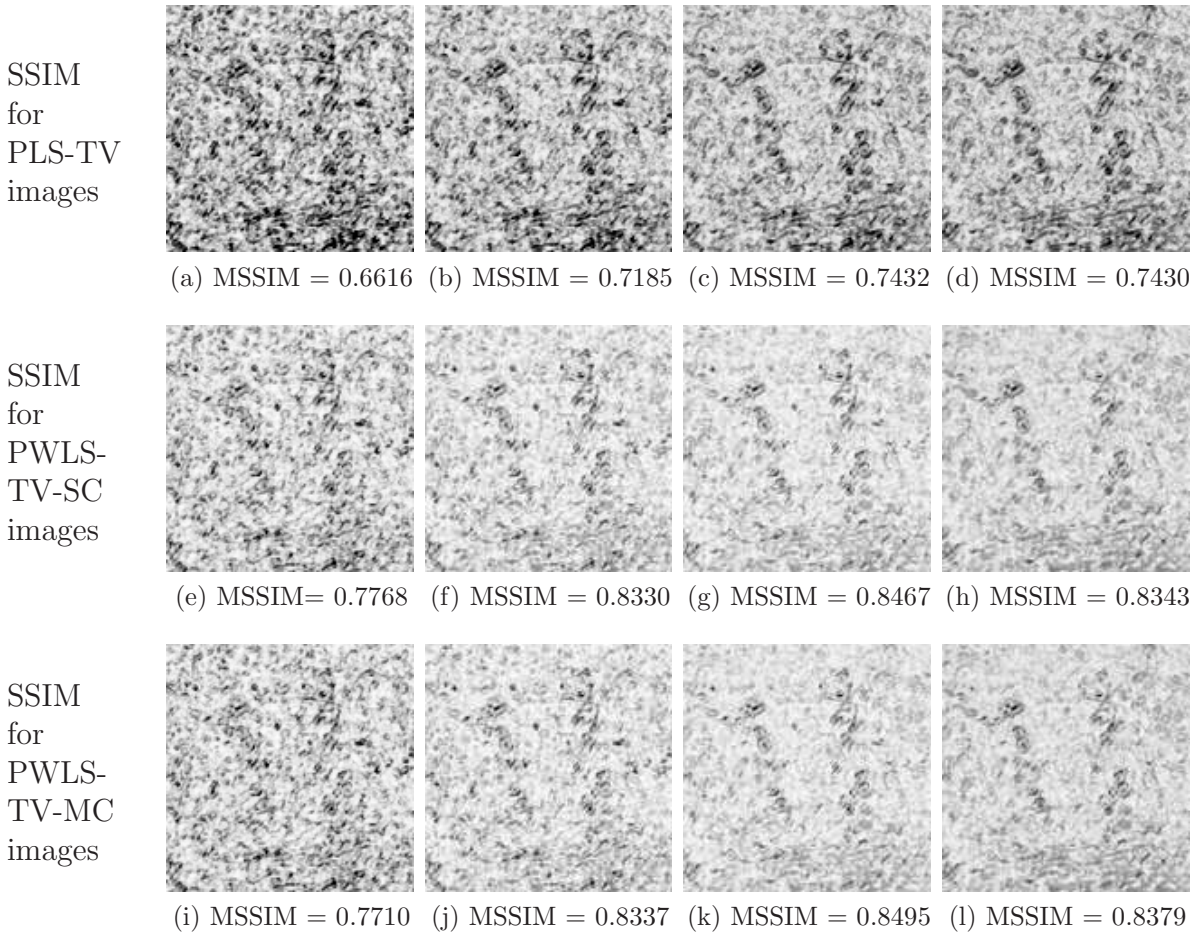

Figure 3.13: SSIM images and MSSIM values corresponding to the images in Fig.3.12. All images are displayed in a window [0 1].

PWLS-TV-MC images perserve some small structures, such as blood vessels and other edge structures and they visually look very similar for their appearance.

To quantitatively estimate those differences, the corresponding SSIM mapping for Fig. 3.12 are shown in Fig. 3.13. These SSIM images confirm our visual observation about PWLS-TV-SC and PWLS-TV-MC images. Meanwhile, the MSSIM values also quantitatively confirm our observations and conclusions.

3.5 Summary and conclusion

For the first time, we fully exploited the 2nd order statistical properties of the measurement data in GB XPCT to suppress image noise by formulating reconstruction methods in a MC framework [175]. The computer simulation studies have confirmed our expectation that the MC approach that exploits inter-sinogram correlations can achieve lower noise-levels and better image quality for the absorption and dark-field channels. This observation and conclusion can be explained by the estimated full MC covariance matrix that implies that the absorption and dark-field channels are correlated and the phase channel is statistically independent from the other two channels. These reconstruction methods will enable imaging at reduced doses and imaging times and will accelerate the translation of this imaging technology.

Chapter 4

Sparsity-Regularized Image Reconstruction of Decomposed K-Edge Data in Spectral CT

4.1 Introduction

The development of spectral X-ray computed tomography (CT) using binned photon-counting detectors has received great attention in recent years and is prompting a paradigm shift in X-ray CT imaging. These advancements are likely to benefit numerous preclinical and clinical imaging applications. For example, K-edge CT has been investigated as a modality to image contrast agents such as iodine [2, 74], gadolinium [59], bismuth [127], and gold [38]. Ytterbium was recently discussed as a contrast agent for conventional CT [98] in general and K-edge imaging [128].

The task of image reconstruction in spectral CT can be implemented in a two-stage processing scheme. In the first step, estimates of material-decomposed sinograms are obtained from the measured energy-resolved photon counts. In the second step, material images are reconstructed from knowledge of the material sinogram estimates. Statistically-principled reconstruction algorithms have been proposed [55, 144, 146, 158] that seek to minimize a penalized weighted least squares (PWLS) cost function. The weighting matrix employed in the data-fidelity term, which corresponds to the inverse covariance of the computed material sinograms, can be estimated in different ways [53, 139, 182].

While it holds great potential for important preclinical and clinical applications, selective imaging of K-edge materials in spectral CT faces challenges that currently limit its applicability. Implementations of K-edge CT employ photon counting detectors to detect the energies of individual photons. To avoid pulse-pileup in the detector, photon fluxes must be limited, which can result in long data-acquisition times. One way to mitigate long data-acquisition times is to develop image reconstruction algorithms that can produce useful images from few-view and/or noisy decomposed sinogram data. While K-edge images are often sparse, the ability of sparsity-based regularization strategies coupled with knowledge of the object-specific noise properties of the decomposed K-edge sinogram data to improve reconstructed image quality in K-edge CT remains largely unexplored.

In this Note, sparsity-regularized PWLS methods are investigated for reconstructing K-edge images from few-view decomposed sinogram data. Object-specific information regarding the decomposed K-edge sinogram variance is employed to weight the data fidelity term in the PWLS cost function. Two choices for the penalty term in the cost function are investigated: a total variation (TV) penalty and a weighted sum of a TV penalty and an ℓ_1-norm with a wavelet sparsifying transform [48, 100]. While TV and other sparsity promoting regularization strategies have been extensively applied for reconstruction problems that explictly or implicitly minimize a penalized least squares (PLS) cost function [20,63,151,174,177,179], relatively few works have investigated the impact of exploiting such regularization strategies in combination with a statistically weighted data fidelity term in a PWLS framework [101, 135]. Computer-simulation and experimental phantom studies are conducted to visually and quantitatively demonstrate the efficacy of the proposed reconstruction methods.

4.2 Materials and Methods

4.2.1 PWLS Image Reconstruction with TV and ℓ_1-norm Regularization

In spectral CT imaging equipped with photon-counting detectors, a set of N_b energy resolved photon count measurements are obtained and employed to estimate a collection of $N_m \leq N_b$ sinograms that represent pre-determined material properties. This process is referred

to as material sinogram decomposition. Let A_n denote a lexicographically ordered vector representing the decomposed sinogram corresponding to the n-the material, and let $\mathbf{A} = [A_1; \ldots; A_{N_m}]$ denote the vector formed by stacking all of the A_n. Maximum likelihood (ML) estimates of $\mathbf{A}$, denoted by $\hat{\mathbf{A}}$, can be obtained assuming a Poisson noise model [141]. Given the ML-estimator, the diagonal elements of the Fisher information matrix can be numerically computed [39, 140] and used to estimate the variance of the decomposed sinograms.

We consider the problem of reconstructing an estimate of the n-th object material individually, which is assumed to be a K-edge material. Let $\mathbf{f}_n$ denote a N-dimensional approximation of the sought-after K-edge material distribution. In this work, conventional pixels were utilized to form $\mathbf{f}_n$. The M-dimensional vector $\hat{\mathbf{A}}_n$ representing the decomposed K-edge sinogram estimate is related to $\mathbf{f}_n$ by the approximate imaging model $\hat{\mathbf{A}}_n = \mathbf{H}\mathbf{f}_n$, where the $M \times N$ matrix $\mathbf{H}$ represents a discrete 2D fan-beam forward projector in the two-dimensional studies described below.

The following PWLS estimators of $\mathbf{f}_n$ were considered [176]:

$$\hat{\mathbf{f}}_n \;=\; \arg\min_{\mathbf{f}_n \geq 0} \left\| \hat{\mathbf{A}}_n - \mathbf{H}\mathbf{f}_n \right\|^2_{\mathbf{W}_n} \;+\; 2\lambda_{tv} \|\mathbf{f}_n\|_{tv} \;, \tag{4.1}$$

and

$$\hat{\mathbf{f}}_n \;=\; \arg\min_{\mathbf{f}_n \geq 0} \left\| \hat{\mathbf{A}}_n - \mathbf{H}\mathbf{f}_n \right\|^2_{\mathbf{W}_n} \;+\; 2\lambda_{tv} \|\mathbf{f}_n\|_{tv} + \; 2\lambda_{l1} \|\mathbf{\Phi}\mathbf{f}_n\|_1 \;, \tag{4.2}$$

where λ_{tv} and λ_{l1} are positive regularization parameters, $\|\cdot\|_{tv}$ and $\|\cdot\|_1$ denote the TV and ℓ_1-norms, and $\mathbf{\Phi}$ is a wavelet transform operator. In this work, $\mathbf{\Phi}$ was chosen as the Daubechies discrete wavelet transform involving three wavelet scales. The $M \times M$ diagonal weight matrix $\mathbf{W}_n$ contains elements that are specified by the inverse of the variance of each sinogram element that, in this work, are estimated by use of the Fisher information matrix as described previously [139]. Since the second order statistics of the decomposed sinograms can be accurately described by Gaussian statistics [145], the above PWLS estimators can be considered as accurate approximations of penalized maximum likelihood estimators. Our method for solving Eq. (4.1) will be referred to as the PWLS-TV method. In the case when the sinogram variance information is ignored and $\mathbf{W}_n$ is redefined as the $M \times M$ identity matrix, the implementation of Eq. (4.1) will be referred to as the PLS-TV method. Similarly, our method for solving Eq. (4.2) will be referred to as the PWLS-TV-ℓ_1 method. The

PWLS-TV and PLS-TV methods were implemented by use of the fast iterative shrinkage-thresholding algorithm (FISTA) [14]. The PWLS-TV-ℓ_1 method was implemented by use of the combination of the splitting algorithm proposed by Combettes [37] and the FISTA. A similar strategy has also been proposed by two previous works [77, 102] for MR image reconstruction, in which the variance $\mathbf{W}_n$ was an identify matrix.

It should be noted that combining the TV and ℓ_1-norm penalties [30] in Eq. (4.2) is motivated by the fact that use of a PLS-TV estimator can result in patch-like image distortions if the chosen value of the regularization parameter λ_{tv} is too large. Combining the penalties yields the opportunity to exploit the effective denoising properties of TV regularization while mitigating these distortions. A previous work [63] employed a similar approach for a 'fully-spectral' CT problem in which the sinogram decomposition step was avoided. That work differs from our study in several ways. For example, it was based on a linearized imaging model that assumed monochromatic illumination, it did not investigate the incorporation of the second-order statistical properties of the measurement data into the reconstruction method, and did not exploit object sparsity in the wavelet transform domain.

4.2.2 Computer-Simulation Studies

Computer-simulation studies were conducted to investigate: (1) the advantages of the PWLS-TV method over the PLS-TV method for reduced-view K-edge image reconstruction; and (2) the advantages of the PWLS-TV-ℓ_1 method over the PWLS-TV method for the same task. A numerical phantom was created from a representative conventional CT image dataset that had been originally acquired with a clinical system (Brilliance iCT, Philips Healthcare, Eindhoven, The Netherlands). The clinical CT image was segmented into 'soft tissue' and 'bone' components. In addition, objects containing ytterbium were inserted as shown in Fig. 4.1 (left). A zoomed-in region containing the ytterbium inserts is provided in Fig. 4.1 (right). The cylinder indicated by the arrow in the upper-left region was intended to mimic a fibrin-targeted contrast agent in a coronary artery. All material attenuation coefficients were determined from the Photon Cross Sections Database [17].

From this numerical phantom, material-specific line integral data and variance estimates [139] were computed for the material basis set 'photo-electric absorption', 'Compton effect', and

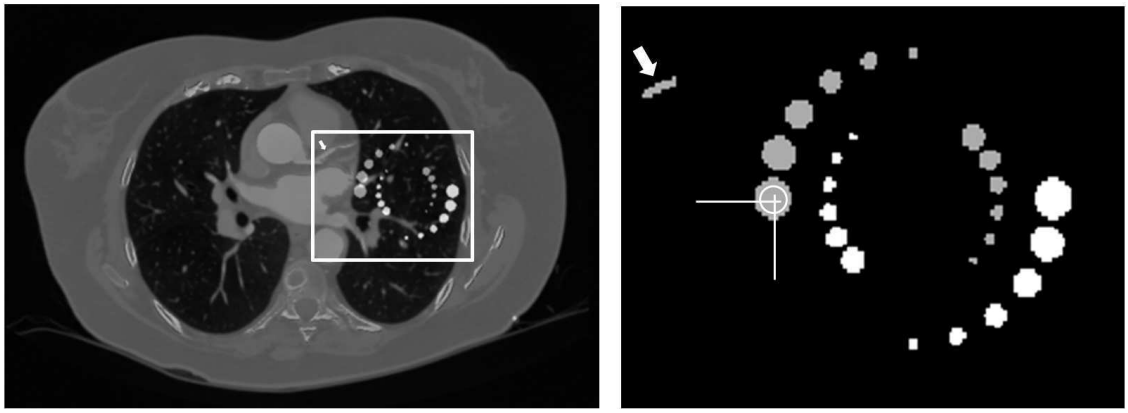

Figure 4.1: The numerical phantom employed in the computer-simulation studies is shown in the left panel and is described in the text. The right panel displays a zoomed-in image of the ytterbium inserts contained within the white box in the left panel.

'ytterbium', assuming a 2D equal-angle fan-beam geometry. The source-to-rotation center distance was 0.57 m and the distance between the source and the center of the detector was 1.04 m. The fan-angle was approximately 52 degrees and the number of detector units was 1024. An x-ray source spectrum and detector response function for a binned photon-counting detector was employed as described in a previous study [147]. The energy thresholds of the six energy bins were set at 25, 46, 61, 64, 76 and 91 keV, respectively. These energy bins were determined in our previous sensitivity of photon-counting based K-edge imaging study [142]. The following scan protocol parameters were assumed: anode voltage 130 kVp, anode current 400 mA, 1200 views/turn, 0.27s/turn.

By use of the estimated variance matrix and treating the noiseless ytterbium sinogram estimate as the mean of a Gaussian random vector, an ensemble of $M = 500$ noisy K-edge sinograms was computed. The PWLS-TV and PLS-TV methods were employed to reconstruct 500 images from the ensemble of noisy K-edge sinograms. Images were reconstructed by use of the two reconstruction methods from reduced-view K-edge sinograms that contained 400, 200, and 100 equally spaced tomographic view angles over 360°. Different choices of the regularization parameter values were considered as described below. In all cases, the reconstructed images were of dimension 1024 x 1024 with a pixel size 0.5 x 0.5 mm^2. The stopping criteria adopted in all studies was chosen such that a converged result was ensured. Specifically, iterations were terminated when changes in the objective function occurred only in the sixth decimal place.

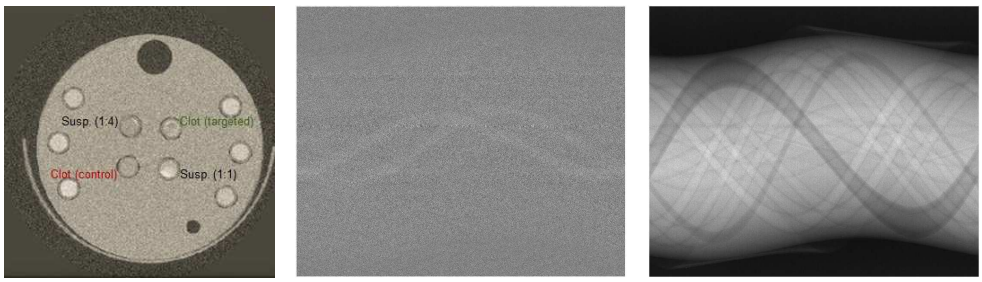

(a) Conventional CT (FBP) (b) K-edge sinogram (1024 x 1250) (c) K-edge variance estimates

Figure 4.2: Physical Phantom Experiment: (a) Conventional CT reconstruction of the physical phantom using a standard filtered backprojection (FBP) algorithm. (b) Decomposed K-edge (ytterbium) sinogram. (c) The estimated sinogram variance.

4.2.3 Assessment of spatial resolution and noise properties

From the ensemble of noisy images reconstructed by use of the PLS-TV and PWLS-TV methods, the average empirical image variance within the region-of-interest (ROI) indicated by the white circle in the right image shown in Fig. 4.1 was computed. To quantify the anisotropic spatial resolution, a cumulative Gaussian function [94] was fit to two orthogonal profiles in the mean image, respectively, whose locations are indicated in the right panel of Fig. 4.1. The full-width at half-maximum (FWHM) value of the fitted error function served as a summary measure of spatial resolution at that location in image space, with smaller values indicating higher spatial resolution.

The values of the regularization parameters employed in this study were chosen in a way that the appearance of reconstructed images varied subjectively from under-smoothed (high-level noise) to relatively over-smoothed (low-noise level). The effects of incorporating sinogram variance information can be easily identified in such a comparision, since the PLS-TV and PWLS-TV method have the same TV regularization term and the only difference between the two methods is whether the sinogram variances was incorporated or not. The PWLS-TV-$\ell 1$ method was not examined in this component of our study due to the added complication of having to systematically vary two regularization parameters.

4.2.4 Quantitative measurement of different reconstruction algorithms performance

The structural similarity index measurement (SSIM) [167] was adopted to quantify the similarity between images reconstructed by use of the different methods and the original phantom object. The absolute value of each element in an image of SSIM values is between 0 and 1, in which the value of 1 is obtained only if the pixel values of the images being compared are identical. A mean SSIM (MSSIM) value was computed by averaging the SSIM image.

4.2.5 Phantom Experiment with Targeted Ytterbium-Nanoparticles

To corroborate the computer-simulation results, experimental data were acquired with a spectral CT small animal scanner prototype (Philips Research, Hamburg, Germany). Figure 4.2(a) shows a representative slice of a conventional CT reconstruction of the phantom (PMMA, diameter 50 mm). It was composed of calcium chloride probes (3 mol/l), mimicking the rib cage, and in its center four X-ray lucent tubes, two tubes filled with suspension of ytterbium nanocolloids [128] diluted with water in the ratio 1:1 and 1:4, respectively, and two probes containing human fibrin-rich clots. One of the clots was targeted with YbNC equipped with a fibrin-specific antibody designed to bind to ruptured plaque [127] while the other did not contain any YbNC. The following scan parameters were used: anode voltage 130 kVp, anode current 50 mA, planar detector geometry, 1250 views/turn, rotation time/turn 100 s, energy thresholds identical to the settings of the simulation. A ML estimate of the decomposed K-edge sinogram corresponding to 'ytterbium' was computed along with an estimate of the sinogram variance. The estimated K-edge sinogram and sinogram variance are displayed in Fig. 4.2(b) and 4.2(c), respectively. Note that a high noise level in the decomposed sinogram can be observed. Images were reconstructed by use of the different reconstruction methods on a 256×256 matrix with a pixel size of 0.24×0.24 mm^2.

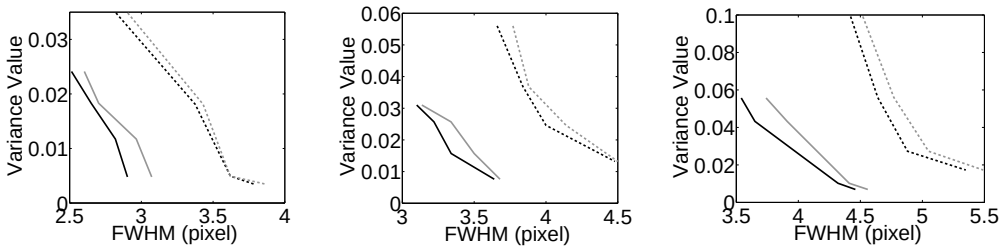

(a) 400 view datasets (b) 200 view datasets (c) 100 view datasets

Figure 4.3: Computer-simulation studies: Ensemble variances as a function of spatial resolution (FWHM) for different undersampling factors. The curves are parametrized by the regularization parameter. FWHM values are evaluated in horizontal (black) and vertical (gray) orientation at positions shown in Fig. 4.1. The PWLS-TV results (solid) show an improved noise-resolution performance compared to PLS-TV (dashed).

4.3 Computer-Simulation Studies

4.3.1 Spatial resolution and noise properties

The plots of image variance vs. spatial resolution that were created by sweeping the regularization parameter and are displayed in Fig. 4.3 for cases in which 400, 200, or 100 tomographic views were employed for image reconstruction. In all cases, the PWLS-TV method (solid curves) shows a superior tradeoff between variance and resolution compared to the PLS-TV method (dashed curves). This confirms the expected finding that it is advantageous to employ knowledge of the decomposed sinogram variance in the reconstruction method. This is found to be especially important for mitigating deteroriation of the variance and resolution properties when reduced-view tomographic data are employed, as demonstrated by the significantly improved performance of the PWLS-TV over the PLS-TV method for the 100- and 200- view cases.

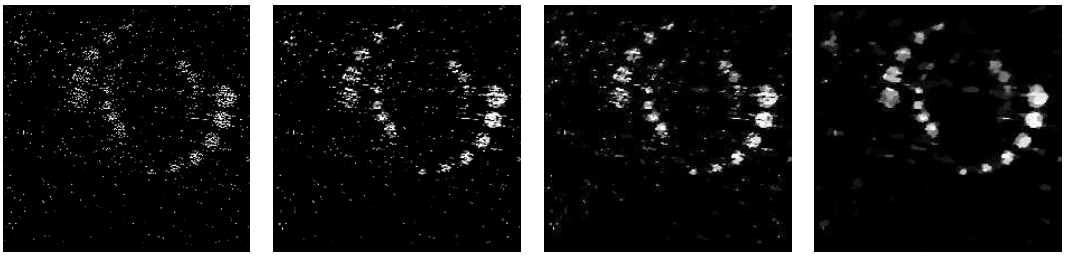

(a) PLS-TV, $\lambda_{tv} = 0$ (b) PLS-TV $\lambda_{tv} = 1 \cdot 10^{-4}$ (c) PLS-TV $\lambda_{tv} = 2 \cdot 10^{-4}$ (d) PLS-TV, $\lambda_{tv} = 4 \cdot 10^{-4}$

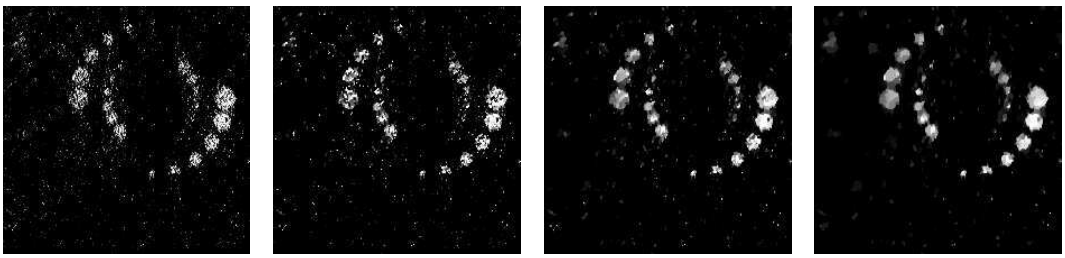

(e) PWLS-TV, $\lambda_{tv} = 0.0$ (f) PWLS-TV, $\lambda_{tv} = 0.1$ (g) PWLS-TV, $\lambda_{tv} = 0.2$ (h) PWLS-TV, $\lambda_{tv} = 0.3$

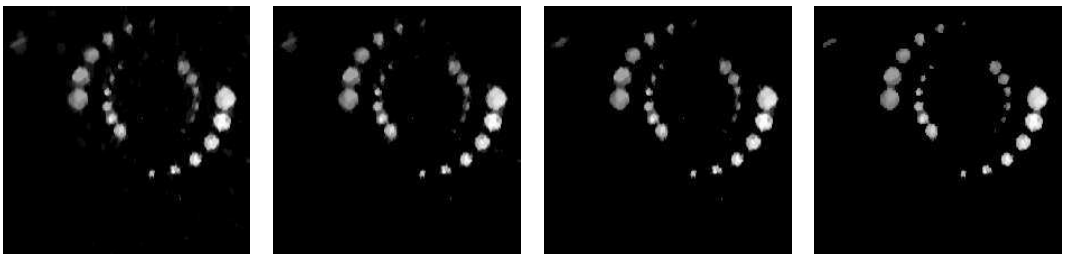

(i) PWLS-TV-ℓ_1, $\lambda_{tv} = 0.3, \lambda_{l1} = 0.2$ (j) PWLS-TV-ℓ_1, $\lambda_{tv} = 0.3, \lambda_{l1} = 0.5$ (k) PWLS-TV-ℓ_1, $\lambda_{tv} = 0.3, \lambda_{l1} = 0.8$ (l) PWLS-TV-ℓ_1, $\lambda_{tv} = 0.3, \lambda_{l1} = 1.0$

Figure 4.4: Computer-simulation studies: Examples of reconstructed K-edge images ROIs for the 200-view case corresponding to different regularization parameter values. All images are cropped to size of 300×300 pixels and are displayed in the same grey-scale window. Images reconstructed via PLS-TV (a-d), PWLS-TV (e-h) and PWLS-TV-ℓ_1 (i-h).

4.3.2 Qualitatively assesments

To visually examine the effects of incorporating the decomposed sinogram variance in the reconstruction method, examples of images reconstructed by use of the PLS-TV and PWLS-TV methods for the 200-view case are shown in Figure 4.4(a)-(d), (e)-(h). In the first and second rows, from left-to-right, the TV regularization parameter λ_{tv} was increased from

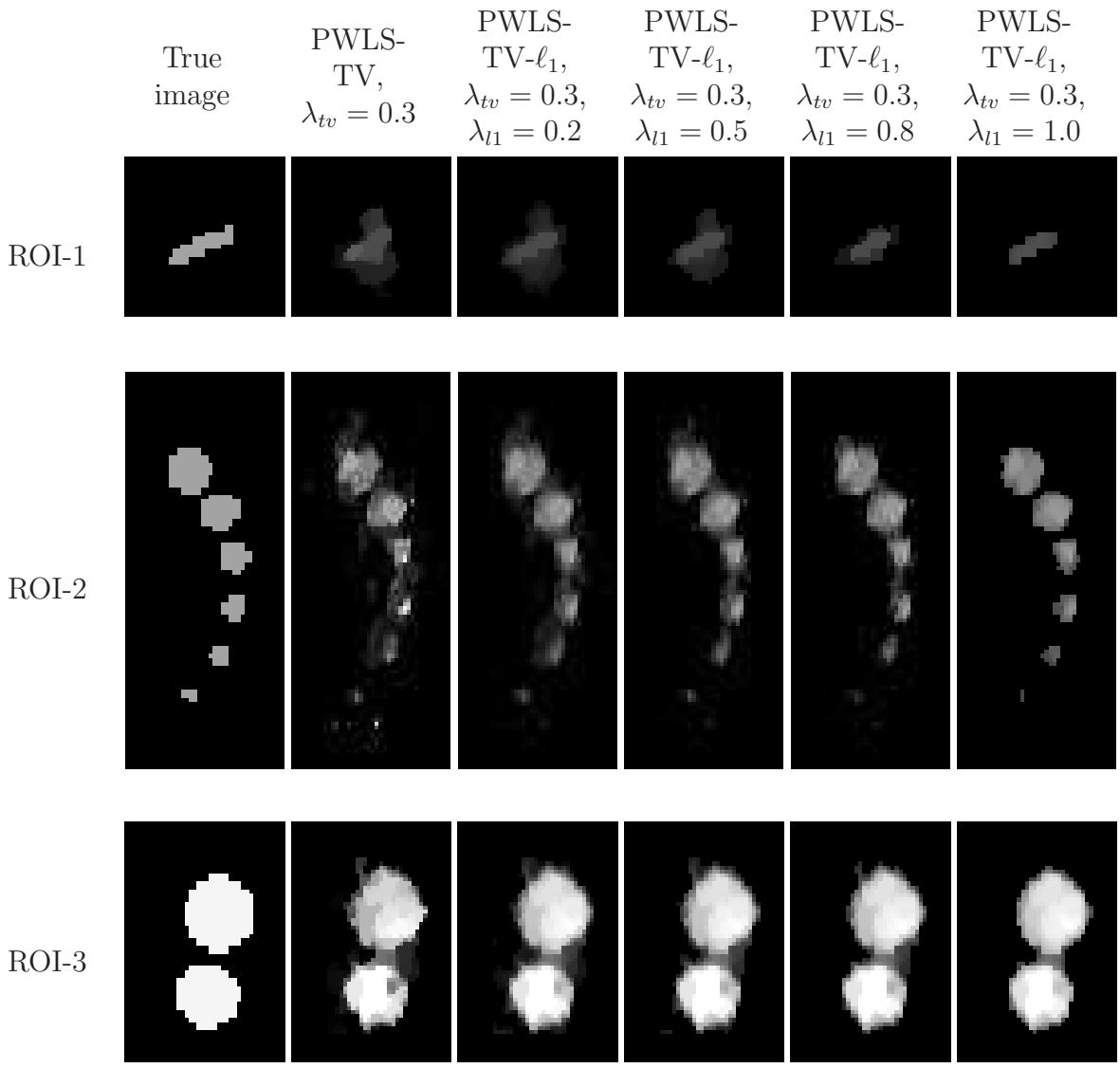

Figure 4.5: Three zoomed-in ROIs of true phantom and corresponding reconstructed images from Fig. 4.4. Each column was obtained from the oringial phantom or one particular reconstructed image, which is indicated by the name shown in first row. All images were displayed in the same grey-scale window.

zero to some positive value. When no TV penalty was added ($\lambda_{tv} = 0$), the impact of incorporating the sinogram variance can be observed readily. In particular, the PWLS estimate in Fig. 4.4(e) contains structures whose shapes are better preserved than those in

the PLS estimate in Fig. 4.4(a). For the case when TV regularization was employed, the PLS-TV estimates in Figs. 4.4(c) and (d) contained lower noise levels but some of the small object structures were lost. On the other hand, the structures in Fig. 4.4(h) reconstructed by the PWLS-TV method are perserved with better appearance with less shape distortion, especially for small structures.

Note that the images in Figs. 4.4(g) and (h) reconstructed by use of the PWLS-TV method contain a noise contribution that is comprised of isolated pixels having large values. This noise can be effectively suppressed by use of the PWLS-TV-ℓ_1 reconstruction method. Figures 4.4(i)-(l) display the images reconstructed by use of the PWLS-TV-ℓ_1 method, where the value of λ_{tv} was fixed and the value of λ_{l1} was increased from left to right. To more clearly see the effects of including the ℓ_1 regularization term, zoomed-in ROIs of Fig. 4.4(h) and Figs. 4.4(i)-(l). are shown in Fig. 4.5. The first column of images shows the ROIs from the true phantom. The second column shows ROIs from the image in Fig. 4.4(h) that reconstructed by use of the PWLS-TV method. The remaining columns show ROIs from the images in Figs. 4.4(i)-(l) that reconstructed by use of the PWLS-TV-ℓ_1 method. As the value of λ_{l1} is increased, the ROI-I images become more sharp and compact due to the ℓ_1 sparsity constraint. The ROI-2 and ROI-3 images also display the same tendency.

4.3.3 SSIM comparison between PWLS-TV and PWLS-TV-ℓ1

In order to quantitatively measure the difference between reconstructed PWLS-TV and PWLS-TV-ℓ_1 images, the SSIM images and MSSIM values corresponding to the images in Fig. 4.4 (e-l) are displayed in Fig. 4.6. The MSSIM values corresponding to the PWLS-TV-ℓ_1 method are higher than those corresponding to the PWLS-TV method. Moreover, the backgrounds of the SSIM images are much more uniform and have a majority of pixel values close to one; this reflects the fact that the PWLS-TV-ℓ_1 method was able to remove the isolated noisy pixels that were produced by the PWLS-TV method These quantitative results are consistent with the qualitative observations described above.

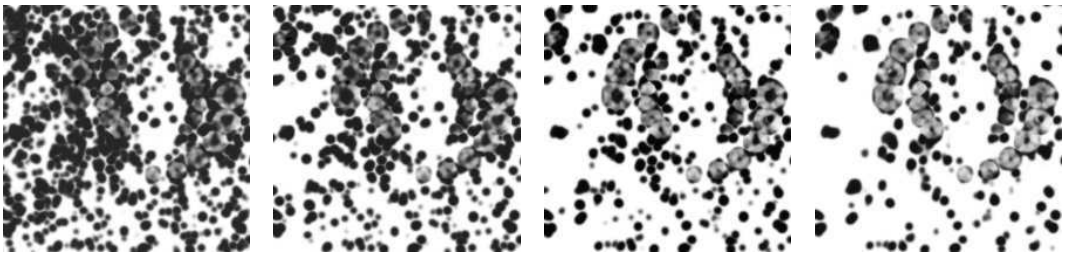

(a) PWLS-TV, $\lambda_{tv} = 0$, MSSIM=0.491 (b) PWLS-TV, $\lambda_{tv} = 0.1$, MSSIM=0.603 (c) PWLS-TV, $\lambda_{tv} = 0.2$, MSSIM=0.703 (d) PWLS-TV, $\lambda_{tv} = 0.3$, MSSIM=0.776

(e) PWLS-TV-ℓ1, $\lambda_{tv} = 0.3, \lambda_{l1} = 0.2$, MSSIM=0.904 (f) PWLS-TV-ℓ1, $\lambda_{tv} = 0.3, \lambda_{l1} = 0.5$, MSSIM=0.917 (g) PWLS-TV-ℓ1, $\lambda_{tv} = 0.3, \lambda_{l1} = 0.8$, MSSIM=0.930 (h) PWLS-TV-ℓ1, $\lambda_{tv} = 0.3, \lambda_{l1} = 1.0$, MSSIM=0.952

Figure 4.6: SSIM images and MSSIM values corresponding to the images in Fig.4.4 (e)-(h) reconstructed by use of the PWLS-TV method are shown in subfigures (a)-(d), respectively. SSIM images and MSSIM values corresponding to the images in Fig.4.4 (i)-(l) reconstructed by use of the PWLS-TV-ℓ_1 method are shown in subfigures (e)-(h), respectively. All images are displayed in the same window [0 1].

4.3.4 Different number of views results for FBP and proposed PWLS-TV-ℓ1

The performance of the PWLS-TV-ℓ1 method was compared to that of the filtered back-projection (FBP) algorithm. Images reconstructed by use of the FBP algorithm by use of 100, 200, 400 and 1200 views (full-view) are shown in Fig. 4.7(a)-(d). Images reconstructed by use of the PWLS-TV-ℓ1 method, corresponding to different regularization parameters, from 100, 200 and 400 views are shown in Figs. 4.7(e)-(h), (i)-(l) and Figs. 4.7(m)-(p). As expected, the images reconstructed by use of the FBP algorithm contain significantly elevanted noise levels. The structures in the 100-view FBP image are difficult to identify due to the high noise levels in the image. Conversely, the performance of the PWLS-TV-ℓ1 method degraded much more slowly than the FBP algorithm as the number of tomographic views

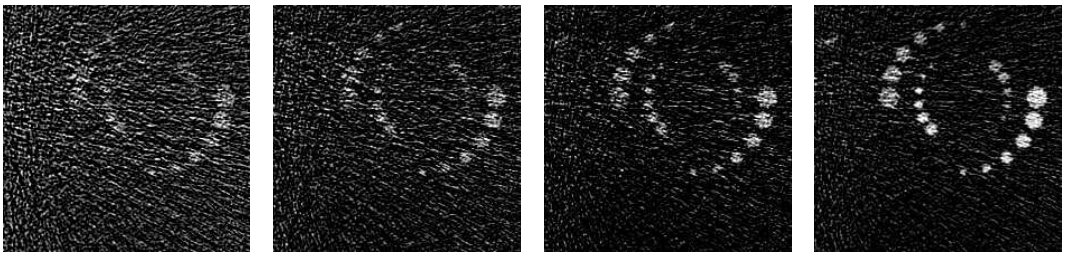

(a) FBP, 100views (b) FBP, 200views (c) FBP, 400views (d) FBP, 1200views

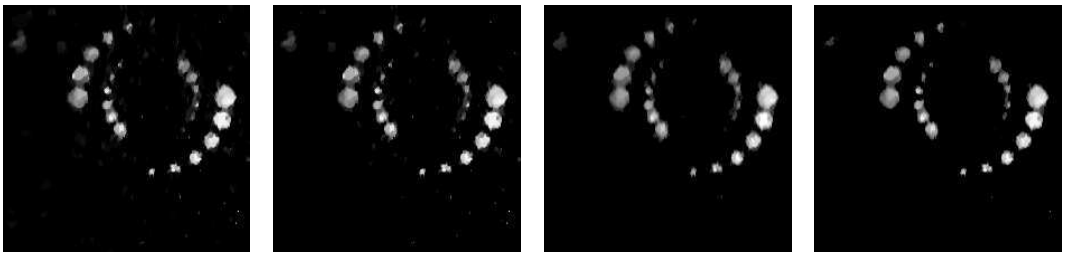

(e) PWLS-TV-ℓ_1,100, $\lambda_{tv} = 0.2, \lambda_{l1} = 0.2$ (f) PWLS-TV-ℓ_1,100, $\lambda_{tv} = 0.2, \lambda_{l1} = 0.5$ (g) PWLS-TV-ℓ_1,100, $\lambda_{tv} = 0.2, \lambda_{l1} = 0.8$ (h) PWLS-TV-ℓ_1,100, $\lambda_{tv} = 0.2, \lambda_{l1} = 1.0$

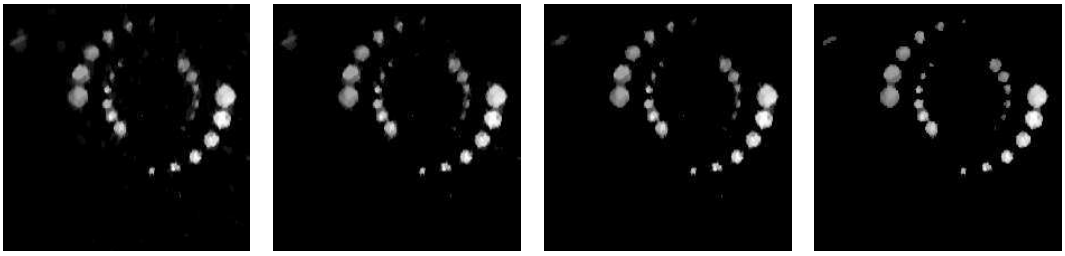

(i) PWLS-TV-ℓ_1,200, $\lambda_{tv} = 0.3, \lambda_{l1} = 0.2$ (j) PWLS-TV-ℓ_1,200, $\lambda_{tv} = 0.3, \lambda_{l1} = 0.5$ (k) PWLS-TV-ℓ_1,200, $\lambda_{tv} = 0.3, \lambda_{l1} = 0.8$ (l) PWLS-TV-ℓ_1,200, $\lambda_{tv} = 0.3, \lambda_{l1} = 1.0$

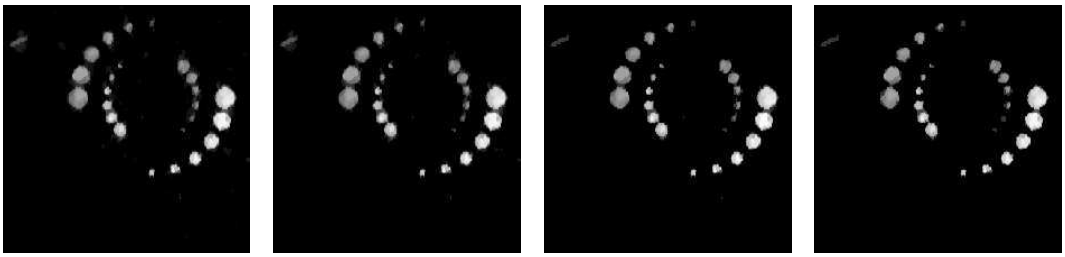

(m) PWLS-TV-ℓ_1,400, $\lambda_{tv} = 0.4, \lambda_{l1} = 0.2$ (n) PWLS-TV-ℓ_1,400, $\lambda_{tv} = 0.4, \lambda_{l1} = 0.5$ (o) PWLS-TV-ℓ_1,400, $\lambda_{tv} = 0.4, \lambda_{l1} = 0.8$ (p) PWLS-TV-ℓ_1,400, $\lambda_{tv} = 0.4, \lambda_{l1} = 1.0$

Figure 4.7: Examples of reconstructed K-edge images via FBP algorithm (a-d) and PWLS-TV-ℓ1 algorithm by use of 100 views (e-h), 200 views (i-l) and 400 views (m-p). All images are displayed in the same window.

was reduced. Even in the few-view cases, the PWLS-TV-ℓ1 method produced images that possess relatively clean backgrounds.

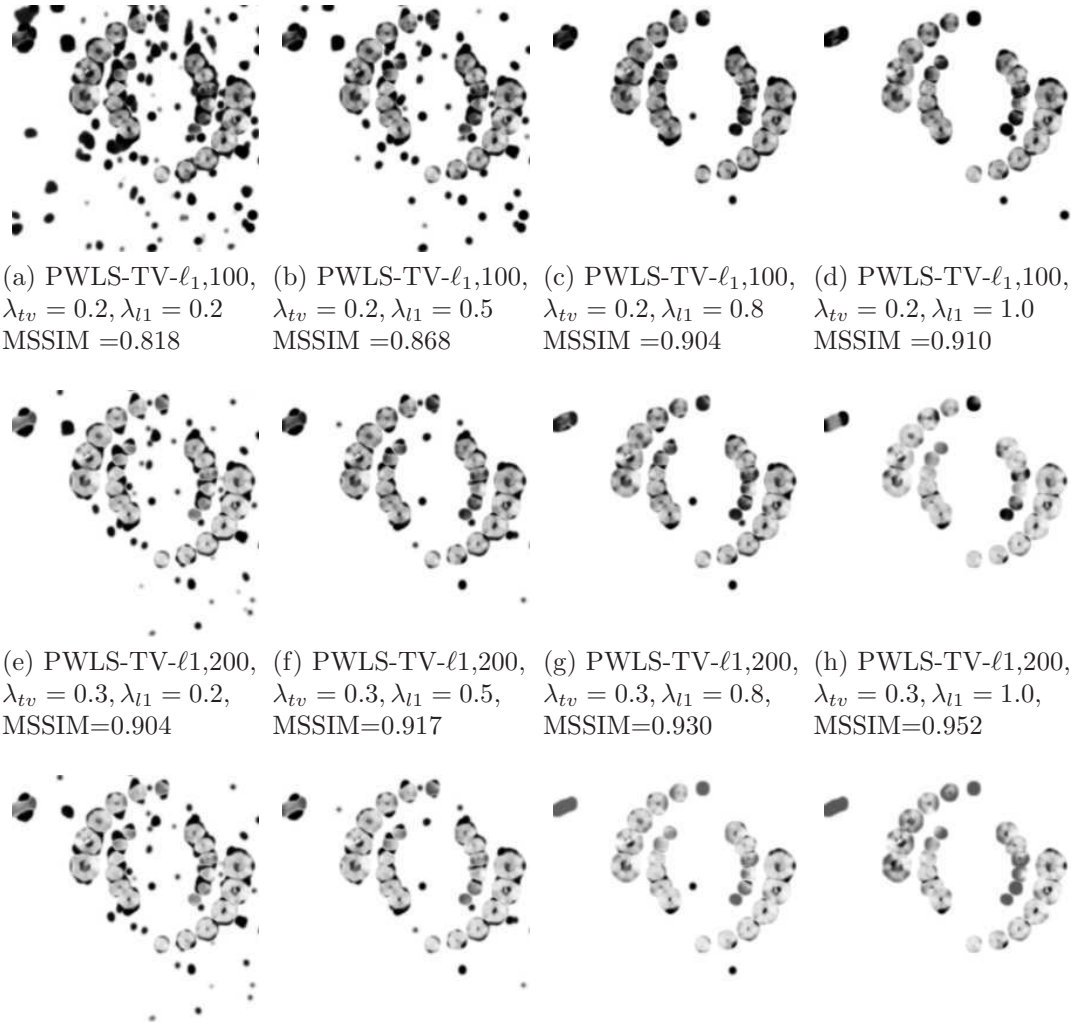

(a) PWLS-TV-ℓ_1,100, $\lambda_{tv} = 0.2, \lambda_{l1} = 0.2$ MSSIM =0.818

(b) PWLS-TV-ℓ_1,100, $\lambda_{tv} = 0.2, \lambda_{l1} = 0.5$ MSSIM =0.868

(c) PWLS-TV-ℓ_1,100, $\lambda_{tv} = 0.2, \lambda_{l1} = 0.8$ MSSIM =0.904

(d) PWLS-TV-ℓ_1,100, $\lambda_{tv} = 0.2, \lambda_{l1} = 1.0$ MSSIM =0.910

(e) PWLS-TV-ℓ1,200, $\lambda_{tv} = 0.3, \lambda_{l1} = 0.2$, MSSIM=0.904

(f) PWLS-TV-ℓ1,200, $\lambda_{tv} = 0.3, \lambda_{l1} = 0.5$, MSSIM=0.917

(g) PWLS-TV-ℓ1,200, $\lambda_{tv} = 0.3, \lambda_{l1} = 0.8$, MSSIM=0.930

(h) PWLS-TV-ℓ1,200, $\lambda_{tv} = 0.3, \lambda_{l1} = 1.0$, MSSIM=0.952

(i) PWLS-TV-ℓ_1,400 $\lambda_{tv} = 0.4, \lambda_{l1} = 0.2$ MSSIm =0.916

(j) PWLS-TV-ℓ_1,400 $\lambda_{tv} = 0.4, \lambda_{l1} = 0.5$ MSSIM =0.936

(k) PWLS-TV-ℓ_1,400 $\lambda_{tv} = 0.4, \lambda_{l1} = 0.8$ MSSIM =0.957

(l) PWLS-TV-ℓ_1,400 $\lambda_{tv} = 0.4, \lambda_{l1} = 1.0$ MSSIM =0.951

Figure 4.8: SSIM images and MSSIM values corresponding to the images in Fig.4.7 (e)-(h) reconstructed by use of the PWLS-TV-ℓ_1 method with 100 views, are shown in subfigures (a)-(d); SSIM images and MSSIM values corresponding to the images in Fig.4.7 (i)-(l) reconstructed by use of the PWLS-TV-ℓ_1 method with 200 views, are shown in subfigures (e)-(h); SSIM images and MSSIM values corresponding to the images in Fig.4.7 (m)-(p) reconstructed by use of the PWLS-TV-ℓ_1 method with 400 views, are shown in subfigures (i)-(l). All images are displayed in the same window [0 1].

SSIM images and MSSIM values corresponding to the PWLS-TV-ℓ1 images in Fig. 4.7 are displayed in Fig. 4.8. The SSIM images corresponding to the PWLS-TV-ℓ1 method possess

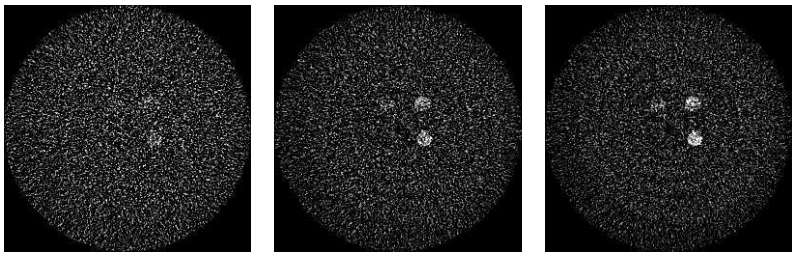

(a) FBP, 125 views (b) FBP, 625 views (c) FBP, 1250 views

Figure 4.9: Physical Phantom Experiment: Reconstructed images of the K-edge material by use of FBP algorithm for 125, 625 and 1250 projection views, respectively. All images are displayed in the same grey-scale window.

a bright background with a majority of pixel values close to 1, indicating high similarity to the reference image, for all cases. The major difference between the SSIM images for three reduced-view cases is that the intensity values become slightly larger as the view number increases from 100 to 400. This reflects that reconstructed image bias is reduced as the number of view angles utilized is increased. The MSSIM values for the images confirm these findings.

4.4 Phantom Experiment with Targeted Ytterbium-Nanoparticles

Images reconstructed by use of the FBP algorithm from the few-view experimental data sets are displayed in Fig. 4.9. As can be seen, it is difficult to visually identify the structures in the image reconstructed from 125 views. Even in the images reconstructed from 625 and 1250 views, the noise level appears high. The images reconstructed by use of the PLS-TV, PWLS-TV, and PWLS-TV-$\ell 1$ methods from 125 views and 625 views are displayed in Fig. 4.10 and Fig. 4.11, respectively. The 125-view results (Fig. 4.10) indicate that the use of the estimated variances increases conspicuity of the low-contrast ytterbium probe (Fig. 4.10(b)). In addition, the positive impact of TV-regularization can be readily observed. A comparison between Fig. 4.10(d-f) and (g-i) demonstrates that the additional ℓ_1-norm regularization can suppress spurious background noise and preserves structural accuracy. Similar conclusions follow from the 625-view results (Fig. 4.11). Both the 125-view PWLS-TV-$\ell 1$ and 625-view

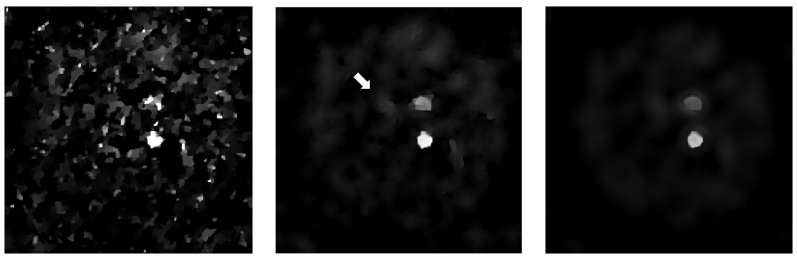

(a) PLS-TV, $\lambda_{tv} = 2.5 \cdot 10^{-4}$ (b) PLS-TV, $\lambda_{tv} = 3 \cdot 10^{-4}$ (c) PLS-TV, $\lambda_{tv} = 3.5 \cdot 10^{-4}$

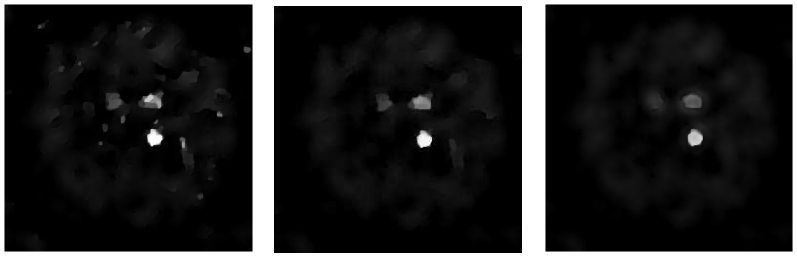

(d) PWLS-TV, $\lambda_{tv} = 1.5$ (e) PWLS-TV, $\lambda_{tv} = 2$ (f) PWLS-TV, $\lambda_{tv} = 3$

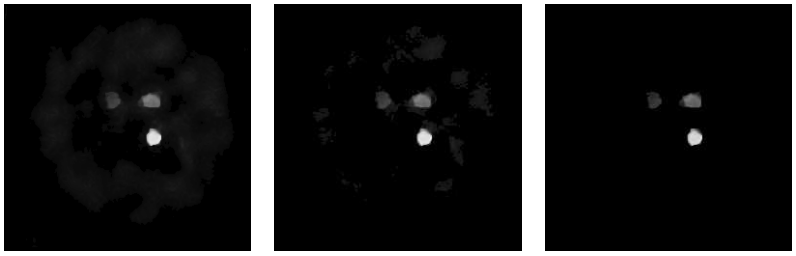

(g) PWLS-TV-ℓ_1, $\lambda_{tv} = 2$, $\lambda_{l1} = 0.1$ (h) PWLS-TV-ℓ_1, $\lambda_{tv} = 2$, $\lambda_{l1} = 0.3$ (i) PWLS-TV-ℓ_1, $\lambda_{tv} = 2$, $\lambda_{l1} = 0.45$

Figure 4.10: Physical Phantom Experiment: Reconstructed images of the K-edge material from 125 projection views. Image reconstructed by use of the PLS-TV method (a-c), PWLS-TV method (d-f), and PWLS-TV-ℓ_1 method (g-i). The arrow in subfigure (b) indicates the tube containing the low-concentration, ytterbium dilution, which becomes more visible in the images estimated by use of the PWLS methods. All images are displayed in the same grey-scale window.

PWLS-TV-ℓ1 images possess a relatively clean background and reveal the third low-contrast ytterbium probe.

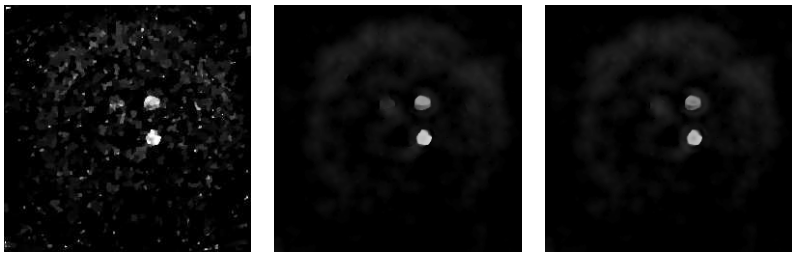

(a) PLS-TV, $\lambda_{tv} = 3.0 \cdot 10^{-4}$ (b) PLS-TV, $\lambda_{tv} = 4.0 \cdot 10^{-4}$ (c) PLS-TV, $\lambda_{tv} = 4.5 \cdot 10^{-4}$

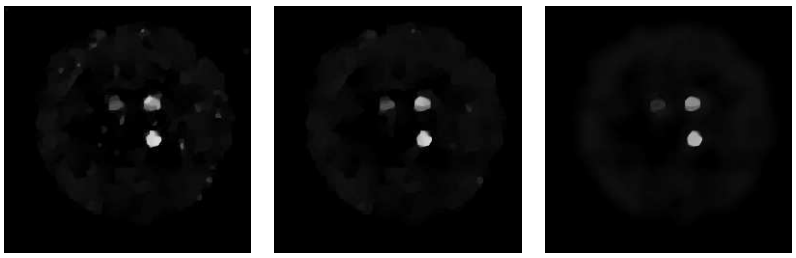

(d) PWLS-TV, $\lambda_{tv} = 2.5$ (e) PWLS-TV, $\lambda_{tv} = 3.5$ (f) PWLS-TV, $\lambda_{tv} = 4.0$

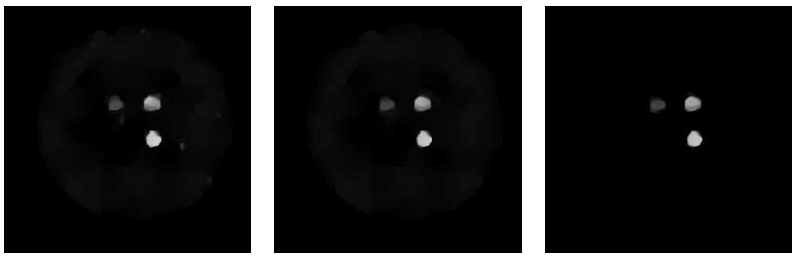

(g) PWLS-TV-ℓ_1, $\lambda_{tv} = 3.5$, $\lambda_{l1} = 0.1$ (h) PWLS-TV-ℓ_1, $\lambda_{tv} = 3.5$, $\lambda_{l1} = 0.3$ (i) PWLS-TV-ℓ_1, $\lambda_{tv} = 3.5$, $\lambda_{l1} = 0.45$

Figure 4.11: Physical Phantom Experiment: Reconstructed images of the K-edge material from 625 projection views. Image reconstructed by use of the PLS-TV method (a-c), PWLS-TV method (d-f), and PWLS-TV-ℓ_1 method (g-i). The arrow in subfigure (b) indicates the tube containing the low-concentration, ytterbium dilution, which becomes more visible in the images estimated by use of the PWLS methods. All images are displayed in the same grey-scale window.

4.5 Summary

We have proposed and investigated PWLS-TV and PWLS-TV-ℓ_l methods for reconstructing distributions of K-edge materials from reduced-view data in spectral CT [176]. It was

demonstrated that, by incorporating the variance information of the decomposed sinograms in the reconstruction method, the PWLS-TV method possessed a noise-to-spatial-resolution trade-off that was superior to a PLS-TV method that ignored the variance information. It was also demonstrated that, by promoting object sparsity in a wavelet transfrom domain, the PWLS-TV-ℓ_l method could improve the fidelity of small structures and remove isolated noises from images reconstructed from reduced-view datasets. This can be particularly useful for preclinical *in-vivo* applications of K-edge imaging, which are currently limited by long scan-times. It is worthwhile to mention that in this study, statistical correlations between decomposed sinograms were not exploited. However, this allows to reconstruct K-edge images individualy, which minimizes the computational burden and yields short computation times. The incorporation of the full covariance matrix in the reconstruction process can potentially reduce noise levels further but presents computationally challenges [135] that are a topic of current investigation.

Chapter 5

Accelerated fast iterative shrinkage thresholding algorithms for sparsity-regularized cone-beam CT image reconstruction with ordered subsets

5.1 Introduction

X-ray cone-beam computed tomography (CBCT) employing a circular scanning geometry is a widely employed three-dimensional (3D) imaging modality with numerous applications that include image-guided radiation therapy (IGRT), micro-computed tomography (CT), and dental imaging, to name only a few. There exist a vast literature related to the development and application of CBCT image reconstruction methods, and we refer readers to the recent literature for representative examples [19, 36, 72, 82, 85, 123, 130, 138]. The potential advantages of iterative algorithms over analytical algorithms are well-known, and include the flexibility to incorporate physical factors in the imaging model and effectively mitigate data incompleteness and noise. The development of iterative image reconstruction algorithms that implement non-smooth regularizers, including the TV penalty and other sparsity-promoting forms, remains an active and important research area [149, 151]. Even with hardware acceleration, however, the overwhelming majority of the available 3D iterative algorithms that

implement non-smooth regularizers remain computationally burdensome and have not been translated for routine use in time-sensitive applications such as IRGT.

The fast iterative shrinkage thresholding algorithm (FISTA) [14, 15] is a state-of-the-art optimization algorithm that possesses several characteristics that are well-suited for iterative CBCT image reconstruction. However, it remains largely unexplored for this important application. Because it can be employed to minimize a cost function that is specified by the sum of a smooth and convex data fidelity term and a convex but possibly non-smooth penalty, the FISTA can be employed for PLS reconstruction problems in which a TV penalty or other sparsity promoting forms are employed. Because it is based on a dual approach, the FISTA does not require approximate computation of the discretized TV function or the gradient discretized TV term, which most previously proposed algorithms require. The FISTA can also readily incorporate positivity or other bound constraints. Mathematically, it has been proven that the FISTA achieves a second-order convergence rate. It can therefore potentially reduce the number of iterations required to produce an image of a specified image quality as compared to first-order methods such as the steepest decent method. However, because the FISTA employs a gradient-descent step, which is known to limit convergence rates in conventional algorithms, there remains an opportunity to modify it and obtain an accelerated second-order algorithm that will lead to further reductions in image reconstruction times.

In this work, two accelerated variants of the FISTA for PLS-based image reconstruction in CBCT are proposed. The algorithm acceleration is obtained by replacing the original gradient-descent step by a sub-problem that is solved by use of the ordered subset simultaneous algebraic reconstruction technique (OS-SART). One algorithm seeks to minimizes a PLS cost function involving a TV penalty while the second assumes a penalty formed as the sum of object TV plus a wavelet-sparsified ℓ_1 norm of the object. We also present efficient numerical implementions of the proposed algorithms that exploit the massive data parallelism of multiple graphics processings units (GPUs).

The remainder of the Chapter is organized as follows. In Section 2, the discrete CBCT image model and the formulation of the sparsity-regularized PLS reconstruction problems are reviewed. The standard FISTAs for solving these problems is also reviewed. Section 3 contains a detailed description the proposed accelerated forms of the FISTAs, which represents the primary contribution of this work. The improved convergence rates of the algorithms are

demonstrated and quantified by use of computer-simulated and clinical data sets in Sections 4 and 5, respectively. The article concludes with a discussion of the work in Section 6.

5.2 Background

5.2.1 Discrete imaging model for CBCT

We consider a discrete CBCT imaging model

$$\mathbf{b} = \mathbf{H}\mathbf{f}, \tag{5.1}$$

where $\mathbf{b} \in \mathbb{R}^M$ represents a lexicographically ordered vector describing the cone-beam projection data with M defined by the product of detector elements and number of tomographic views acquired. The vector $\mathbf{f} \in \mathbb{R}^N$ is a finite-dimensional approximation of the sought-after object function $f(\mathbf{r})$. In the algorithms described below, we assume without loss of generality that $\mathbf{f}$ is formed by use of voxel expansion functions. The $M \times N$ system matrix $\mathbf{H}$ represents a discrete approximation of the continuous-to-discrete imaging operator that maps $f(\mathbf{r})$ to $\mathbf{b}$. Accordingly, the system matrix $\mathbf{H}$ can incorporate physical factors such as the detector reponse, X-ray beam polychromaticity, and the effects of scattering. In this work, as described later, we will assume that $\mathbf{H}$ is simply defined as a discrete approximation of a divergent beam X-ray transform. However, the presented algorithms are applicable for inversion of any linear imaging equation of the form of Eq. (5.1).

5.2.2 PLS image reconstruction using sparsity-promoting penalties

We consider two PLS estimators [176] for CBCT image reconstruction. The first estimator, hereafter referred to as the PLS-TV estimator, is defined as

$$\hat{\mathbf{f}} \;=\; \arg\min_{\mathbf{f}\,\geq\,0} \left\|\mathbf{b} - \mathbf{H}\mathbf{f}\right\|_2^2 \;+\; 2\lambda_{tv}\|\mathbf{f}\|_{TV}, \tag{5.2}$$

where $\|\cdot\|_{TV} = \|\nabla(\cdot)\|_1$ and $\|\cdot\|_1$ denote the TV and ℓ_1 norms, and ∇ is a discrete 3D gradient. The second estimator, hereafter referred to as the PLS-TV-ℓ_1 estimator, is defined as

$$\hat{\mathbf{f}} \;=\; \arg\min_{\mathbf{f}\geq 0} \left\|\mathbf{b}-\mathbf{H}\mathbf{f}\right\|_2^2 \;+\; 2\lambda_{tv}\|\mathbf{f}\|_{TV} + 2\lambda_{\ell_1}\|\mathbf{\Phi}\mathbf{f}\|_1, \tag{5.3}$$

where $\mathbf{\Phi}$ is a sparsifying transform. Inclusion of the ℓ_1 norm in the penalty provides the opportunity to improve image quality over use of the TV norm alone, particularly with respect to preservation of fine structures [30, 48]. In the numerical studies below, $\mathbf{\Phi}$ was defined as a discrete Daubechies wavelet transform that involved three wavelet scales. The real-valued scalar quantities λ_{tv} and λ_{ℓ_1} are user-defined regularization parameters.

5.2.3 FISTA for solving the PLS-TV problem

Let

$$d(\mathbf{f}) \equiv \|\hat{\mathbf{b}}-\mathbf{H}\mathbf{f}\|_2^2, \tag{5.4}$$

and

$$g_{tv}(\mathbf{f}) \equiv\; 2\lambda_{tv}\|\mathbf{f}\|_{TV} + \delta_C(\mathbf{f}), \tag{5.5}$$

where δ_C is the indicator function that can be defined as

$$\delta_C(\mathbf{f}) = \begin{cases} 0 & \text{if } \mathbf{f}\in C, \\ +\infty & \text{elsewhere.} \end{cases}$$

A simple flowchart of standard FISTA [14] to solve the optimization problem Eq. (5.2) is provided in Algorithm 1, and its basic steps are summarized as follows. First, a gradient descent step is applied to the data fidelity $d(\mathbf{f})$ to obtain an intermediate image denoted as $\mathbf{x}_g$ as indicated by Eq (5.6). Second, Eq (5.7) represents a TV-proximal problem $prox_{1/L}(g_{tv})\big(x_g\big)$ that can be efficiently solved by the fast gradient projection algorithm (FGP) as an imiage denoising step [14]. We extended the original FGP algorithm for solving 2D proximal problem to our 3D CBCT circumstance and a description of this extension is provided in Appendix C. Finally, the solution of the proximal problem is employed to define a new image estimate that is substituted into the first step and the procedure is repeated until a convergence criteria is met.

Algorithm 1 FISTA-TV

Input: $L \geq L(d(f))$– An upper bound on the Lipschitz constant of $\nabla d(f)$
Initial Step: Take $\mathbf{e_1} = \mathbf{f_0} = \mathbf{0}$, $t_1 = 1$
for $k \leftarrow 1, n$ **do**

$$\mathbf{x}_g = \mathbf{e}_k - \frac{1}{L}\nabla d(\mathbf{e}_k) = \mathbf{e}_k - \frac{2}{L}H^T(H\mathbf{e}_k - \mathbf{b}) \tag{5.6}$$

$$\mathbf{f}_k = prox_{1/L}(g_{tv})(\mathbf{x}_g) = prox_{1/L}(2\lambda_{tv}\|\mathbf{f}\|_{TV})(\mathbf{x}_g) \tag{5.7}$$

$$t_{k+1} = \frac{1 + \sqrt{1 + 4t_k^2}}{2} \tag{5.8}$$

$$\mathbf{e}_{k+1} = \mathbf{f}_k + \frac{t_k - 1}{t_{k+1}}(\mathbf{f}_k - \mathbf{f}_{k-1}) \tag{5.9}$$

end for
Output: $\mathbf{f}_n$

5.2.4 Splitting-based FISTA for solving the PLS-TV-$\ell 1$ problem

The FISTA for solving the PLS-TV problem Eq. (5.2) cannot be applied directly for solving the PLS-TV-$\ell 1$ problem (Eq. (5.3)) because no efficient algorithms are currently available to directly solve the corresponding composite proximal problem.

To circumvent this difficulty, the composite splitting algorithm proposed by Combettes [37] can be employed to decompose the associated composite proximal problem into two sub-proximal problems. One is associated with the TV-penalty, which can be readily solved by the FGP algorithm. The other is associated with the ℓ_1 penalty involving the sparsifying transform Φ. Fortunately, when Φ corresponds to an orthogonal wavelet transform, the iterative shrinkage thresholding algorithm (ISTA) algorithm can efficiently solve this problem [15, 42]. According to Theorem 3.4 in reference [37]), the sequence generated by the average of the solutions of the two sub-proximal problems will converge to the solution of the original composite proximal problem. A flowchart of the splitting-based FISTA to solve the PLS-TV-ℓ_1 optimization problem in Eq. (5.3) is shown in Algorithm 2. Some details for efficiently solving the ℓ_1-proximal problem $prox_{1/L}(4\lambda_{\ell 1}\|\mathbf{\Phi f}\|_{\ell 1})(\mathbf{x}_g)$ in Eq. (5.12) by ISTA/FISTA algorithm can be founed in Appendix D. Equation (5.14) describes an operator that projects $\mathbf{f}_k$ into a feasible set with value range of [0 max].

Algorithm 2 FISTA-TV-$\ell 1$

Input: $L \geq L(d(f))$– An upper bound on the Lipschitz constant of $\nabla d(f)$
Initial Step: Take $\mathbf{e_1} = \mathbf{f_0} = \mathbf{0}$, $t_1 = 1$
for $k \leftarrow 1, n$ **do**

$$\mathbf{x}_g = \mathbf{e}_k - \frac{1}{L}\nabla d(\mathbf{e}_k) = \mathbf{e}_k - \frac{2}{L}H^T(H\mathbf{e}_k - \mathbf{b}) \tag{5.10}$$

$$\mathbf{f}_k^1 = prox_{1/L}(2\lambda_{tv}\|\mathbf{f}\|_{TV} \times 2)(\mathbf{x}_g) = prox_{1/L}(4\lambda_{tv}\|\mathbf{f}\|_{TV})(\mathbf{x}_g) \tag{5.11}$$

$$\mathbf{f}_k^2 = prox_{1/L}(2\lambda_{\ell 1}\|\mathbf{\Phi f}\|_{\ell 1} \times 2)(\mathbf{x}_g) = prox_{1/L}(4\lambda_{\ell 1}\|\mathbf{\Phi f}\|_{\ell 1})(\mathbf{x}_g) \tag{5.12}$$

$$\mathbf{f}_k = (\mathbf{f}_k^1 + \mathbf{f}_k^2)/2; \tag{5.13}$$

$$\mathbf{f}_k = project(\mathbf{f}_k, [0 \ \max]); \tag{5.14}$$

$$t_{k+1} = \frac{1 + \sqrt{1 + 4t_k^2}}{2} \tag{5.15}$$

$$\mathbf{e}_{k+1} = \mathbf{f}_k + \frac{t_k - 1}{t_{k+1}}(\mathbf{f}_k - \mathbf{f}_{k-1}) \tag{5.16}$$

end for
Output: $\mathbf{f}_n$

In the following section, the above algorithms are modified to form accelerated FISTAs that can benefit CBCT applications.

5.3 Accelerated FISTAs for image reconstruction in CBCT

5.3.1 Motivation and preconditioned ordered subsets acceleration strategies

The standard FISTA employs a basic gradient-descent step update [14],

$$\frac{1}{L}\nabla d(\mathbf{f}) = \frac{2}{L}\mathbf{H}^T(\mathbf{Hf} - \mathbf{b}) \tag{5.17}$$

to minimize $d(\mathbf{f})$, where L is the Lipschitz constant of $\mathbf{H^T H}$ that is equal to the maximum of the eigenvalue of $\mathbf{H^T H}$. Theoretically, for the standard FISTA algorithm, the achieved

second order convergence speed can be described as

$$F(f_k) - F(f^*) \leq \frac{2L\|f_k - f^*\|^2}{(k+1)^2}, \tag{5.18}$$

where $F(\cdot)$ is the object function, k is the iteration number, f_k is object (image) at the k-th iteration and f^* is the optimization point. Eq. (5.18) is simply Theorem 3.1 in reference [14]. The efficiency of the standard FISTA simply relies on being able to rapidly solve the second step, which is either TV-proximal problem or ℓ_1-proximal problem. However, for many medical image reconstruction problems, the basic gradient update step in Eq. (5.17) performed before solving proximal problems is the most time consuming part and limits the overall convergence speed. The simple reason is that it requires computation of the complete forward operator $\mathbf{H}$ and the backprojection operator $\mathbf{H^T}$ for each single update of the object function estimate. This can be computationally burdensome in CBCT due to the the large amount of projection data and the large dimensions of the 3D reconstructed volume. In addition, when the Lipschitz constant L is large, the update step size $1/L$ is small in the basic gradient step, which also indicates that more iterations need to be performed. Therefore, the gradient descent step will generally limit the computational efficiency of the FISTA when applied to CBCT image reconstruction.

Instead of employing all of the projection data at once to compute a gradient descent step, it is well known that an intermediate solution to a least squares minimization problem can be obtained more efficiently by employing a strategy in which the estimate of the object function is updated frequently by use of ordered subsets of the projection data sequentially [79]. Such approaches can dramatically improve the convergence rate of an iterative method over classic gradient descent methods. Therefore, many advanced iterative methods that solve the least square problem can be combined with the ordered subsets concept to accelerate the reconstruction progress. The simultaneous algebraic reconstruction technique (SART) [10], which is one type of block-iterative algorithms [31], has been considered as a very efficient converged method for CT reconstruction [31, 84]. Therefore, we chose the ordered subsets version of SART (OS-SART) [164] as one exmaple to accelerate 3D CBCT image reconstruction.

The type of OS-SART algorithm adopted in this work is now briefly explained. A ray model can be easily written as

$$\sum_{j=1}^{N} h_{ij} f_j = b_i, \quad i = 1, 2, \cdots, M, \tag{5.19}$$

where f_j is jth element of the vector $\mathbf{f}$, N is the total number of voxels, M is the number of total rays from all projection data, and h_{ij} is one weight element that represents the contribution of the jth voxel to the ith ray integral. For the ordered subsets version, we can rewrite Eq. (5.19) as

$$\sum_{j=1}^{N} h_{ij,v} f_j = b_{i,v}, \quad i = 1, 2, \cdots, M_v, \quad v = 1, 2, \cdots T, \tag{5.20}$$

where v represents one specific v-th subset, M_v is the total number of rays in v-th subset, T indicates the total number of subsets.

The OS-SART algorithm is composed of two sub-steps, a forward-correction step and a backprojection-update step. These two steps were carried out, respectively, by adopting the following two specific formulae:

$$c_{i,v} = \frac{b_{i,v}^{data} - \sum_{j=1}^{N} h_{ij,v} f_{j,v-1}^{k}}{\sum_{j=1}^{N} h_{ij,v}}, \tag{5.21}$$

$$f_{j,v}^{k} = f_{j,v-1}^{k} + \gamma_v \frac{\sum_{i}^{M_v} c_{i,v} h_{ij,v}}{\sum_{i}^{M_v} h_{ij,v}}, \tag{5.22}$$

where $b_{i,v}^{data}$ represents the ith ray projection data in the v-th subset, $f_{j,v-1}^{k}$ and $f_{j,v}^{k}$ are the jth voxel value updated by use of the $(v-1)$-th and the v-th subset, respectively.

Eq. (5.21) and Eq. (5.22) can be combined to write as a matrix-vector form [31],

$$\mathbf{f}_v^k = \mathbf{f}_{v-1}^k - \gamma_v \mathbf{D}_v \mathbf{H}_v^T \mathbf{U}_v (\mathbf{H}_v \mathbf{f}_{v-1}^k - \mathbf{b}_v), \tag{5.23}$$

where $\mathbf{H}_v$ is the v-th partition of the complete $\mathbf{H}$, $\mathbf{D}$ and $\mathbf{M}$ are two diagonal matrices. Matrix $\mathbf{U}_v$ is a weighte matrix given by

$$\mathbf{U}_v = \text{diag}\big\{1/\sum_{j=1}^{N} h_{ij,v+1} \quad | \quad i = 1, 2, \cdots, M_v\big\}. \tag{5.24}$$

Each element of matrix $\mathbf{U}_v$ is nothing but the reciprocal of the i-th ray length, which can be treated as a weight when other noise properties are not available. Matrix $\mathbf{D}_v$ is a preconditioned matrix given by

$$\mathbf{D}_v = \text{diag}\big\{1/\sum_{i=1}^{M_v} h_{ij,v} \quad | \quad j = 1, 2, \cdots, N\big\}. \tag{5.25}$$

Each element of matrix $\mathbf{D}_v$ is reciprocal of the sum of intersection lengths of rays which intersect with j-th voxel in the $v+1$-th subset. The two diagonal matrices $\mathbf{U}_v$ and $\mathbf{D}_v$ are automatically obtained without any extra computation when computing operators $\mathbf{H}_v$ and $\mathbf{H}_v^T$. Therefore, Eq. (5.23) can be reviewed as a pre-conditioned gradient based scheme with sequential update strategy. This form of matrix $\mathbf{D}_{v+1}$ has been proved to be a good pre-conditioned matrix to accelerate the convergence speed of a simple gradient step. One good property for this update strategy is that the spectrum $\rho\big(\mathbf{D}_v\mathbf{H}_v^T\mathbf{U}_v\mathbf{H}_v\big) \leq 1$ [31, 84]. Therefore, a relative large relaxation parameter γ_v (step size) can be used for early iterations to rapidly obtain a very good approximation to the solution of the least square problem.

Motivated by the above observations, we propose accelerated versions of the FISTAs in which the gradient descent step is replaced by an OS-SART subproblem. More specifically, Eq. (5.6) and Eq. (5.7) in Algorithm 1 will be replaced by an inner loop given by

$$\begin{cases} \text{for } v = 0, \ \cdots, \ T-1 \\ \quad \mathbf{e}_v^k = \mathbf{e}_{v-1}^k - \gamma_v \mathbf{D}_v \mathbf{H}_v^{\prime T}(\mathbf{H}^\prime{}_v \mathbf{e}_v^k - \mathbf{b}^\prime{}_v) \\ \quad \mathbf{f}_k = prox_{\gamma_v}^{D_v^{-1}}(g_{tv}/T)(\mathbf{e}_v^k) \\ \text{end} \end{cases}$$

Here, $\mathbf{H}' \leftarrow \mathbf{U}_v^{1/2}\mathbf{H}_v$ and $\mathbf{b}'_v = \mathbf{U}_v^{1/2}\mathbf{b}_v$. In addition, we have a new proximal problem $prox_{\gamma}^{D_v^{-1}}(g_{tv}/T)(\mathbf{e}_v^k)$ given by

$$prox_{\gamma}^{D_v^{-1}}(g_{tv}/T)(\mathbf{e}_v^k) = \arg\min_{\mathbf{u}} \Big\{ \frac{g_{tv}(\mathbf{u})}{T} + \frac{1}{2\gamma}\|\mathbf{u} - \mathbf{e}_{v+1}^k\|_{D_v^{-1}}^2 \Big\} \tag{5.26}$$

Here, the original penalty term $g_{tv}(\mathbf{u})$ was scaled by T, which is the total number of subsets, becuase of the subset update strategy. The proximal problem with weighted normed can also be efficiently solved by FGP algorithm since the matrix D_v is only a diagonal matrix. In a similar way, Eq. (5.10), Eq. (5.11) and Eq. (5.12) in Algorithm 2 can also be replaced by this order subsets strategy. Hereafter, the notation OS-SART-FISTA-TV (OSSF-TV) and OS-SART-FISTA-TV-ℓ_1 (OSSF-TV-ℓ_1) will be used to denote these two algorithms with OS-SART update strategy.

5.3.2 Some technical implementaion details

Number of subsets and data accessing order

In general, the achieved acceleration factor is approximately proportional to the number of subsets in which the entire projection data are divided [16] for early iterations. In this work, we considered each view of the projection data to be a subset, and the number of subsets was equal to the number of projection views. However, to treat each projection data as one subset in this ray-based model, some conditions must be met. Otherwise, numerical artifacts can be produced. This condition is that each voxel in our reconstructed area must be intersected with at least one ray in every subset. When no ray intersects with a specific voxel, the corresponding element of matrix $\mathbf{D}_v$ will be zero. Therefore, this specific voxel will not be updated at this subset, which may cause inaccuracy and artifacts. To circumvent this circumstance, we can either adjust the voxel size (pixel size in 2D) or employ more than one projection view as a subset in our proposed new algorithms.

Besides the number of subsets, the data-access ordering strategy will also affect the convergence speed for most cases. Several different strategies were proposed and investigated in previous works, which included the ordering methods of sequential access (SAS), fixed angles, random access [160], prime number decomposition [75], multilevel [67] and weighted

distance [116]. For the sake of simplicity, we empolyed two different strategies, sequential access and fixed angles, in this work. Additionally, different suffixes will be appended to the algorithm names to denote the different data access strategies employed in the OS-SART subproblem. Specifically, the first number will represent how many projections are included in one subset and the second number will denote the accessing order of subsets. For example, the OS-SART subproblem in an OSSF-TV-1-1 algorithm treats each projection as one subset and the subsets are accessed sequentially. The OS-SART subproblem in an OSSF-TV-1-4 algorithm still treats each projection as one subset but the access order of subsets is to jump every four sequential projection views (subsets), i.e., the view angle access order will look like 1,5, $\cdots$, (T); 2,6,$\cdots$, (T); 3,7,$\cdots$, (T), 4,8, $\cdots$, (T), where T denotes the total number of subsets. In the numerical studies below, an improved version of Siddon's ray-tracing model [81] was employed to calculate the system matrix weights.

Number of iterations to solve TV-proximal problem

After performing one full gradient step in standard FISTA-TV or FISTA-TV-ℓ_1 algorithms, only 20 iterations are generally enough for FGP algorithm to solve the TV-proximal problem with a good precision [14]. Additionally, this computation time to solve TV-proximal problem by use of GPU is negligible when compared to the previous gradient step since the computation complexity for FGP algorithm is only with cost $\mathbf{O}(N)$ [14]. On the other hand, in our proposed OSSF-TV algorithm or OSSF-TV-ℓ_1, only 1-2 iterations are enough for each subset. The simple reason is that the TV regularization term $g_{tv}(\mathbf{f})$ with the parameter λ_{tv} has been rescaled by the total number of subsets T. Therefore, FGP algorithm requires much fewer iterations to solve the corresponding TV-proximal problem with a much smaller regularization term. In this work, 20 iterations of FGP algorithm were employed in standard FISTA-TV and FISTA-TV-ℓ_1 algorithm and only 1 iteration was employed for each subset in our proposed OSSF-TV and OSSF-TV-ℓ_1 algorithms.

Preconditioned matrix and step size γ

It is well known that a good precondtioned matrix can accelerate the convergence speed [57]. In our case, the OS-SART algorithm implicitly incorporates a preconditioned matrix $\mathbf{D}_v$.

Better preconditioned matrices can be employed for this purpose. However, to do so may require addtional computing products with operator $\mathbf{H}_v^T$ and $\mathbf{H}_v^T$.

Mathematically, the step size γ_v should satisfy the condition $0 \leq \gamma_v \leq 2/\rho(\big(\mathbf{D}_v\mathbf{H}_v^T\mathbf{U}_v\mathbf{H}_v)$ to control the convergence. As mentioned in previous section, the spectrum for each subset update satisfies $\rho\big(\mathbf{D}_v\mathbf{H}_v^T\mathbf{U}_v\mathbf{H}_v\big) \leq 1$. Therefore, a general choice for γ_{v+1} will be $0 < \gamma_{v+1} < 2$. However, the step size γ_v can also be optimized to achieve the maximum decrease for each subset. For example, we could solve another optimization problem for each subset as

$$\begin{aligned}\gamma_v &= \arg\min_{\gamma_v \geq 0} \|H_v\mathbf{f}_v^k - \mathbf{b}_v\|_2^2 \\ &= \arg\min_{\gamma_v \geq 0)} \|\mathbf{H}_v\big(\mathbf{f}_{v-1}^k - \gamma_v\mathbf{D}_v\mathbf{H}_v^T\mathbf{U}_v(\mathbf{H}_v\mathbf{f}_{v-1}^k - \mathbf{b}_{(v)})\big) - \mathbf{b}_v\|_2^2 \end{aligned} \tag{5.27}$$

We could take the first order derivative of the above least square expression with respect to γ_v, and set it to be zero. Therefore, an analytic expression will be obtained for γ_v. However, this also involves at least one time additional computing products with operator $\mathbf{H}_v$ and $\mathbf{H}_v^T$ Although the iteration number can be reduced, the reconstruction time will actually be doubled.

Basic schemes of GPU implementation

Highly efficient parallel implementations of the OSSF-TV and OSSF-TV-ℓ_1 algorithms that can utilize a single or multiple GPUs are presented in Appendix D. Below, the rapid convergence rates of the OSSF-TV and OSSF-TV-ℓ_1 algorithms are demonstrated and quantified.

5.4 Computer-simulation studies

Computer-simulation studies were conducted to validate the proposed reconstruction algorithms and quantify their improvements in convergence rates over to the standard FISTAs described in Sections 2.3 and 2.4. Experimental data studies are described in Section 5.5.

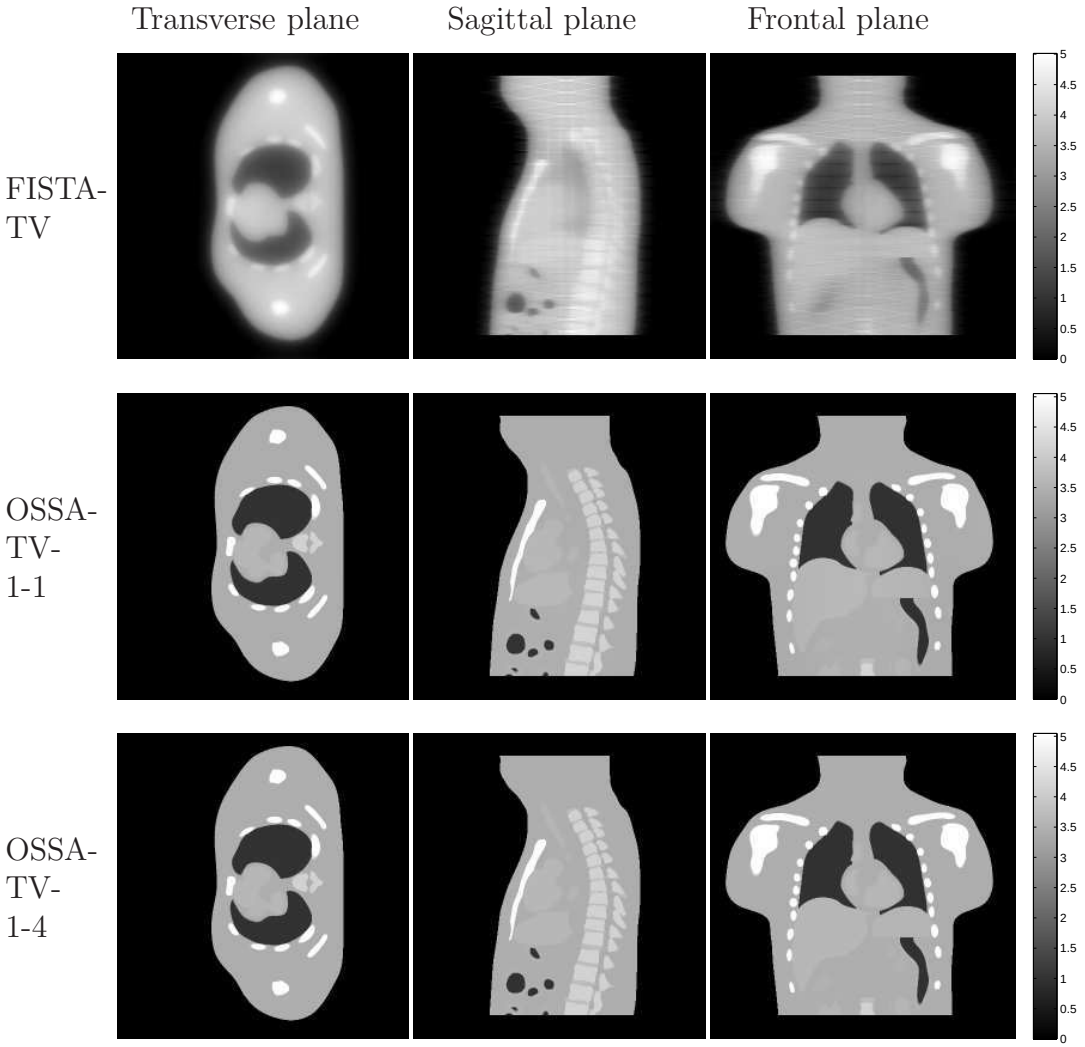

Figure 5.1: NCAT numerical phantom study for the full-view (360-view) case. Examples of images reconstructed by use of the FISTA-TV (top row), OSSF-TV-1-1 (middle row) and OSSF-TV-1-4 (bottom row) algorithms are displayed. Ten algorithm iterations were employed in all cases.

5.4.1 Numerical phantom and simulated projection data

A NCAT phantom [161] was adopted to represent the object function. The discrete phantom was represented by $256 \times 256 \times 256$ voxels of dimension 0.5 mm. We employed a circular

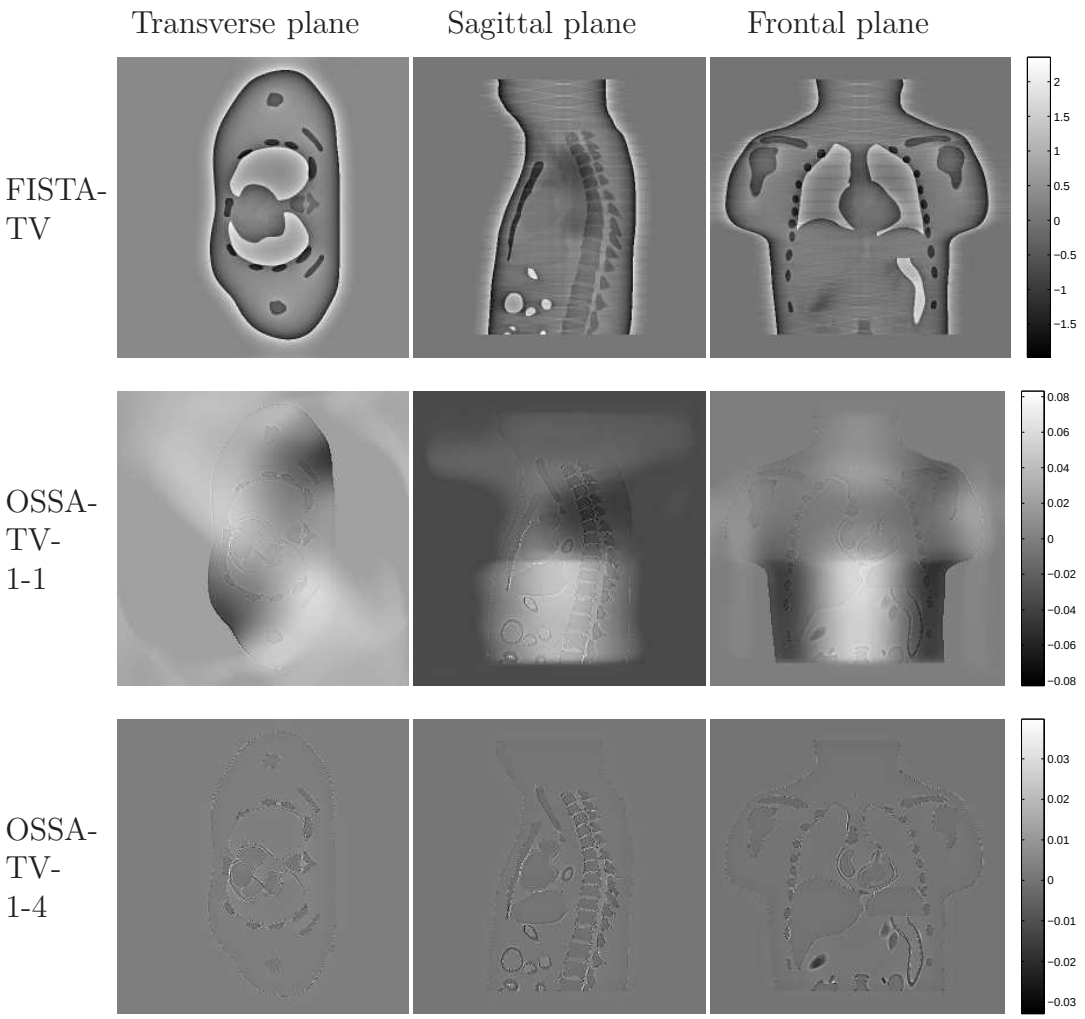

Figure 5.2: Error maps corresponding to the images displayed in Fig. 5.1.

CBCT imaging geometry with a source-to-rotation center distance of 50 cm and source-to-detector distance of 150 cm. The scanning geometry employed 360 tomographic views that were uniformly spaced over a 2π angular range. At each view, a flat detector with a physical size 20 cm $\times$ 20 cm was assumed that possessed 512×512 elements. The CBCT projection data were computed numerically by use of the system matrix described below and were contaminated by a 2% Gaussian noise. The complete set of projection containing all 360 views will be referred to as the 'full-view' data, while while an angularly subsampled version containing 45 equally spaced views will be referred to as the 'sparse-view' data. The reconstructed volumn has the same voxel number and size with the original phantom.

5.4.2 Full-view (360-view) case: Example images and corresponding error maps

Images reconstructed from the full-view noisy projection data by use of the standard FISTA-TV and the proposed OSSF-TV-1-1 and OSSF-TV-1-4 algorithms are shown in Fig. 5.1. All algorithms were terminated after 10 iterations. Images reconstructed by use of the FISTA-TV algorithm (first row in Fig. 5.1) have a signficantly blurred apperance, indicating that additional algorithm iterations are required to recover sharp boundaries and accurate pixel values. On the other hand, images reconstructed by use of the OSSF-TV-1-1 and OSSF-TV-1-4 algorithms contain accurate structures with high contrast, despite the use of only 10 iterations in the algorithms. To quantitatively examine the reconstructed images, error maps produced by substracting the reconstructed images from the true phantom, are shown in Fig. 5.2. The maximum magnitudes of the error maps obtained by the standard FISTA-TV algorithm are nearly two orders larger than those obtained from the proposed OSSF-TV algorithms. Moreover, the error maps reveal that the OSSF-TV-1-4 algorithm is more accurate thatn the OSSF-TV-1-1 algorithm, indicating that the data accessing strategy in the former algorithm is more effective.

5.4.3 Sparse-view (45-view) case: Example images and corresponding error maps

Images reconstructed from the sparse-view noisy projection data by use of the standard FISTA-TV and the proposed OSSF-TV-1-1 and OSSF-TV-1-4 algorithms and the associated error maps are shown in Figs. 5.3 and 5.4. All algorithms were terminated after 30 iterations. As in the full-view case, images reconstructed by use of the OSSF-TV-1-1 and OSSF-TV-1-4 algorithms both display sharper boundaries and higher contrast compared to the image reconstructed by use of the FISTA-TV algorithm. The maximum magnitude of the error map corresponding to the standard FISTA-TV algorithm is an order of magnitude larger than those corresponding to the OSSF-TV algorithms. Unlike in the full-view case, the OSSF-TV-1-4 algorithm shows a similar performance to the OSSF-TV-1-1 algorithm in this sparse-view case. This observation can be explained by the fact that the angular sampling is inherently sparse.

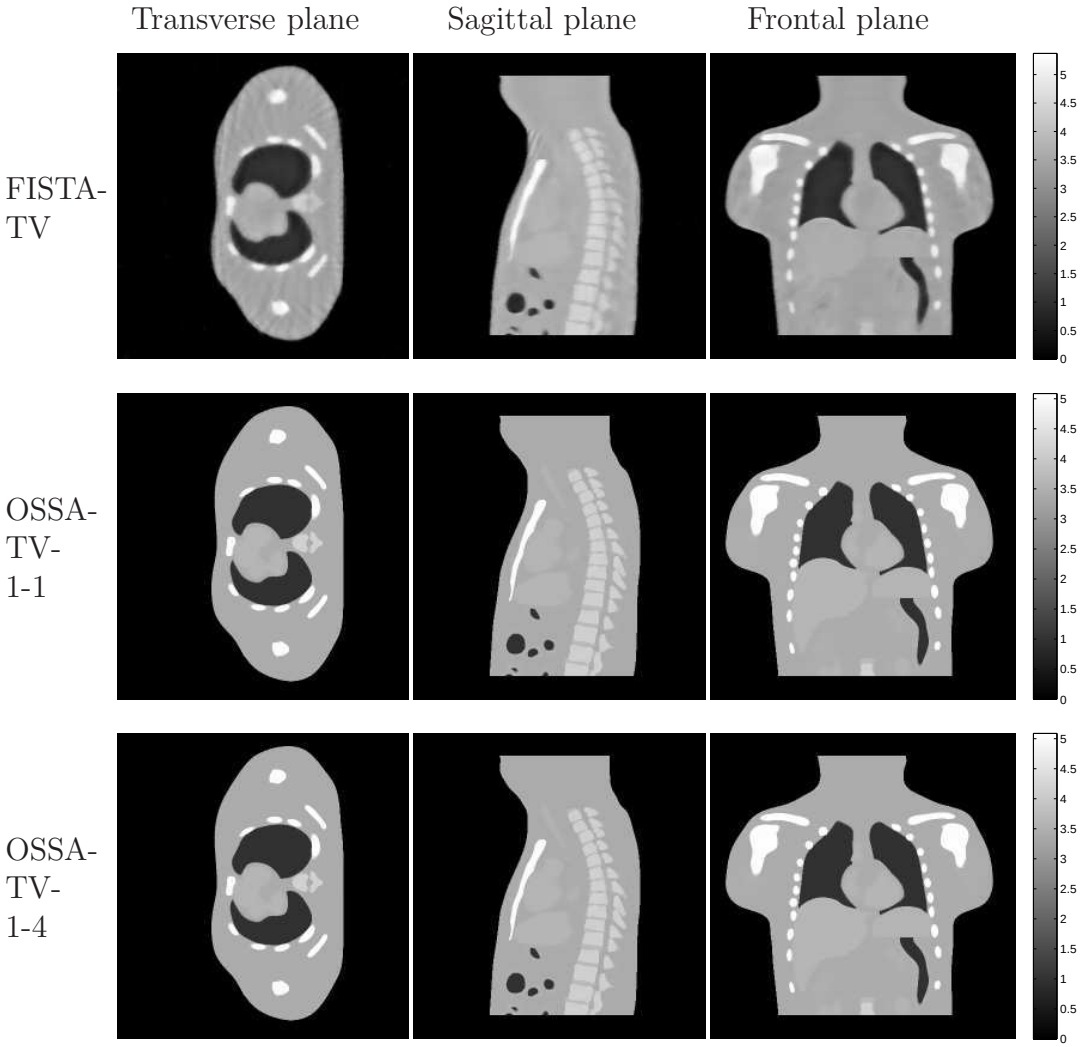

Figure 5.3: NCAT numerical phantom study for the sparse-view (45 view) case. Examples of images reconstructed by use of the FISTA-TV (top row), OSSF-TV-1-1 (middle row) and OSSF-TV-1-4 (bottom row) algorithms are displayed. Thirty algorithm iterations were employed in all cases.

5.4.4 Convergence and accuracy curves

To quantify the improvement in convergence rate yielded by the OSSF-TV algorithm, the objective function values $F(f) = ||\mathbf{b}-\mathbf{H}\mathbf{f}_{recon}||^2+2\lambda_{tv}||\mathbf{f}_{recon}||_{TV}$ were plotted as a function of

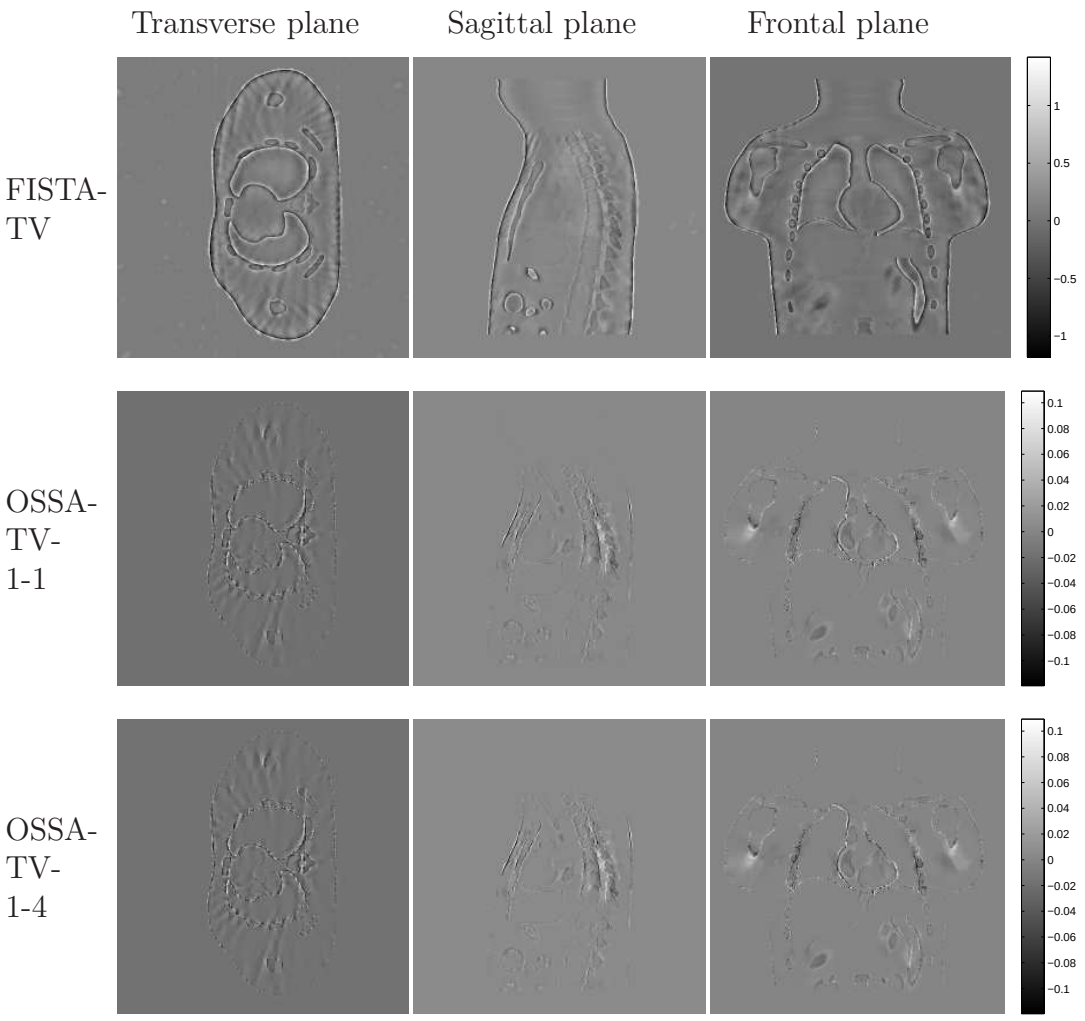

Figure 5.4: Error maps corresponding to the images displayed in Fig. 5.3.

algorithm iteration. The curves corresponding to the FISTA-TV OSSF-TV-1-1 and OSSF-TV-1-4 algorithms are displayed in Fig. 5.5 for both the full- and sparse-view cases. For the full-view case (Fig. 5.5-(a)), both the OSSF-TV-1-4 and the OSSF-TV-1-1 algorithms produce a more rapid decay in the objective function values than the FISTA-TV algorithm, reflecting that they possess improved convergence rates. Specifically, the OSSF-TV-1-4 curve indicates that the convergence has been approximately achieved by the 6th iteration in the full-view case. Even for the OSSF-TV-1-1 curve, only 16 iterations were required to achieve this. On the other hand, the curve corresponding to the FISTA-TV algorithm indicates that the algorithm requires more than one hundred iterations to achieve approximate convergence

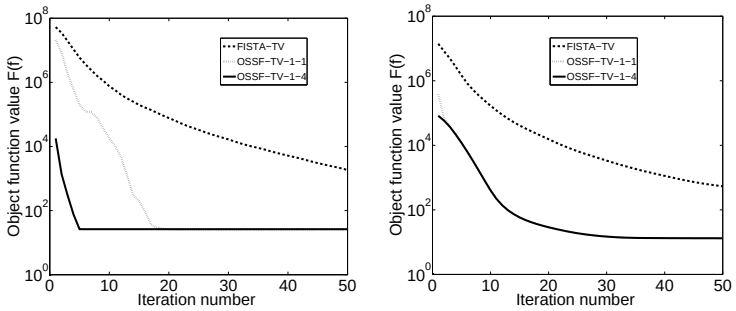

Figure 5.5: Convergence analysis: Plots of the objective function value as a function of iteration number for the FISTA-TV and OSSF-TV algorithms for the (a) full-view (360-view) case and (b) few-view (45-view) case.

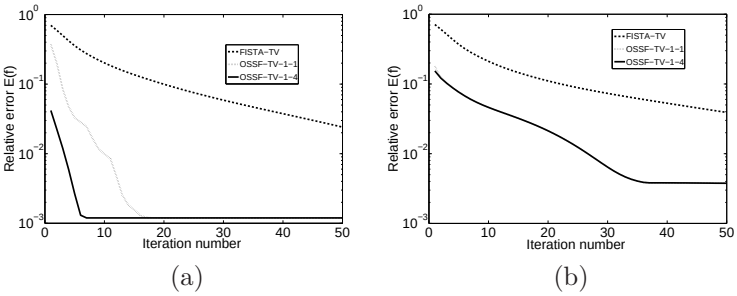

Figure 5.6: Accuracy analysis: Plots of the image RE as a function of iteration number for the FISTA-TV and OSSF-TV algorithms for the (a) full-view case and (b) few-view case.

for the full-view case. (Note: for display purposes we truncated the curve at the 50th iteration.) Similar observations regarding the relative convergence rates of the algorithms are obtained for the sparse-view case shown in Fig. 5.5-(b).

The relative error (RE) defined by $E(f) = \|f^{recon} - f^{true}\|_2 / \|f^{true}\|_2$, where f^{recon} represents the reconstructed images and f^{ture} represents the true phantom image, was also computed and plotted as a function of iteration number for the three algorithms and are displayed in Fig. 5.6 for the full- and sparse-view cases. The relative behavior of the RE curves is similar to that of the convergence rate curves described above. The values of REs indicates that the solution of the optimization problem indeed matches well with the true phantom.

The above results corroborate our claim that the OSSF-TV algorithms possess superior convergence rates as compared to the standard FISTA-TV algorithm while maintaining reconstruction accuracy. We have also verified that the OSSF-TV-ℓ_1 algorithm outperforms the FISTA-TV-ℓ_1 algorithm in a similar way.

5.4.5 Reconstruction time by using GPUs

Additional studies were conducted to quantify image reconstruction times that can be achieved when the proposed algorithms are implemented on currently available hardware. RE curves as a function of reconstruction time are plotted in Fig. 5.7 for the case when a single GPU (Figs. 5.7-(a) and (b)) or four GPUs (Figs. 5.7-(c) and (d)) were employed in the implementation. For the single-GPU case with full-view data (Fig. 5.7-(a)), the OSSF-TV-1-4 algorithm requires only 35 seconds to reach the approximate convergence point. With the sparse-view data, it requires approximatley 50 seconds. However, it should be noted that diagnostically useful images may be produced by the algorithm before this degree of convergence is obtained. With the four-GPU implementation, the OSSF-TV-1-4 algorithm required 10 seconds to converge with the full-view data and 15 seconds for the sparse-view case. These results are consistent with the claim in Appendix D that the multi-GPU implementations of the OSSF-TV algorithm will provide a speed-up over the single-GPU implementation that is approximately proportional to the number of GPUs employed.

5.5 Confirmation of algorithm performance using clinical data

The rapid convergence rates of the OSSF-TV and OSSF-TV-ℓ_1 algorithms were corroborated by use of clinical CBCT projection data. Because the OSSF-TV and OSSF-TV-ℓ1 algorithms both employed the -1-4 data accessing strategy in these studies, the suffix -1-4 to the algorithm names is omitted below.

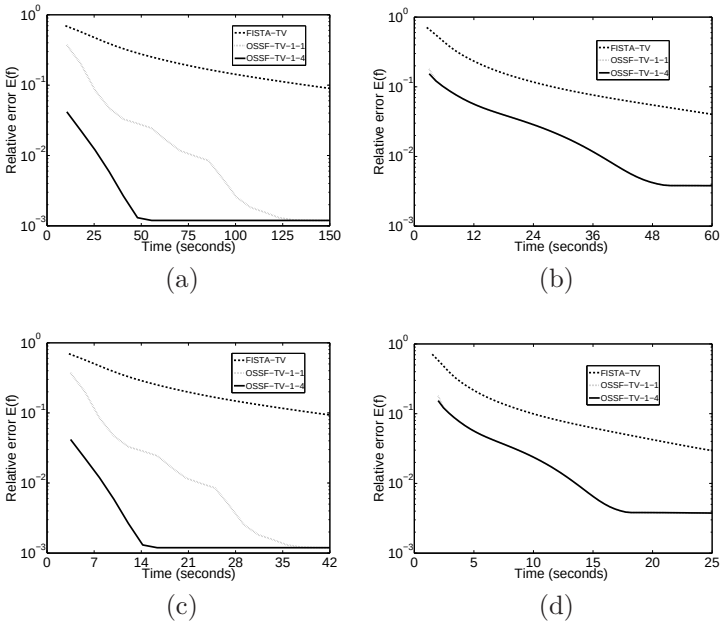

Figure 5.7: Plots of image RE as a function of reconstruction time for (a) full-view case with one GPU, (b) few-view case with one GPU; (c) full-view case with four GPUs, and (d) few-view case with four GPUs;

5.5.1 Experimental data and image reconstruction

Previously acquired circular CBCT projection data corresponding to a head-and-neck cancer patient were obtained under an IRB approved study. The data were acquired by use of a kilovoltage (kV) On-Board Imager (OBI) on a Varian TrueBeam radiation therapy treatment machine (Varian Medical System, USA). The source-to-axis distance (SAD) and detector-to-axis distances were 100 cm and 50 cm, respectively. A flat panel detector of size 30cm (768 rows) $\times$ 40cm (1024 columns) was employed. Additional details regarding the imaging hardware are described elsewhere [157]. The data were originally collected for IGRT purposes and contained 364 uniformly spaced tomographic views that spanned an angular range of approximately 200 degrees.

The acquired raw projection data were subjected to 5 pre-processing steps: scattering correction, air normalization, bow-tie filtration and beam-hardening correction and logarithm transformation, as described in a previous study [157]. From the processed projection data,

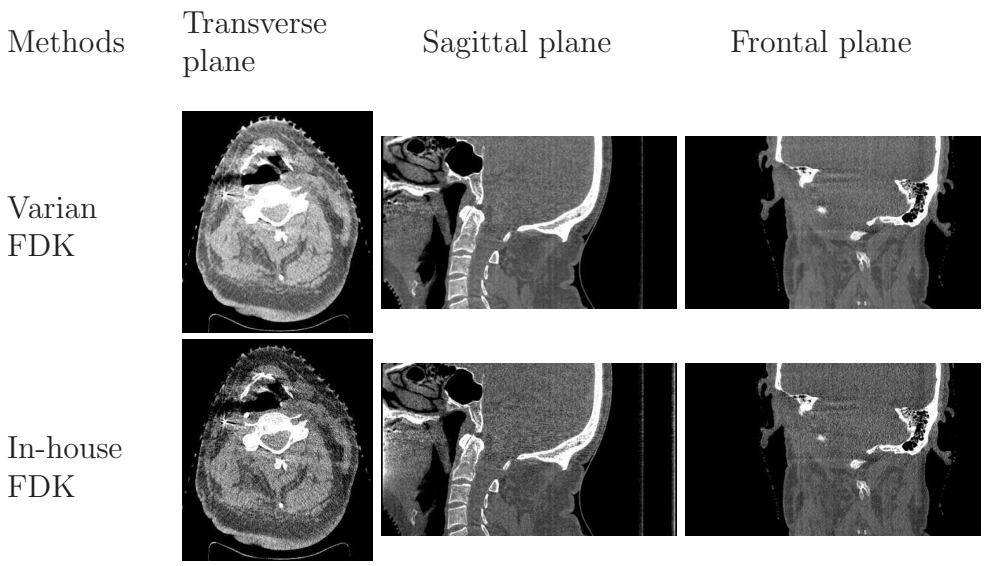

Figure 5.8: Example images corresponding to three orthogonal planes reconstructed by a Varian imager system and in-house FDK algorithm. First row: image reconstructed by Varian imager system, Second row: image reconstructed by our in-house FDK algorithm with a simple ramp filter. The transverse images are shown in a soft-tissue window [-300 200]HU. The sagittal and frontal images are shown in a display window [-500 800]HU.

the images reconstructed from the commerical software package in the Varian Imager system and our in-house FDK algorithm with a simple ramp filter, are shown in Fig. 5.8. With the same projection data, we obtained our reference images shown in Fig. 5.9 by running the standard FISTA-TV and FISTA-TV-ℓ_1 algorithms until convergence. They are employed to evaluate the convergence speed of our proposed OSSF-TV and OSSF-TV-ℓ_1 algorithms, respectively. For our proposed OSSF-TV and OSSF-TV-ℓ_1 algorithms, the proposed multi-GPU scheme with four K20x GPUs was employed for this reconstruction. All reconstructed images were of dimension $512 \times 512 \times 379$ (slices) with a voxel size of 0.512 mm.

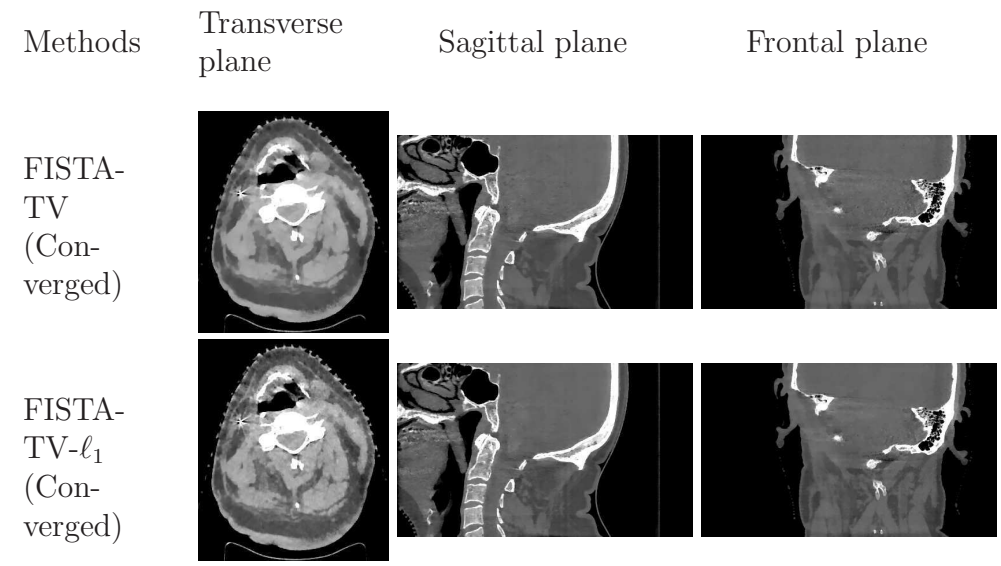

Figure 5.9: Reference images reconstructed by the standard FISTA-TV (converged) and FISTA-TV-ℓ_1 (converged). First row: reconstructed by standard FISTA-TV algorithm. Second row: reconstructed by the standard FISTA-TV-ℓ_1 algorithm.

5.5.2 Demonstration of rapid convergence rate with experimental data

A series of images corresponding to three orthogonal planes through the volumetric images produced by the OSSF-TV algorithm at iteration numbers $K = 1, 5, 10$, and 20 are shown in Figure 5.10. These images reveal that the visual appearances of the images after the 5th iteration do not considerably vary. This observation is consistent with the behavior of the error maps corresponding to the three planes that are displayed in the Figs. 5.11. Those error images were produced by subtracting the OSSF-TV reconstructed images from the reference image produced by the standard FISTA-TV algorithm. The error maps reveal that homogeneous tissue regions have been accurately recovered by the 5th iteration. The tissue interfaces and small bone features have been accurately recovered by the 10th iteration. By the 20th iteration, the values of the error maps were approximately zero reflecting that the image is nearly identical to the reference image.

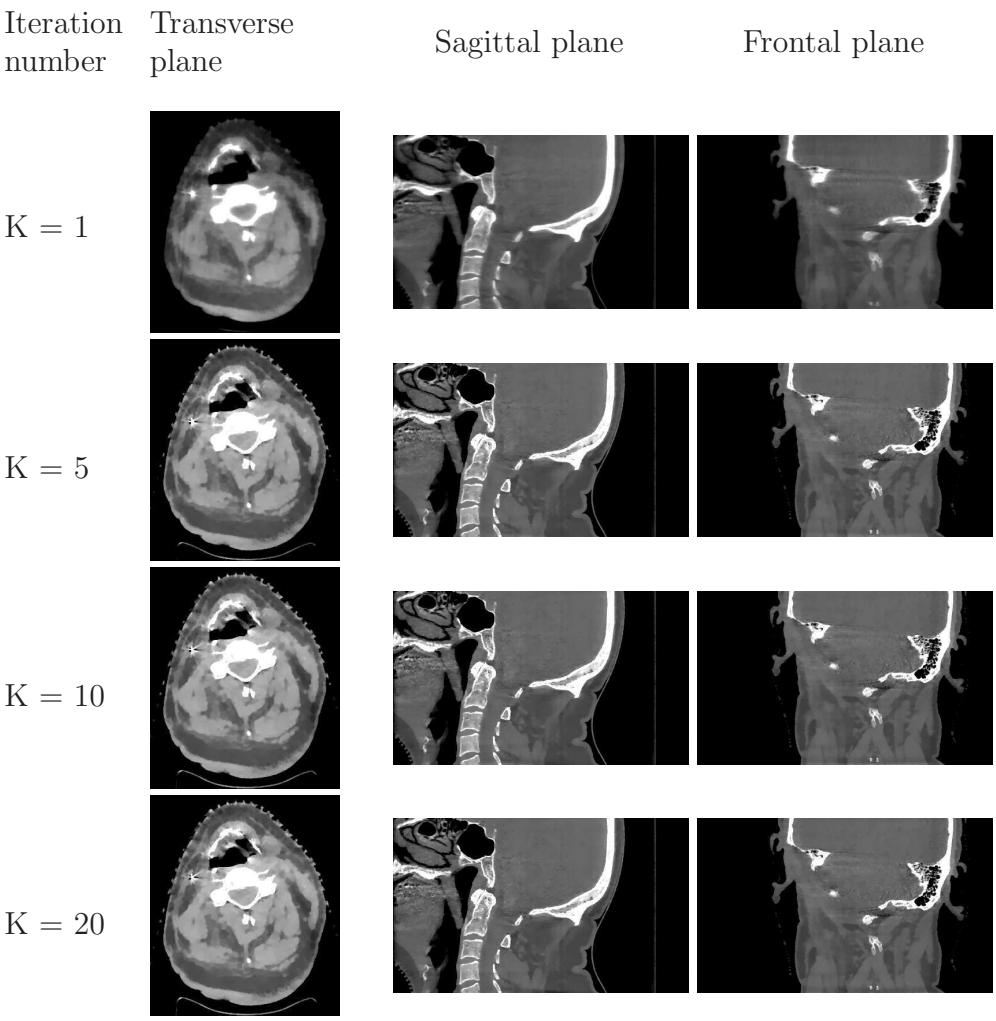

Figure 5.10: Example images corresponding to different iteration numbers (K) for the OSSF-TV algorithm. First Column: the selected transverse slice with soft-tissue display window [-300 200]HU, Second column:the selected sagittal plane with display window [-500 800]HU, Third column: the chosen frontal plane with display window [-500 800]HU.

The same image planes reconstructed by use of the OSSF-TV-ℓ_1 algorithm at iteration numbers $K = 1, 5, 10$, and 20 are shown in Figure. 5.12. The corresponding error maps are displayed in Figure 5.13. The observations described above regarding the rapid convergence rate of the OSSF-TV algorithm are found to also describe the behavior of the OSSF-TV-ℓ_1 algorithm.

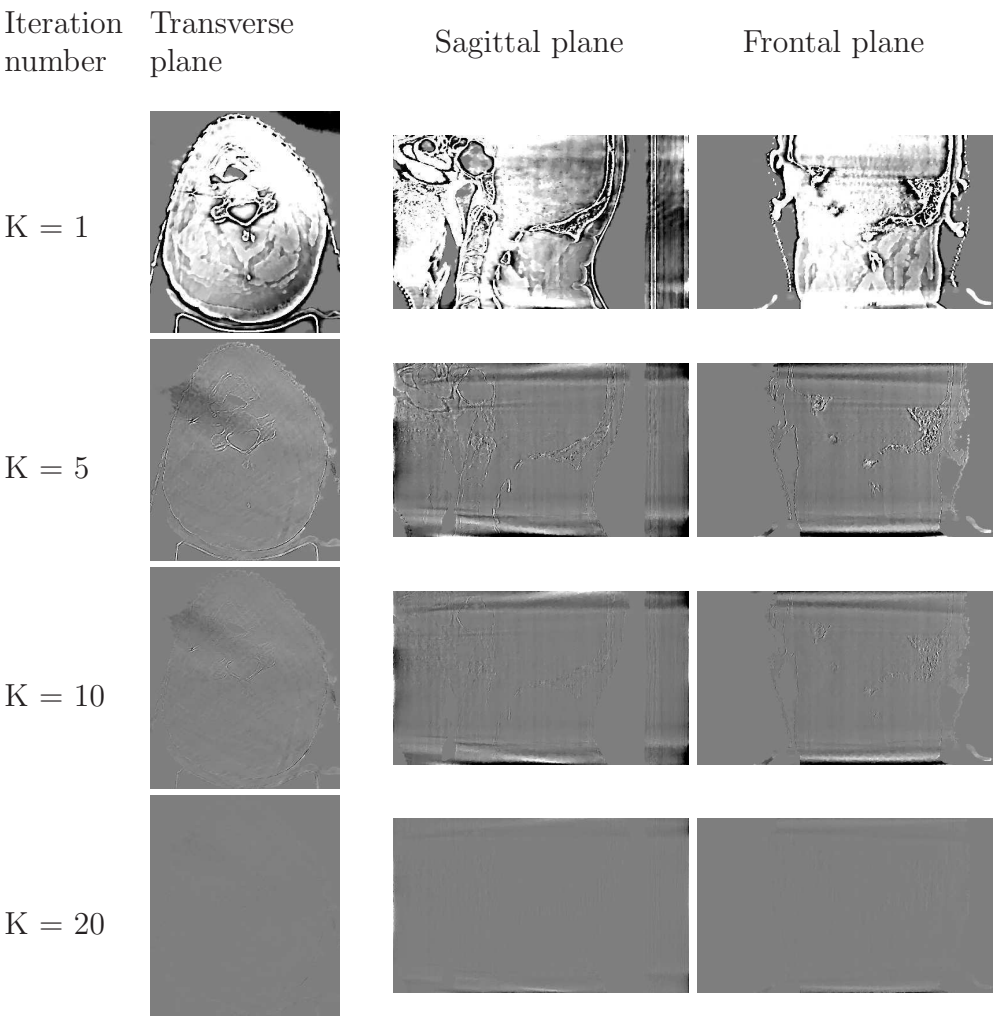

Figure 5.11: Error maps corresponding to different iteration numbers (K) for the OSSF-TV algorithm. The display window was [-50 50]HU. First Column: error maps for the selected transverse slice, Second column: error maps for the selected sagittal plane, Third column: error maps for the selected frontal plane. The reference image was produced by running the standard FISTA-TV until convergence.

5.6 Discussion

5.6.1 Convergence rate compared to some previous works

To better understand these achieved convergence rates, we chose several recent published works, which solve the same PLS-TV optimization problem, to do some brief comparison.

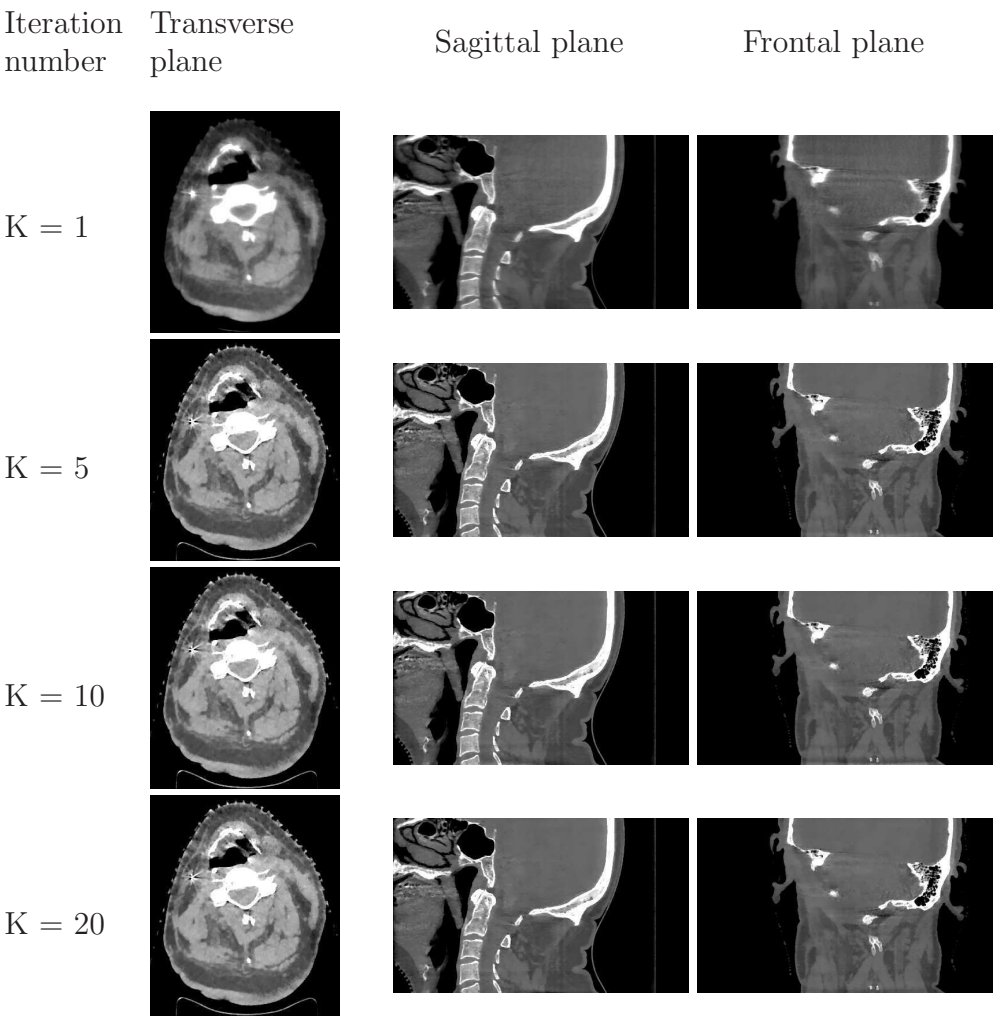

Figure 5.12: Example images corresponding to different iteration numbers (K) for the OSSF-TV-ℓ_1 algorithm. First Column: the selected transverse slice with soft-tissue display window [-300 200]HU, Second column:the selected sagittal plane with display window [-500 800]HU, Third column: the chosen frontal plane with display window [-500 800]HU.

The first example is that a previous work named gradient projection barzilai-borwein (GP-BB) proposed by Park [130] shows a RE curve for a 2D Shepp-Logan phantom in a fan-beam geometry by using only 40 uniform projection views. The proposed GP-BB algorithm in that work requires approximatelyl 20 iterations for the RE to decrease to 10%. We refer readers to see Fig. 5 in that work [130]. Another recent work by Niu et al [122] employed an unknown-parameter Nesterov (UPN) method, which is treated as an improved version of his

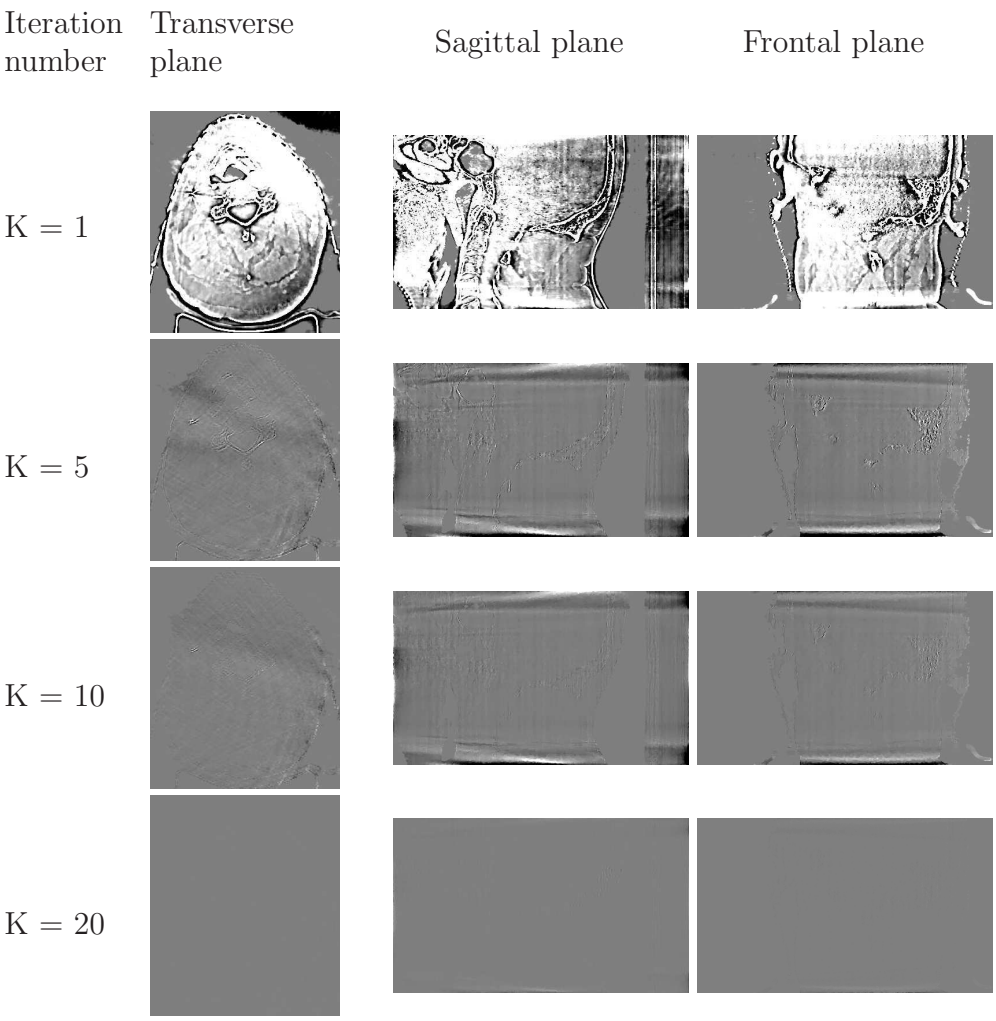

Figure 5.13: Error maps corresponding to different iteration numbers (K) for the OSSF-TV-ell_1 algorithm. The display window was [-50 50]HU. First Column: error maps for the selected transverse slice, Second column: error maps for the selected sagittal plane, Third column: error maps for the selected frontal plane. The reference image was produced by running the FISTA-TV-ℓ_1 algorithm until convergence.

previous gradient projection barzilai-borwein (GP-BB) method [123] for a 2D Shepp-Logan reconstruction by employing 66 projections. In this improved version, it still requires more than 60 iterations for the RE to decrease to 10%. We refer readers to Fig. 2 in that work [122]. The third example is that a previous work proposed by Jia [82] also shows a RE curve for a similar NCAT phantom reconstruction in the same CBCT geometry by employing only

40 envely distributed projection views. It takes approximately 50 iterations for the above proposed algorithm to achieve a RE value of 10%. We refer readers to Fig. 6 in that work [82]. On the other hand, the 45-view RE curve produced by our proposed OSSF-TV or OSSF-TV-ℓ_1 algorithm with a similar 3D NCAT phantom in the same CBCT geometry, is shown in Fig. 5.6(b) with a log-scale. As we can see, after only 3 iterations, the RE value of images reconstructed by the proposed OSSF-TV algorithms has decreased to 10%, and the RE values continue to decrease to 1% after only 25 iterations. In addition, even the standard FISTA-TV method only takes 22 iterations to reach the RE value of 10%. Based on the above comparison, we could clearly see and understand how superior the convergence rate can be achieved for our proposed algorithms. Mathamatically speaking, for the above exmaples, and other recently proposed algorithms [36, 85] that did not explicitly show RE curves to the gound truth, they all belong to the first-order type or Nesterov-type method. Therefore, their convergence rates will be slower than the standard FISTA-TV method with the second-order covnergence rate at the denoising step to solve the TV-proximal problem [14], and therefore slower than our proposed OSSF-TV or OSSF-TV-ℓ1 algorithms.

5.6.2 Computation complexity and reconstruction time

In general, it is relatively hard to compare the reconstruction times for previous different algorithms, since different hardward and different implementations will make the comparsion unfair or unreliable. However, we can simply calculate the computation complexity to estimate the relative time difference between them. For most aglorithms, the computation of products with $\mathbf{H}$ and $\mathbf{H}^T$ are very intensive in CT reconstruction and dominates the overall computation load [100]. In addtion, during one full iteration, at least one time product with $\mathbf{H}$ and $\mathbf{H^T}$ have to be performed for most all algorithms. For example, a basic gradient step includes only one time product with $\mathbf{H}$ and $\mathbf{H^T}$ to calculate the gradient $\nabla d(\mathbf{f}) = 2\mathbf{H^T}(\mathbf{Hf} - \mathbf{b})$ in one iteration. Our proposed OSSF-TV and OSSF-TV-ℓ_1 methods decouple the least square problems and TV regularization penalty or other sparsity penalties. This stragety avoids recalculating the gradient of the regularization terms in each subset. The adopted OS-SART breaks products with $\mathbf{H}$ and $\mathbf{H^T}$ in terms of block-rows of $\mathbf{H}$ and block-subcolumns of $\mathbf{H^T}$ in each subset. So effectively, similar to the basic gradient step, the adopted OS-SART only empolys one time product with $\mathbf{H}$ and $\mathbf{H^T}$ in one-full iteration,

which indicates that the computation time for the basic gradient step and one-full iteration of the OS-SART is nearly the same. In addition, the computation time of solving the TV-proximal or other proximal problems in our proposed can be negligible when compared to the computation burden of performing one-full iteration of OS-SART. Moreover, this decoupled two-step structure, which includes solving the least square problem and solving the TV-proximal or other proximal problems, is extremely suitable to exploit the parallel computation power.

5.6.3 Other recently published OS-type accelerating iterative algorithms with regularizations

Our original idea regarding use of the ordered subsets to accelerate the standard FISTA was first presented at 2012 AAPM John R. Cameron Young Investigator symposium [174]. During the preparation of our current draft, Fessler's group have also proposed several types of OS-type acceleration algorithms [87, 119] for helical CT. The former one combines a Augmented Lagrangian method with ordered subsets to solve a penalized weighted least square (PWLS) problem with Tikhonov regularization, the later one employs the ordered subsets to accelerate a nonuniform separable quadratic surrogate algorithm (NU-SQS) to solve the PWLS problem with Tikhonov regularization. Both works have very good performance to solve PWLS problems with Tikhonov regularization for helical CT. However, the structures and algorithms of both works are very different with our proposed methods. First, in both works, the employed ordered subsets [50] were performed for data fidelity term (least squares problem) and the regularization terms together. Therefore, unlike the decoupled structure in our proposed algorithm, this requires additional calculation of the gradient of the regularization terms (Tikhonov terms) in each subset besides the gradient of data fidelity term under the subset balance condition [50]. The total number of subsets could not be very large since having less measured data in each subset will likely break the subset balance condition [119]. In their second work [87], the nonuniform optimization transfer and averaging strategies were proposed mitigate the instability and convergence issue of the original OS algorithm. Second, the above OS-type algorithms may not be convenient to calculate the gradient of non-smooth and nondifferentialbe regularization terms, since they require calculation of the gradient of the regularization terms which our proposed algorithms do not. In addition,

before we submitted the current draft, another OS-momentum based algorithm [88] was also proposed to accelerate the standard FISTA algorithm by Fessler's group. To our best knowledge, the theoretical behavior of the OS-momentum algorithm is still under investigation.

5.7 Summary and conclusion

The FISTA is a state-of-the-art optimization algorithm that possesses a secord-order convergence rate and is suitable for minimizing PLS cost functions that contain non-smooth penalties. In this work, accelerated variants of the FISTA were proposed and investigated for CBCT image reconstruction. Algorithm acceleration was achieved by replacing the gradient-descent step in the standard FISTAs by an OS-SART subproblem. The proposed OSSF-TV and OSSF-TV-ℓ_1 algorithms solved PLS image reconstruction problems that utilized a TV penalty and the sum of a TV penalty and a wavelet-sparsified ℓ_1 norm penalty, respectively. However, the proposed approach to accelerating the FISTA can be applied readily to solve PLS reconstruction problems that utlize other sparsity-promoting penalty forms. By use of computer-simulated CBCT data, it was verified that the OSSF-TV and OSSF-TV-ℓ_1 algorithms possessed significantly greater convergence rates than the corresponding standard FISTAs. The rapid convergence properties of the algorithms were verified further by use of clincal CBCT data.

A reconstruction algorithm that possesses a rapid convergent rate can potentially produce a diagnostically useful image in fewer iterations than an algorithm that possesses a slower convergence rate. However, a rapid convergence rate does not necessarily translate into shortened reconstruction times. This depends on how efficiently each iteration can be computed. In order to reduce image reconstruction times in practice, we developed efficient GPU implementations of the proposed algorithms that utlize either a single or multiple GPUs. When multiple GPUs are employed, we demonstrated that the reduction in reconstruction time over the single GPU implemenation is approximately linear with the number of GPUs employed. The rapid convergence rates of the extremely simple structured algorithms coupled with efficient GPU implementations may make them suitable for certain timie-sensitive clinical applications.

The topic of optimizing image quality has intentionally not been addressed in this chapter, as our main focus has been on the development of accelerated iterative image reconstruction algorithms for CBCT. In our opinion, specification of the penalty form and regularization parameters in a PLS estimator that are most appropriate for a particular diagnostic task is a complicated undertaking. However, because the developed algorithms can drastically reduce image reconstruction times they can facilitate the systematic investigation of such issues.

The formulation of the reconstruction problems in this work have not explicitly exploited information regarding the statistical propertes of the projection data. Incorporating statistical formulation can potentially improve image quality in, for example, low-dose imaging applications. However, the proposed OSSF-TV and OSSF-TV-ℓ_1 algorithms can be generalized readily to exploit such statistical information. Specifically, the OS-SART subproblem in the accelerated algorithms can be modified to naturally incorporate information about the noise statistics in the projection data to formulate new system equations [41] and the rest of parts in our proposed algorithms remain the same. Additionally, the proposed algorithms can be explored for other CT imaging applications such as helical CBCT. The investigation of these topics can be pursued in future studies.

Chapter 6

Investigation of in-line X-ray phase-contrast tomosynthesis using an advanced iterative algorithm

6.1 Introduction

X-ray phase-contrast (XPC) imaging is a promising technique for visualizing soft tissue features in many biological applications [95,113,187,189]. There are several XPC imaging methods including crystal-based [162] and grating-based [169] varieties. In-line (or propagation-based) XPC is the simplest form to implement, requiring only a small X-ray focal spot, a high resolution detector and a sufficient propagation distance between the object and detector [171]. In practice, these requirements lead to longer acquisition times than conventional absorption-based radiography. These long acquisition times can be prohibitive for extending XPC computerized tomography (XPC CT) to pre-clinical and clinical scenarios. To circumvent this, tomosynthesis methods can be employed to reconstruct volumetric images from a relatively small number of projections at the cost of sacrificing spatial resolution in the depth-direction [47].

Conventional X-ray tomosynthesis, which is a form of limited angle tomography that employs only a few x-ray planar projections in a proper angular range to synthesize a collection of 2D images, has been widely studied for breast imaging and other medical imaging applications. There has been a high degree of research interest in tomosynthesis imaging in the past decade [6, 46, 64, 136]. Tomosynthesis allows for some level of low-resolution discrimination

between overlaying structures along the z direction (i.e., in-depth direction perpendicular to the in-plane images), bringing a substantial improvement in the ability to appreciate abnormal anatomy or disease in tomosynthesis images relative to conventional radiographs. Besides, the resolution of the reconstructed in-plane images is often believed to be superior to CT, at the same time tomosynthesis provides much reduced dose and faster acquisition time than that required for full CT datasets.

In recent years, a small number of studies [68] have explored XPC tomosynthesis imaging techniques. In 2010, Zhang *et al.* published in-line XPC tomosynthesis experimental results from data acquired with synchrotron radiation [181]. A phase retrieval filter was applied to the raw in-line projections so that the reconstruction problem was converted to be the same as conventional tomosynthesis. Hammonds *et al.* investigated in-line XPC tomosynthesis using a micro-focus x-ray tube in 2011 [70] A standard shift-and-add (SAA) algorithm was directly performed in the tomosynthesis reconstruction, and it showed that the reconstructed in-plane images (i.e. x-y plane shown in Fig. 6.1). could retain the edge enhancement that is observed in planar phase-contrast radiographs. Wu *et al.* conducted in-plane spatial resolution measurements of a phase-contrast tomosynthesis prototype using standard resolution test patterns [172], but certain details regarding the data-acquisition and reconstruction were not reported.

While the studies above show XPC tomosynthesis can provide boundary-enchanced in-plane images with better conspicuity than conventional tomosynthesis, there is a lack of studies that investigate the depth resolution (i.e. z-direction shown in Fig. 6.1) properties. In this contribution, we present a numerical investigation that compares the ability of conventional tomosynthesis and XPC tomosynthesis to distinguish depth positions of features in reconstructed images of a soft tissue phantom. We demonstrate that, for XPC tomosynthesis, the phase-contrast-induced features can help discriminate in-plane structures from out-of-plane structures, thus providing better z-resolution than conventional tomosynthesis. In addition, because previous XPC tomosynthesis studies employed simple reconstruction algorithms (e.g. SAA, FBP) that are susceptible to the incomplete and/or noisy data, we propose an advanced iterative algorithm that can better mitigate these factors.

The chapter is organized as follows. In Section 6.2, the in-line phase-contrast imaging model is briefly reviewed. We then propose an advanced iterative algorithm (OS-SART-FISTA) for

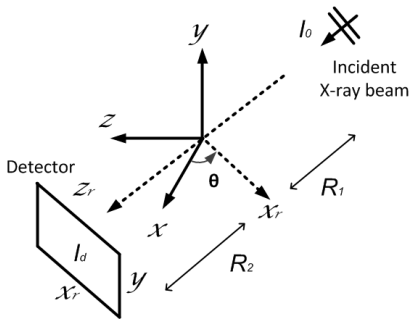

Figure 6.1: A schematic of the XPC imaging geometry is shown in which the object is fixed in a reference coordinate system (x, y, z). The source (not shown) and detector rotate about the y-axis.

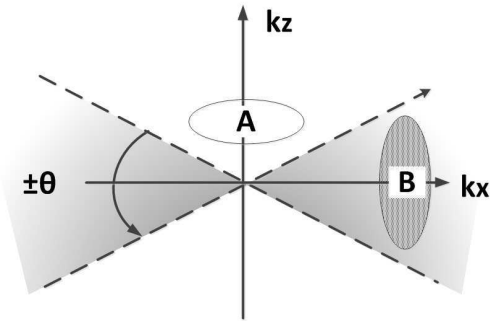

Figure 6.2: A frequency domain interpretation of tomosynthesis illustrates the reduced spatial resolution in the z-direction of reconstructed images. The shaded region indicates spectral information content of tomosynthesis measurements in the k_x and k_z plane. Region A indicates the (low) frequency information in k_z that is not contained in the measured data. Region B illustrates the preservation of some high frequency components in k_z.

XPC tomosynthesis reconstruction. Section 6.3 describes the computer-simulation studies and experimental studies, including imaging model validation, investigating different factors to affect the reconstructed image quality and depth resolution properties of XPC tomosynthesis. The corresponding results are shown in Section 6.4. In addition. some experimental results are present in Section 6.5. This chapter concludes with a summary in Section 6.6.

6.2 Background

6.2.1 XPC imaging model

The imaging geometry is depicted in Fig 6.1 in which a detector and source rotate about a fixed object. An object is irradiated by a monochromatic point X-ray source with wavelength λ in the direction of the positive z_r-axis. The y-axis of the fixed reference coordinate system (x, y, z) defines the rotation axis for tomographic scanning. The rotated coordinate system

(x_r, y, z_r) is related to the reference system by $x_r = x\cos\theta + z\sin\theta$ and $z_r = z\cos\theta - x\sin\theta$, where the tomographic view angle θ is calculated with respect to the positive x-axis. The x-ray wave field intensity incident on the object is given by $I_0(x_r, y, \theta)$. The transmitted wave field propagates a distance $z_r = R_2$ to a detector and the detected intensity is denoted by $I_d(x_r, y, \theta)$. [7]

The object can be characterized by its complex-valued refractive index distribution

$$n(\mathbf{r}) = 1 - \delta(\mathbf{r}) + j\beta(\mathbf{r}), \tag{6.1}$$

where $\mathbf{r} = (x, y, z)$. We define the total attenuation $A(x_r, y, \theta)$ and the total phase shift $\phi(x_r, y, \theta)$ as

$$A(x_r, y, \theta) = \exp(-k \int dz_r \beta(\mathbf{r})) \tag{6.2}$$

$$\phi(x_r, y, \theta) = -k \int dz_r \delta(\mathbf{r}), \tag{6.3}$$

where $k = 2\pi/\lambda$. $A(x_r, y, \theta)$ and $\phi(x_r, y, \theta)$ are calculated as integrals through the object along the X-ray beam path. This is approximately the z_r direction when we assume a small cone-beam angle approximation.

With the assumption that the object is weakly absorbing, the measured intensity approximately satisfies [173]

$$I_d(x_r, y, \theta) = I_0(x_r, y, \theta)\{A^2(x_r, y, \theta) - \frac{\lambda R_2}{2\pi M}\nabla^2_{x_r,y}[A^2(x_r, y, \theta)\phi(x_r, y, \theta)]\}, \tag{6.4}$$

where the magnification factor $M = (R_1 + R_2)/R_1$ and $\nabla^2_{x_r,y}$ is the 2D Laplacian operator acting on the (x_r, y) plane. Under certain approximations, we define a data function g as [26]

$$\begin{aligned} g(x_r, y, \theta) &= -\log\{\frac{I_d(x_r, y, \theta)}{I_0(x_r, y, \theta)}\} \\ &\approx A(x_r, y, \theta) + \frac{\lambda R_2}{2\pi}\nabla^2_{x_r,y}\phi(x_r, y, \theta) \end{aligned} \tag{6.5}$$

Eq. (6.5) shows that the measured data should contain edge-enhancement at the boundaries between different projected refractive properties. It also reveals that the diffraction phenomenon is easier to observe with increasing propagation distance R_2.

Under the paraxial approximation (i.e., a small cone angle), it has been demonstrated that the application of a 3D reconstruction operator $\mathcal{R}^{-1}$ (e.g. FDK algorithm) to this data function yields the object function [26]

$$\begin{aligned} f(\mathbf{r}) &= \mathcal{R}^{-1}\{g\} \\ &= 2k\beta(\mathbf{r}) + \frac{R_2}{M}\nabla^2_{xyz}\delta(\mathbf{r}) \end{aligned} \tag{6.6}$$

where ∇^2_{xyz} denotes a 3D Laplacian operator. Eq. (6.6) is called the object function for boundary-enhanced tomography. It contains mixed contrast regarding β and δ and mathematically explains why in-line XPC tomography enables the reconstructed object to retain the features of edge-enhancement that are observed in the measured projections.

6.2.2 OS-SART-FISTA-TV (OSSF-TV) iterative algorithm

In development of an iterative tomosynthesis algorithm, we employ a discrete imaging model. A vector $\mathbf{g}_{M\times 1}$ is used to represent the continuous data function (Eq. 6.5) in a discrete form. A vector $\mathbf{f}_{N\times 1}$ is used to represent the 3D discrete object using voxels. The size of N corresponds to the number of voxels that make up the reconstruction region. The relationship between the acquired data $\mathbf{g}_{M\times 1}$ and the discrete object $\mathbf{f}_{N\times 1}$ can be formed as

$$\mathbf{g} = \mathbf{H}\mathbf{f} \tag{6.7}$$

where $\mathbf{H}$ is an $M \times N$ system matrix that can be interpreted as an operator representing a cone-beam projection transformation. In this work, for the sake of simplicity, the system matrix $\mathbf{H}$ only represents the discrete ray-tracing projector in tomosynthesis.

A wide variety of iterative image reconstruction algorithms can be employed for determining estimates of $\mathbf{f}$ [152, 183]. In this work, we seek solutions of a total-variation (TV) regularized least square optimization problem [151, 177]

$$\hat{\mathbf{f}} = \arg\min \|\mathbf{g} - \mathbf{H}\mathbf{f}\|_2^2 + 2\zeta\|\mathbf{f}\|_{TV} \tag{6.8}$$

where ζ is a regularization parameter whose value is empirically chosen to be 0.5.

A modified version of fast iterative shrinkage/thresholding algorithm (FISTA) was employed to solve Eq. (6.8). The employed OSSF-TV algorithm has been proposed and discussed in Chapter 5.

6.2.3 Fourier analysis of XPC tomosynthesis

The well-known Fourier slice theorem states that a projection along a direction θ in space (e.g. x, y, z) corresponds to a plane along θ in the frequency domain (i.e. k_x, k_y, k_z). When projection views are acquired along a limited scan range, a wedge in the Fourier domain is covered where the opening angle of the wedge is equal to the arc of the tomosynthesis scan. [136] Figure 6.2 depicts this relationship by showing the (k_x, k_z) plane with a shaded region corresponding to frequency components of measured data from a tomosynthesis scan. The figure explains why tomosynthesis produces limited z resolution: the acquired information along the k_z direction in region A is limited due to the angular range of the tomosynthesis scan, especially at low frequencies near the origin. It also explains why small objects are better resolved along the z direction than large objects as there resides a significant amount of high frequency information (corresponding to larger values of k_z) in region B of the measured data.

A similar analysis can be applied to interpreting frequency domain characteristics of XPC tomosynthesis signals. Due to the action of the Laplacian operator ∇^2 in Eq. (6.5), the high frequency components of the second term are significantly amplified, and the corresponding region in Fourier domain along k_z direction is thus enhanced. Based on the previous analysis, the phase-contrast-induced fringes associated with the $\nabla^2\phi$ term should have better z resolution because they are able to cover a wider range along k_z direction. This idea is validated in the following simulation studies.

6.3 Descriptions of numerical and experimental studies

6.3.1 Computer-Simulation Studies Descriptions

In this section, we describe the way that we conducted computer simulations to evaluate reconstructed tomosynthesis in-plane images and depth resolution.

Phantom design: Figure 6.3 shows the spherical phantom we employed to investigate the depth resolution properties of XPC tomosynthesis. Eight spheres were placed in a row in the x-direction with their z positions slightly offset from one another. The spherical volumes were assigned realistic tissue properties (i.e. breast tissue, adipose and tumor), whose refractive index values were calculated [178] based on the element composition[1] and atomic scattering factors[2]. The diameters of the spheres ranged between 80 μm to 160 μm, and the diameter of the entire phantom is around 4mm. To simulate a realistic model of tissue boundaries and to avoid difficulties in applying the Laplacian operator in Eq. 6.6, we applied a 3D Gaussian blurring kernel to smooth each sphere, making sure that the boundaries between different tissues are differentiable.

Scanning geometries: The geometry of the simulated tomosynthesis imaging system is illustrated in Fig 6.4. The source and the flat-panel detector simultaneously rotate around the isocenter with a specified angular step (2°) and scan range ($\pm 20^\circ$). The source-to-isocenter distance R_1 and the isocenter-to-detector distance R_2 were both set to be 50cm corresponding to a geometric magnification of two. The measurement data is a set of 1024×1024 projections with a pixel size of 8 μm. We included realistic physical blurring factors (e.g. the finite source spot size, and the limited detector resolving power) by applying an additional 2D Gaussian blurring kernel (FWHM=40μm) to the simulated projections.

Chromatic coherence: In order to simulate the performance of a realistic benchtop x-ray tube, we considered a polychromatic source with a wide bandwidth ranging from 5-55keV (Fig 6.5). The spectrum was obtained from on-line software developed by Siemens assuming

[1] http://physics.nist.gov/PhysRefData/XrayMassCoef/tab2.html
[2] http://physics.nist.gov/PhysRefData/FFast/html/form.html

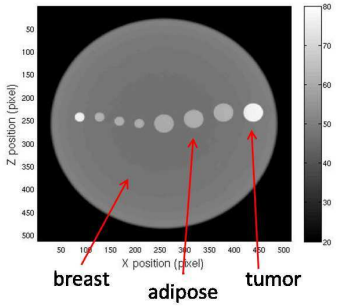

Figure 6.3: The numerical phantom we employed to investigate XPC tomosynthesis is shown (top view). Diameters of internal spheres range from $80\mu m$ to $160\mu m$.

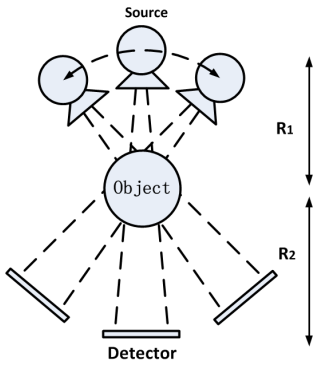

Figure 6.4: This figure illustrates the tomosynthesis scanning configuration used in the study. The detector and source rotate about the fixed phantom covering a limited angular range.

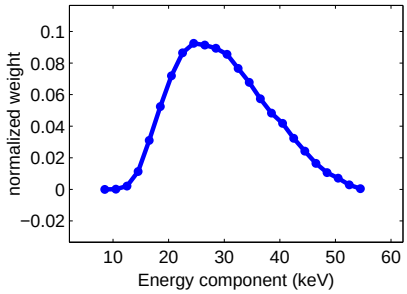

Figure 6.5: The polychromatic spectrum used as input in the tomosynthesis simulations is shown. The y-axis gives the normalized weight for each energy bin.

a solid tungsten anode.[3] The simulated polychromatic projections are calculated as the weighted sum of the intensity associated with each energy component of the spectrum.

In the numerical simulation studies, we analytically generated two sets of projection data based on the conventional absorption-based Radon transform and the XPC imaging model described in Section 6.2.1. The effects of physical blur and polychromaticity were taken into consideration as specified above. In addition, 1% (with respect to the local pixel value) uncorrelated Gaussian noise was added to the projection data. We then employed the proposed advanced iterative algorithm for tomosynthesis reconstruction. The result for each dataset is a 512×512×512 matrix with a voxel size of 8μm. As described in the next section, we analyzed reconstructed images from these conventional and XPC tomosynthesis datasets to compare and contrast their respective z resolution properties.

6.3.2 Experimental Studies Descriptions

Imaging system: The XPC imaging system was supported on an optical table and utilized high-precision rails to allow the sample and the detector to be positioned at distances from

[3]https://w9.siemens.com/cms/oemproducts/Home/X-rayToolbox/spektrum/Pages/radIn.aspx

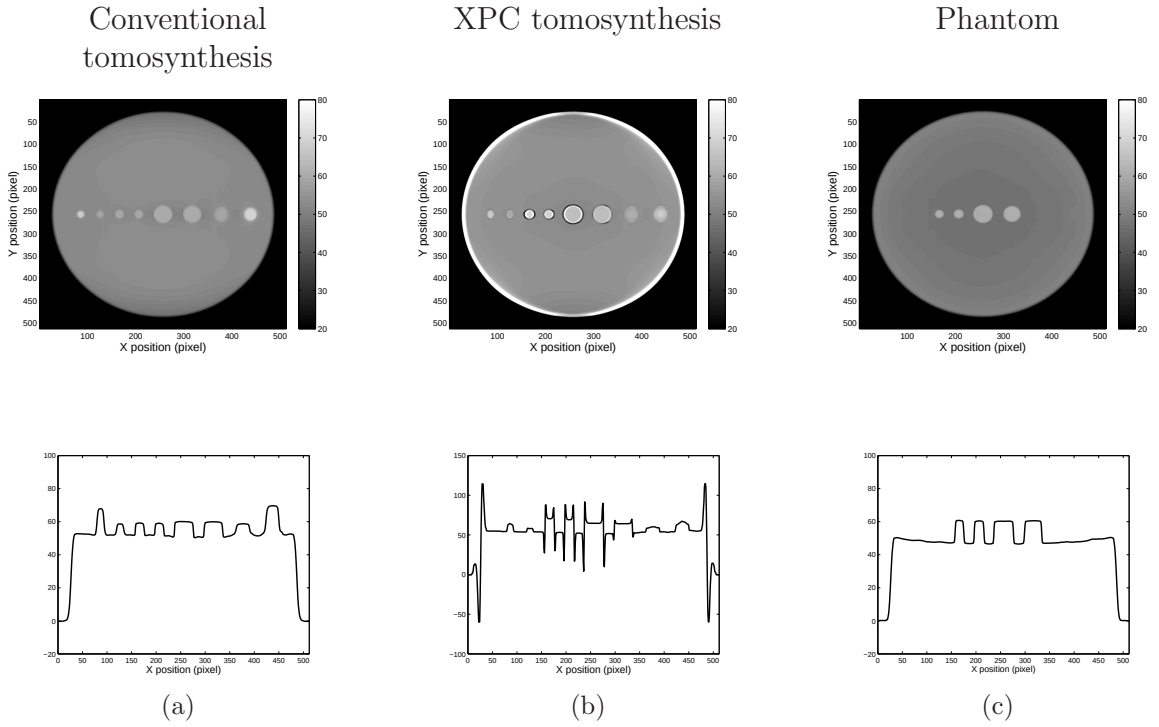

Figure 6.6: Comparison of reconstructed in-plane images (top row) and associated profiles (bottom row). (a)The line profiles from conventional tomosynthesis result show similar signals from all internal spheres. (b) The XPC tomosynthesis result reveals edge-enhancement for some of the internal spheres. (c) The true in-plane phantom structure shows that only the edge-enhanced spheres in (b) are actually located in that plane.

the x-ray source ranging from 20 cm to 2 m. X-ray generation was provided by a Kevex PSX10-65W microfocus source (Thermosher) which has a variable spot size ranging from 7 to 100 μm and can operate at tube voltages between 45 and 130 kV. For this x-ray source, the beam current setting determines the spot size for a given tube voltage setting with larger currents corresponding to larger spot sizes. The x-ray camera is a super-cooled QuadRO: 4096 (Princeton Instruments) which uses a 4096 $\times$ 4096 pixelated Si-based CCD detector with 15 μm pixel pitch, 33 micron effective FWHM resolution, and 36 cm^2 detection area. The CCD is illuminated by a Gd2O2S:Tb phosphor screen optimized for 17.5 keV x-rays which is coupled directly to the CCD via optical bers with a 1:1 taper ratio. During image acquisition, samples were placed on computer-controlled X,Y linear translation stages (Thorlabs LTS150).

6.4 Computer simulation results

6.4.1 In-plane image evaluation

In Fig. 6.6, the top row shows the reconstructed in-plane images (x-y plane) at the central depth position ($z = 256$); the associated profiles are shown in the bottom row. For the conventional tomosynthesis results (Fig.6.6-a), all of the spheres appeared in this plane and it is not possible to determine which spheres are actually located at this depth position. For XPC tomosynthesis (Fig.6.6-b), again all spheres are present in the reconstructed images, however, four of them exhibit fringes. Based on the previous observation, only these four spheres should be in-plane structures, and the other spheres are contaminations from out-of-plane. The corresponding slice of the true phantom (Fig.6.6-c) verifies this interpretation and demonstrates that only the structures with fringes are truly located in this plane and the others actually do not exist in this plane.

6.4.2 In-depth image evaluation

The reconstructed in-depth images (x-z plane) from conventional tomosynthesis and XPC tomosynthesis are shown in Fig. 6.7. A zoomed-in area for a central sphere (highlighted as dotted blue rectangular region) is also displayed. For conventional tomosynthesis (Fig. 6.7-a,b), the spatial distribution of the reconstructed attenuation coefficient is strongly blurred along the z direction. For the XPC tomosynthesis case (Fig. 6.7-c,d) the reconstructed attenuation coefficient is also blurred, however the fringes at boundaries exhibit less blurring and are contained in a z-axis range near to the center of the sphere. This indicates that the edge-enhanced features in XPC tomosynthesis can possibly provide improved depth position determination of reconstructed structures compared to that from conventional tomosynthesis.

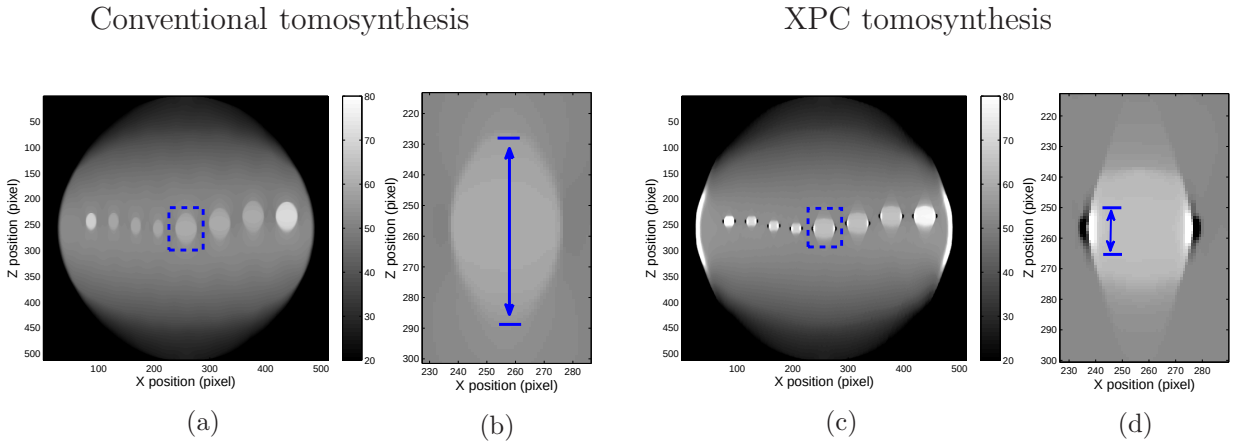

Figure 6.7: The reconstructed in-depth images are given for conventional (panel a) and XPC (panel c) tomosynthesis scans of the phantom shown in Fig 6.3. The dotted regions in (a) and (c) are shown with a close-up view in panels (b) and (d), respectively.The arrows indicate the extent of blur from image features for each case.

6.5 Experimental studies

6.5.1 In-plane image evaluation

We acquired extracted mouse lung using a benchtop x-ray imaging system in our lab. The tomosynthesis images reconstructed from the experimental data are shown in Fig. 6.8. Both FDK and iterative algorithm were employed for comparison purpose and the full-view CT result was taken as the reference. Three different depth positions were investigated. Fig. 6.9 shows the corresonding SSIM map for each case. We see iterative algorithm generally provides much more accurate structure than FDK in terms of in-plane image evaluation.

6.5.2 Z-resolution property of XPC tomosynthesis

An experimental study was also conducted to demonstrate the Z-resolution property of XPC tomosynthesis. We imaged extracted mouse lung and two branch airways were specified in the study. For XPC tomosynthesis, the projections were acquired with a long propagation distance $R_2 = 74$cm; for absorption-based tomosyntesis, we set the propagation distance

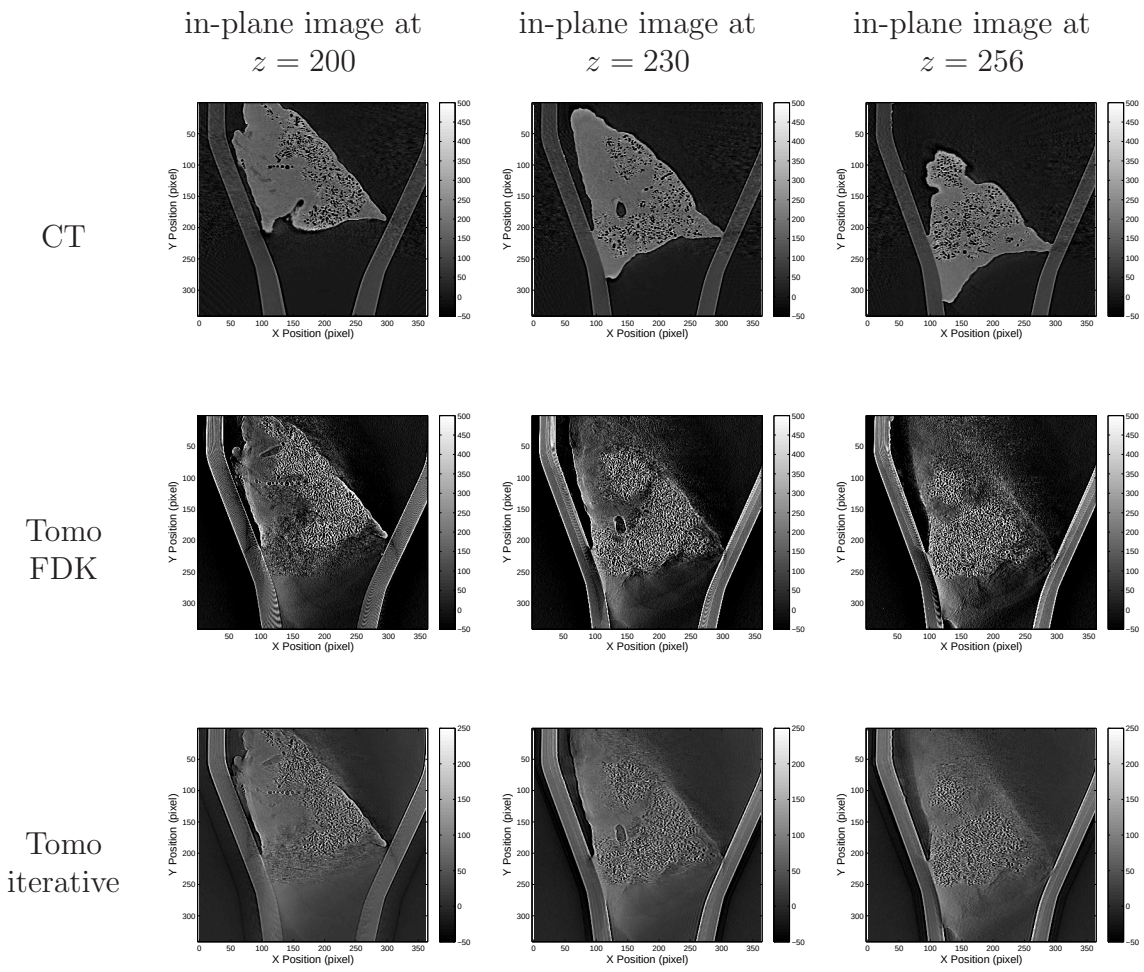

Figure 6.8: Reconstruction for experimental data: extracted mouse lung. CT reconstruction used 200 projections with the angular step of 1 degree; tomosynthesis reconstruction used 40 projections with the angular step of 1 degree. Voxel size: 28 μm

R_2 = 13cm only. Fig. 6.10 compares the reconstructed in-planes images between the two types of tomosynthesis in terms of depth resolution. We take the CT result as the reference. In the top row, the left branch airway was real at this position but the right branch airway was actually false structure brought by tomosynthesis. As expected, XPC tomosynthesis produced significant fringes at the left airway boudaries (shown in red line) but no edge enhancement observed for the right airway (shown in blue line); while conventional tomosynthesis was not able to provide any evidence to tell the structures true or false. The

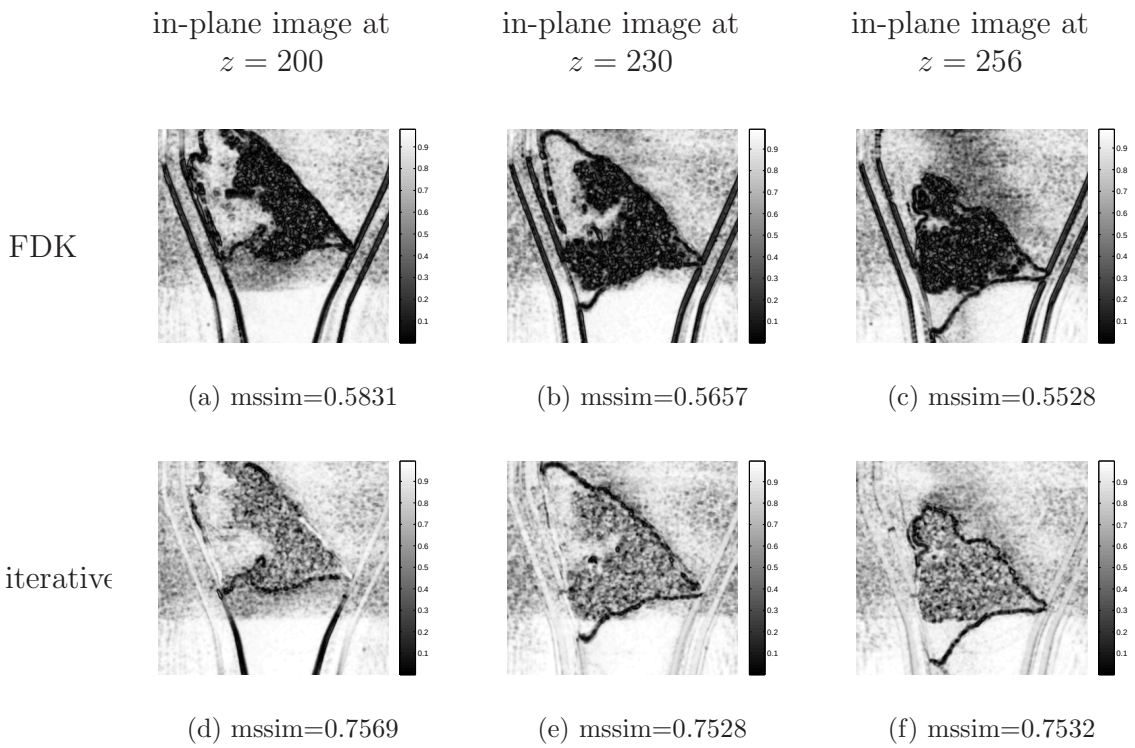

(a) mssim=0.5831 (b) mssim=0.5657 (c) mssim=0.5528

(d) mssim=0.7569 (e) mssim=0.7528 (f) mssim=0.7532

Figure 6.9: SSIM map for the reconstructed tomosynthesis images.

same condition occurred for the another depth position (shown in the bottom row), where only the right brach was real. Again, XPC tomosynthesis was able to take advantage of the fringes to judge, but conventional tomosynthesis failed to do so.

6.6 Conclusion and discussion

In this study [68], we have implemented an advanced iterative algorithm and investigated the depth resolution properties of XPC tomosynthesis. We observed that XPC tomosynthesis has better z resolution compared with conventional absorption-based tomosynthesis. More specifically, the simulation results show that in-plane structures display strong boundary-enhancement while out-of-plane structures do not. This effect can faciliate the identification of in-plane structures. Future studies will include a quantitative investigation based on

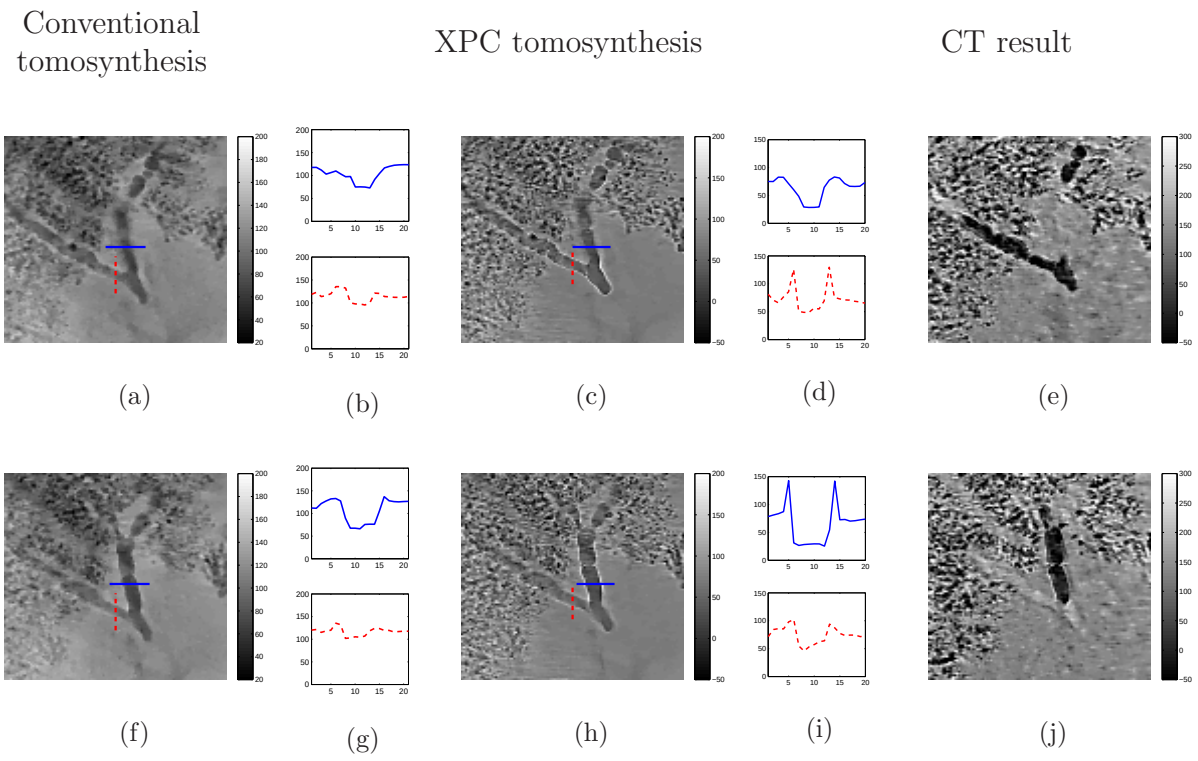

Figure 6.10: Experimental studies: comparison of the reconstructed in-planes images between the two types of tomosynthesis in terms of depth resolution. Two branch airways were specified and profiles are ploted to show the presence of edge enhancment. CT reconstruction used 100 projections with the angular step of 2 degrees; tomosynthesis reconstruction used 20 projections with the angular step of 3 degrees. Voxel size: 28 μm

simulated and experimental data to characterize the peformance of XPC tomosynthesis in identifying and locating features.

Chapter 7

Summary

In this dissertation, we have reviewed five different X-ray based imaging technologies, including differential phase-contrast tomography (DPCT), grating-based phase-contrast tomography (GB-PCT), spectral-CT (K-edge imaging), cone-beam computed tomography (CBCT) and in-line X-ray phase contrast (XPC) tomosynthesis. For each imaging modality, we proposed new approaches, strategies and/or fast convergent iterative algorithms to mitigate one or more specific problems, related to the issues of dose, long data-acquisition time, or image quality that prevent them being effectively or efficiently employed in clinical applications. To investigate all these proposed novel strategies and new algorithms in these different imaging modalities, we conduct computer simulation studies and/or real experimental data studies.

7.1 Differential phase-contrast imaging

We have analyzed the numerical and statistical properties of two classes of discrete imaging models that form the basis for iterative image reconstruction in DPCT. The models differ in the choice of expansion functions that were utilized to discretize the sought-after object function. The models based on Kaiser-Bessel window functions ("blobs") were demonstrated to produced images that possess more favorable variance-resolution trade-offs than images reconstructed by use of pixel-based imaging models. This observation was consistent with the results of an SVD analysis of the system matrices, which demonstrated that the blob-based system matrices can yield more stable reconstruction problems than do pixel-based ones.

A reconstruction algorithm that seeks solutions of a constrained TV minimization optimization program was employed with a blob-based imaging model for few-view image reconstruction. By use of few-view experimental data, it was demonstrated that this algorithm can produce images with significantly weaker artifacts and lower noise levels than the FBP algorithm that has been utilized the majority of previously published studies. To our knowledge, this was the first published application of an iterative reconstruction method in X-ray DPCT for reconstruction of a biological specimen. We expect that the findings of our study will benefit the continued development of DPCT imaging systems by permitting reduction of data-acquisition times and radiation doses. Future research efforts will be required to identify blob parameters that are optimal for specific imaging tasks.

7.2 Grating-based phase-contrast imaging

For the first time, we fully exploited the 2nd order statistical properties of the measurement data in GB XPCT to suppress image noise by formulating reconstruction methods in a MC framework. The computer simulation studies have confirmed our expectation that the MC approach that exploits inter-sinogram correlations can achieve lower noise-levels and better image quality for the absorption and dark-field channels. This observation and conclusion can be explained by the estimated full MC covariance matrix that implies that the absorption and dark-field channels are correlated and the phase channel is statistically independent from the other two channels. These reconstruction methods will enable imaging at reduced doses and imaging times and will accelerate the translation of this imaging technology.

7.3 Spectral-CT (K-edge imaging)

We have proposed and investigated PWLS-TV and PWLS-TV-ℓ_l methods for reconstructing distributions of K-edge materials from reduced-view data in spectral CT. It was demonstrated that, by incorporating the variance information of the decomposed sinograms in the reconstruction method, the PWLS-TV method possessed a noise-to-spatial-resolution trade-off that was superior to a PLS-TV method that ignored the variance information. It

was also demonstrated that, by promoting object sparsity in a wavelet transfrom domain, the PWLS-TV-ℓ_l method could improve the fidelity of small structures and remove isolated noises from images reconstructed from reduced-view datasets. This can be particularly useful for preclinical *in-vivo* applications of K-edge imaging, which are currently limited by long scan-times. It is worthwhile to mention that in this study, statistical correlations between decomposed sinograms were not exploited. However, this allows to reconstruct K-edge images individualy, which minimizes the computational burden and yields short computation times. The incorporation of the full covariance matrix in the reconstruction process can potentially reduce noise levels further but presents computationally challenges [135] that are a topic of current investigation.

7.4 Cone-beam computed tomography

The FISTA is a state-of-the-art optimization algorithm that possesses a secord-order convergence rate and is suitable for minimizing PLS cost functions that contain non-smooth penalties. In this work, accelerated variants of the FISTA were proposed and investigated for CBCT image reconstruction. Algorithm acceleration was achieved by replacing the gradient-descent step in the standard FISTAs by an OS-SART subproblem. The proposed OSSF-TV and OSSF-TV-ℓ_1 algorithms solved PLS image reconstruction problems that utilized a TV penalty and the sum of a TV penalty and a wavelet-sparsified ℓ_1 norm penalty, respectively. However, the proposed approach to accelerating the FISTA can be applied readily to solve PLS reconstruction problems that utlize other sparsity-promoting penalty forms. By use of computer-simulated CBCT data, it was verified that the OSSF-TV and OSSF-TV-ℓ_1 algorithms possessed significantly greater convergence rates than the corresponding standard FISTAs. The rapid convergence properties of the algorithms were verified further by use of clincal CBCT data.

A reconstruction algorithm that possesses a rapid convergent rate can potentially produce a diagnostically useful image in fewer iterations than an algorithm that possesses a slower convergence rate. However, a rapid convergence rate does not necessarily translate into shortened reconstruction times. This depends on how efficiently each iteration can be computed.

In order to reduce image reconstruction times in practice, we developed efficient GPU implementations of the proposed algorithms that utlize either a single or multiple GPUs. When multiple GPUs are employed, we demonstrated that the reduction in reconstruction time over the single GPU implemenation is approximately linear with the number of GPUs employed. The rapid convergence rates of the extremely simple structured algorithms coupled with efficient GPU implementations may make them suitable for certain timie-sensitive clinical applications.

7.5 In-line phase-contrast tomosynthesis

We have implemented an advanced iterative algorithm and investigated the depth resolution properties of XPC tomosynthesis. We find XPC tomosynthesis has better z resolution compared with conventional absorption-based tomosynthesis. More specifically, the simulation results show that in-plane structures display strong boundary-enhancement while out-of-plane structures do not. This effect can faciliate the identification of in-plane structures. Future studies will include a quantitative investigation based on simulated and experimental data to characterize the peformance of XPC tomosynthesis in identifying and locating features.

Appendix A

Explicit construction of the pixel-based system matrices

Below we describe how the matrices $\mathbf{H}^{pixel}$ employed in our numerical studies were constructed by use of Eq. (2.15). Specifically, because $\mathbf{H}^{R}$ is defined by Eq. (2.10) with the elements provided in reference [148], we need to specify the explicit forms of discrete derivative operator $\mathbf{H}^{D}$ for the three kernel functions $\mathbf{W}(x_r, d)$ employed.

A general form of the matrix $\mathbf{H}^{D}$ can be expressed as follows

$$\mathbf{H^D} = \begin{pmatrix} \mathbf{H}^{11} & 0 & 0 & \cdots & \cdots & 0 \\ 0 & \mathbf{H}^{22} & 0 & \cdots & \cdots & 0 \\ 0 & 0 & \ddots & \cdots & \cdots & 0 \\ \vdots & & \cdots & \mathbf{H}^{tt} & \vdots & 0 \\ \vdots & & \cdots & & \ddots & 0 \\ 0 & 0 & \cdots & 0 & 0 & \mathbf{H}^{TT} \end{pmatrix},$$

where $\mathbf{H}^{tt}(t = 1, 2, \cdots, T)$ is a $S \times S$ matrix, T is the total number of projection views and S is the number of sampled projection data at each view. Explicit forms of $\mathbf{H}^{tt}$ are determined by different interpolation kernels $\mathbf{W}(x_r, h)$. Three types of $\mathbf{H}^{tt}$ corresponding to three different kernels $\mathbf{W}(x_r, h)$ adopted in the paper are provided as follows:

Linear interpolation kernel

$$\mathbf{W}_1(d,h) = n_d \begin{cases} 1-s & 0 \le s < 1, s = \frac{|d|}{h}, \\ 0 & s \ge 1, \end{cases}$$

where n_d is a normalization constant which is determined by the dimensionality and the smoothing length h. The value of h was set to 2 times the projection sampling interval, and n_d is equal to $\frac{1}{h}$. The explicit form of $\mathbf{H}^{tt}$ corresponding to use of $\mathbf{W}_1(x_r, d)$ can be expressed as

$$\mathbf{H}^{tt} = \begin{pmatrix} \cdots & \cdots & \text{boundary} & \text{condition} & \cdots & \cdots \\ -1/2 & 0 & 1/2 & 0 & 0 & \cdots \\ 0 & -1/2 & 0 & 1/2 & 0 & \cdots \\ \cdots & \ddots & \ddots & \cdots & \ddots & \vdots \\ \cdots & \cdots & 0 & -1/2 & 0 & 1/2 \\ \cdots & \cdots & \text{boundary} & \text{condition} & \cdots & \cdots \end{pmatrix}_{S \times S},$$

where the the boundary condition elements are appropriately defined. In our studies, the projection data were not truncated and the object was embedded in uniform background medium. In this case, the boundary condition elements were set to zero.

Quadratic spline

$$\mathbf{W}_2(d,h) = n_d \begin{cases} \frac{3}{4} - s^2 & 0 \le s < \frac{1}{2}, s = \frac{|d|}{h}, \\ \frac{9}{8} - \frac{3}{2}s + \frac{s^2}{2} & \frac{1}{2} \le s < \frac{3}{2}, \\ 0 & s \ge \frac{3}{2}, \end{cases}$$

where h was set to 2 times the projection sampling interval, and n_d is equal to $\frac{1}{h}$. The explicit form of $\mathbf{H}^{tt}$ corresponding to use of $\mathbf{W}_2(x_r, d)$ can be expressed as

$$\mathbf{H}^{tt} = \begin{pmatrix} \cdots & \cdots & \cdots & \text{boundary} & \text{condition} & \cdots & \cdots & \cdots \\ -1/8 & -1/4 & 0 & 1/4 & 1/8 & 0 & \cdots & \cdots \\ 0 & -1/8 & -1/4 & 0 & 1/4 & 1/8 & 0 & \cdots \\ \cdots & \ddots & \ddots & \ddots & \ddots & \ddots & \vdots & 0 \\ \vdots & \cdots & 0 & -1/8 & -1/4 & 0 & 1/4 & 1/8 \\ \cdots & \cdots & \cdots & \text{boundary} & \text{condition} & \cdots & \cdots & \cdots \end{pmatrix}_{S \times S}.$$

Cubic spline

$$\mathbf{W}_3(d, h) = n_d \begin{cases} \frac{2}{3} - s^2 + \frac{s^3}{2} & 0 \le s < 1, s = \frac{|d|}{h}, \\ \frac{4}{3} - 2s + s^2 - \frac{s^3}{6} & 1 \le s < 2, \\ 0 & s \ge 2, \end{cases}$$

where h was set to 2 times the sampling interval with linear interpolation case, and n_d is equal to $\frac{1}{h}$. The explicit form of $\mathbf{H}^{tt}$ corresponding to use of $\mathbf{W}_3(x_r, d)$ can be expressed as

$$\mathbf{H}^{tt} = \begin{pmatrix} \cdots & \cdots & \cdots & \cdots & \text{boundary} & \text{condition} & \cdots & \cdots & \cdots & \cdots \\ -1/32 & -1/8 & -5/32 & 0 & 5/32 & 1/8 & 1/32 & 0 & \cdots & \cdots \\ 0 & -1/32 & -1/8 & -5/32 & 0 & 5/32 & 1/8 & 1/32 & 0 & \cdots \\ \vdots & \ddots & \ddots & \ddots & \ddots & \ddots & \ddots & \ddots & \cdots & \vdots \\ 0 & \cdots & 0 & -1/32 & -1/8 & -5/32 & 0 & 5/32 & 1/8 & 1/32 \\ \cdots & \cdots & \cdots & \cdots & \text{boundary} & \text{condition} & \cdots & \cdots & \cdots & \cdots \end{pmatrix}_{S \times S}.$$

Appendix B

The derivation of Eq.(2.18) in Sec. 2.3.2

Let $\xi \equiv x_r - x_n \cos\theta - y_n \sin\theta$. As demonstrated by Lewitt [96], The 2D Radon transform of one window function is given by

$$\mathbf{R}\phi_n^{blob}(\mathbf{r}_2; m, a, \alpha) = \frac{a}{I_m(\alpha)}\left(\frac{2\pi}{\alpha}\right)^{1/2}\left[\sqrt{1-(\xi/a)^2}\right]^{m+1/2} I_{m+1/2}\left(\alpha\sqrt{1-(\xi/a)^2}\right), \quad \text{(B.1)}$$

for $|\xi| \leq a$ and zero otherwise. The gradient of the modified bessel function has the following relationship as [1]

$$\frac{d}{dz}\{z^{\pm m} I_m(z)\} = z^{\pm m} I_{m\mp 1}(z), \quad \text{(B.2)}$$

where z is the distance to the center of the blob and m is a real number. Let $z = \alpha\sqrt{1-(\xi/a)^2}$. Note that Eqn. (B.1) can be re-expressed as

$$\mathbf{R}\phi_n^{blob}(\mathbf{r}_2; m, a, \alpha) = \frac{a}{I_m(\alpha)}\left(\frac{2\pi}{\alpha}\right)^{1/2}\left(\frac{1}{\alpha}\right)^{m+1/2} z^{m+1/2} I_{m+1/2}(z). \quad \text{(B.3)}$$

By use of Eq. (B.2) and Eq. (B.3), along with the chain rule, it can be verified readily that

$$\begin{aligned}
\frac{\partial(\mathbf{R}\phi_n^{blob}(m,a,\alpha,r))}{\partial x_r} &= \frac{\partial(\mathbf{R}\phi_n^{blob}(m,a,\alpha,r))}{\partial z}\frac{\partial z}{\partial \xi}\frac{\partial \xi}{\partial x_r} \\
&= \frac{a}{I_m[\alpha]}\left(\frac{2\pi}{\alpha}\right)^{1/2}\left(\frac{1}{\alpha}\right)^{m+1/2} z^{m+1/2} I_{m-1/2}(z) \times \left(\frac{\alpha}{a}\right)^2\left(-\frac{\xi}{z}\right) \\
&= -\frac{(2\pi\alpha)^{1/2}}{I_m(\alpha)}\frac{\xi}{a}\left(\sqrt{1-(\xi/a)^2}\right)^{m-1/2} I_{m-1/2}\left(\alpha\sqrt{1-(\xi/a)^2}\right). \quad \text{(B.4)}
\end{aligned}$$

Appendix C

Desription of the FGP algorithm for the 3D case in Sec. 5.2.3

Below, the 3D FGP algorithm for solving the proximal problem contained in the FISTA is described. Without loss of generality, we assume that $g_{tv}(\mathbf{u}) = c_1\lambda_{tv}\|\mathbf{u}\|_{TV}$, where c_1 is a positive constant. Therefore,

$$prox_{1/L}(g_{tv})(\mathbf{x}_g) = prox_{1/L}(g_{tv})(\mathbf{e}_k - \frac{1}{L}\nabla d(\mathbf{e}_k)) := \arg\min_{\mathbf{u}} \left\{c_1\lambda_{tv}\|\mathbf{u}\|_{TV} + \frac{L}{2}\|\mathbf{u} - \mathbf{x}_g\|^2\right\}, \tag{C.1}$$

which is equivalent to the minimization problem

$$\hat{\mathbf{u}} := \arg\min_{\mathbf{u}} \left\{\|\mathbf{u} - \mathbf{x}_g\|^2 + 2\alpha\|\mathbf{u}\|_{TV}\right\}, \tag{C.2}$$

where $\alpha = c_1\lambda_{tv}/L$. It has been demonstrated [14] that the FGP method can efficiently solve the above problem in 2D case. Algorithm 3 describes the extension of the 2D FGP algorithm to 3D, for use with CBCT image reconstruction.

The relevant operators are explicitly defined as follows:

- The linear operator $\mathcal{L} : \mathbb{R}^{(m-1)\times n\ \times l} \times \mathbb{R}^{m\times(n-1)\times l} \times \mathbb{R}^{m\times n\times(l-1)} \to \mathbb{R}^{m\times n\ \times l}$ is defined by the following expression

$$\mathcal{L}(\mathbf{r},\mathbf{s},\mathbf{t}))_{i,j,h} = [\mathbf{r}]_{i,j,h} - [\mathbf{r}]_{i-1,j,h} + [\mathbf{s}]_{i,j,h} - [\mathbf{s}]_{i,j-1,h} + [\mathbf{t}]_{i,j,h} - [\mathbf{t}]_{i,j,h-1},$$
$$i = 1,\cdots,m, \quad j = 1,\cdots,n, \quad h = 1,\cdots,l$$

Algorithm 3 FGP algorithm to solve the TV-proximal problem in Eq. (C.2)

Input: $\mathbf{x}_g$,
Output: $\hat{\mathbf{u}}$ – An optimal solution of Eq. (C.1) (up to a tolerance).
Step 0. Take $(\mathbf{r}^1, \mathbf{s}^1, \mathbf{t}^1) = (\mathbf{o}^0, \mathbf{p}^0, \mathbf{q}^0) = [\mathbf{0}_{(m-1)\times n\times l}, \mathbf{0}_{m\times(n-1)\times l}, \mathbf{0}_{m\times n\times(l-1)}]$
for $k \leftarrow 1, K$ **do**

$$(\mathbf{o}^k, \mathbf{p}^k, \mathbf{q}^k) = P_{\mathcal{P}}\Big[(\mathbf{r}^k, \mathbf{s}^k, \mathbf{t}^k) + \frac{1}{12\alpha}\mathcal{L}^T(P_C[\mathbf{x}_g - \alpha\mathcal{L}(\mathbf{r}^k, \mathbf{s}^k, \mathbf{t}^k)])\Big] \tag{C.3}$$

$$t_{k+1} = \frac{1+\sqrt{1+4t_k^2}}{2} \tag{C.4}$$

$$(\mathbf{r}^{k+1}, \mathbf{s}^{k+1}, \mathbf{t}^{k+1}) = (\mathbf{o}^k, \mathbf{p}^k, \mathbf{q}^k) + \Big(\frac{t_k - 1}{t_{k+1}}\Big)(\mathbf{o}^k - \mathbf{o}^{k-1}, \mathbf{p}^k - \mathbf{p}^{k-1}, \mathbf{q}^k - \mathbf{q}^{k-1}) \tag{C.5}$$

end for
Set $\mathbf{f}_K = P_C[\mathbf{x}_g - \alpha\mathcal{L}(\mathbf{o}^K, \mathbf{p}^K, \mathbf{q}^K)]$

where we assume that $[\mathbf{r}]_{0,j,h} = [\mathbf{r}]_{m,j,h} = [\mathbf{s}]_{i,0,h} = [\mathbf{s}]_{i,n,h} = [\mathbf{t}]_{i,j,0} = [\mathbf{t}]_{i,j,l} \equiv 0$,for every $i = 1, \cdots, m$ and $j = 1, \cdots, n$ and $h = 1, \cdots, l$. In our CBCT case, the values of m, n and l represent the dimensions of the 3D discrete object.

- P_C is an orthogonal projection operator onto the convex feasible set C. In our CBCT case, we consider the operator P_C is a positivity constraint:

$$P_C[\mathbf{x}] = \max\big\{\mathbf{0}, \mathbf{x}\big\},$$

where $\mathbf{x}$ is a arbitrary input matrix and max applies on the vector or matrix $\mathbf{x}$ in a element-wise way.

- The operator $\mathcal{L}^T$: $\mathbb{R}^{m\times n\times l} \to \mathbb{R}^{(m-1)\times n\times l} \times \mathbb{R}^{m\times(n-1)\times l} \times \mathbb{R}^{m\times n\times(l-1)}$, which is the adjoint of $\mathcal{L}$ is given by

$$\mathcal{L}^T(\mathbf{x}) = (\mathbf{r}, \mathbf{s}, \mathbf{t})$$

where $\mathbf{r} \in \mathbb{R}^{(m-1)\times n\times l}$, $\mathbf{s} \in \mathbb{R}^{m\times(n-1)\times l}$, and $\mathbf{t} \in \mathbb{R}^{m\times n\times(l-1)}$ are the matrices defined by

$$\begin{aligned}
[\mathbf{r}]_{i,j,h} &= [\mathbf{x}]_{i,j,h} - [\mathbf{x}]_{i+1,j,h}, \quad i = 1, \cdots, m-1, j = 1, \cdots, n, h = 1, \cdots, l \\
[\mathbf{s}]_{i,j,h} &= [\mathbf{x}]_{i,j,h} - [\mathbf{x}]_{i,j+1,h}, \quad i = 1, \cdots, m, j = 1, \cdots, n-1, h = 1, \cdots, l \\
[\mathbf{t}]_{i,j,h} &= [\mathbf{x}]_{i,j,h} - [\mathbf{x}]_{i,j,h+1}, \quad i = 1, \cdots, m, j = 1, \cdots, n, h = 1, \cdots, l-1.
\end{aligned}$$

- The operator $P_{\mathcal{P}}$: $\mathbb{R}^{(m-1)\times n\times l}\times\mathbb{R}^{m\times(n-1)\times l}\times\mathbb{R}^{m\times n\times(l-1)}\to\mathbb{R}^{(m-1)\times n\times l}\times\mathbb{R}^{m\times(n-1)\times l}\times\mathbb{R}^{m\times n\times(l-1)}$, which is a projection operator onto the set $\mathcal{P}$ such as

$$\mathcal{L}^T(\mathbf{r},\mathbf{s},\mathbf{t})=(\mathbf{o},\mathbf{p},\mathbf{q})$$

where $\mathbf{r},\mathbf{s},\mathbf{t}$ and $\mathbf{o},\mathbf{p},\mathbf{q}$ denote the input and output matrices respectively are the matrices defined by

$$[\mathbf{o}]_{i,j,h}=\frac{\mathbf{r}_{i,j,h}}{\max\{1,\sqrt{[\mathbf{r}]^2_{i,j,h}+[\mathbf{s}]^2_{i,j,h}+[\mathbf{t}]^2_{i,j,h}}\}},\quad i=1,\cdots,m-1,j=1,\cdots,n,h=1,\cdots,l$$

$$[\mathbf{p}]_{i,j,h}=\frac{\mathbf{s}_{i,j,h}}{\max\{1,\sqrt{[\mathbf{r}]^2_{i,j,h}+[\mathbf{s}]^2_{i,j,h}+[\mathbf{t}]^2_{i,j,h}}\}},\quad i=1,\cdots,m,j=1,\cdots,n-1,h=1,\cdots,l$$

$$[\mathbf{q}]_{i,j,h}=\frac{\mathbf{t}_{i,j,h}}{\max\{1,\sqrt{[\mathbf{r}]^2_{i,j,h}+[\mathbf{s}]^2_{i,j,h}+[\mathbf{t}]^2_{i,j,h}}\}},\quad i=1,\cdots,m,j=1,\cdots,n,h=1,\cdots,l-1,$$

where we define $[\mathbf{r}]_{m,j,h}=[\mathbf{s}]_{i,n,h}=[\mathbf{t}]_{i,j,l}\equiv 0$.

Appendix D

Description of FISTA-ℓ_1 algorithm for wavelet-ℓ_1 penalty in Sec. 5.2.4

Without loss of generality, consider that $g_{l1}(\mathbf{u}) = c_2\lambda_{l1}\|\Phi\mathbf{u}\|_1$, in which c_2 is a positive constant and Φ is a 3D discrete Daubechies wavelet transform operator. Accordingly, we can have

$$prox_{1/L}(g_{\ell 1})(\mathbf{x}_g) := \arg\min_{\mathbf{u}} \left\{c_2\lambda_{\ell 1}\|\Phi\mathbf{u}\|_1 + \frac{L}{2}\|\mathbf{u}-\mathbf{x}_g\|^2\right\}, \tag{D.1}$$

which is equivalent to the minimization poblem

$$\hat{\mathbf{u}} := \arg\min_{\mathbf{u}} \left\{\|\mathbf{u}-\mathbf{x}_g\|^2 + \beta\|\mathbf{\Phi u}\|_1\right\}, \tag{D.2}$$

where $\beta = 2c_2\lambda_{\ell 1}/L$. Since the Daubechies wavelets are orthogonal, $\Phi^T\Phi = \mathcal{I}$. Hence, Eq. (D.2) is equivalent to the following minimization problem:

$$\hat{\mathbf{u}} := \arg\min_{\mathbf{u}} \left\{\|\Phi\mathbf{u}-\Phi\mathbf{x}_g\|^2 + \beta\|\mathbf{\Phi u}\|_1\right\}, \tag{D.3}$$

or

$$\hat{\tilde{\mathbf{u}}} := \arg\min_{\tilde{\mathbf{u}}} \left\{\|\tilde{\mathbf{u}}-\tilde{\mathbf{x}}_g\|^2 + \beta\|\tilde{\mathbf{u}}\|_1\right\}, \tag{D.4}$$

where $\tilde{u}$ and $\tilde{\mathbf{x}}_g$ represent the wavelet coefficients of $\mathbf{u}$ and $\mathbf{x}_g$, respectively. It has been demonstrated [15, 42] that the iterative shrinkage thresholding algorithm (ISTA) can readily solve this problem by employing an operator

$$\hat{\tilde{\mathbf{u}}} = \mathcal{T}_\beta(\tilde{\mathbf{x}}_g),$$

where $\mathcal{T}_\alpha$ is defined as

$$\mathcal{T}_\beta(\tilde{\mathbf{x}}_g) = (\|\tilde{\mathbf{x}}_g\| - \beta)_+ \text{sgn}(\tilde{\mathbf{x}}_g),$$

where $(\cdot)_+$ returns the argument if it is positive and returns zero otherwise, and the function sgn returns the sign of $(\cdot)$. The ISTA requires only one computation of the discrete wavelet transform of $\mathbf{x}_g$ to obtain the wavelet coefficients $\tilde{\mathbf{x}}_g$, followed by application of a shrinkage-thresholding operator to get the solution. Both of these operations can be computed efficiently.

Appendix E

Hardware acceleration employing single and multiple GPUs in Sec. 5.3.2

Single- and multi-GPU implemenations of the OSSF-TV algorithm are described below. Although not presented, the implementations for the OSSF-TV-ℓ_1 algorithm are essential similar to those of the OSSF-TV algorithm.

E.1 Single GPU implementation of the OSSF-TV algorithm for CBCT

All implementation in this work were based on NVIDIA Tesla K20 GPUs, each of which has 2496 processing cores and 5GB of RAM. Figure E.1 describes the basic structure of the single-GPU implementation of the OSSF-TV algorithm.

Specific details are as follows:

- **Projection data $\mathbf{b}^{data}$**: The projection data $\mathbf{b}^{data}$ are transferred into the GPU global memory from the host memory. If the GPU global memory allows, the projection data should be transferred into GPUs at one time instead of multiple transfers.
- **OS-SART**
  - **Projection-correction step (One kernel function in GPU)**: For the vth subset, each thread distributed by the GPU is employed to compute one element

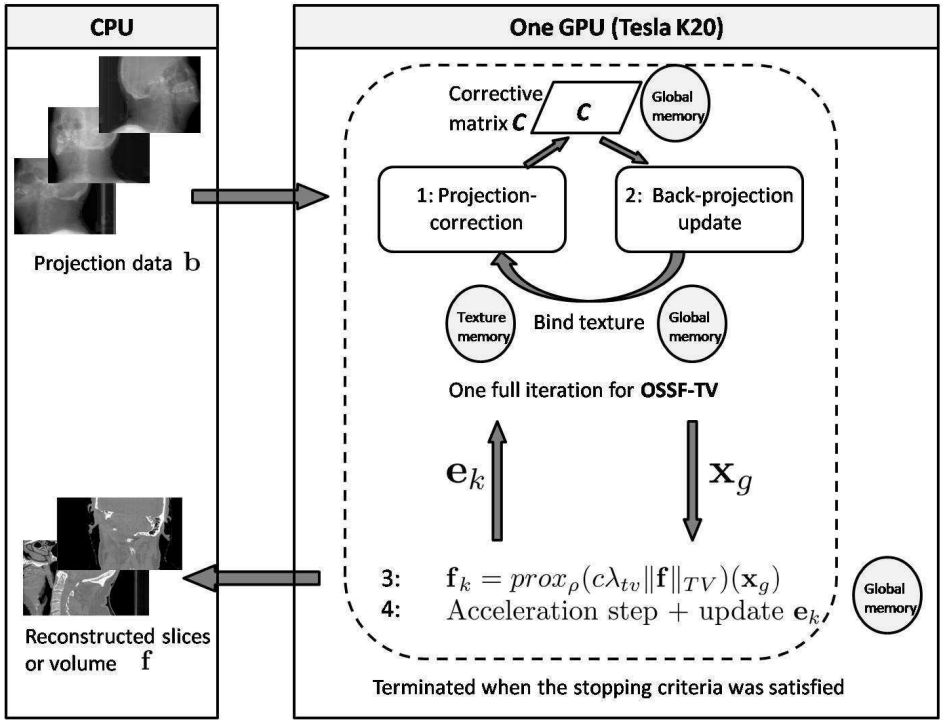

Figure E.1: A simple flowchart of the OSSF-TV algorithm with single GPU approach

of the corrective matrix $c_{i,v}$ according to the Eq.(5.21). In order to accelerate this step, the 3D discrete object matrix $\mathbf{f}$ was stored in texture memory. The correspondent values of $h_{ij,v}$ was calculated independently by use of a previous proposed method [81] in each thread. The calculated 2D corrective matrix $c_{i,v}$ for the vth subset was located in GPU global memory, which will be employed in the following backprojection-update step.

– **Backprojection-update step (One kernel function in GPU)**: For the vth projection data subset, each thread independently updates one specific voxel of the 3D volume $\mathbf{f}$ from the previous obtained 2D corrective matrix $c_{i,v}$ according to the Eq. (5.22). To update each element f_j independently, a key step is to find the indices of the ray that intersects the jth voxel. This can be accomplished by projecting the eight vertexes of the jth voxel onto the detector plane to find the ray indices range.

  For each subset, the object matrix $\mathbf{f}$ was updated once, which would be used in

next subset update. One full iteration of the **OS-SART** algorithm is performed before solving the TV-proximal problem by the FGP method.

- **TV-proximal problem (One kernel function in GPU):** As described previously, the four operators $\mathcal{L}$, P_C, $\mathcal{P}^P$, and $\mathcal{L}^T$ operate in a element-wise manner in Eq. (C.3). This indicates that each element of $(\mathbf{r}, \mathbf{s}, \mathbf{t})$ and $(\mathbf{o}, \mathbf{p}, \mathbf{q})$ can be updated independently by use a GPU thread. Accordingly, implemenations of Eqs. (C.3) (C.5) can efficiently exploit GPU parallelism because only simple and independent arithmetic operations are required by each thread that generally cause few memory conflicts.

  Note that the nine auxillary vectors $\mathbf{r}^k$, $\mathbf{s}^k$, $\mathbf{t}^k$, $\mathbf{o}^{k-1}$, $\mathbf{p}^{k-1}$, $\mathbf{q}^{k-1}$, $\mathbf{o}^k$, $\mathbf{p}^k$, and $\mathbf{q}^k$ need to be stored in the GPU memory as well. Each vector approximately had the same size with the 3D matrix $\mathbf{f}$. Fortunately, when each of these vectors has fewer than 512^3 elements, the NVIDIA K20 has enough global memory to store all of them simultaneouly. For vectors larger than 512^3, the memory bottleneck can be mitigated by the following multi-GPU scheme.

E.2 Multi-GPU implementation of the OSSF-TV algorithm for CBCT

To further reduce the computation time, a multi-GPU scheme is proposed in this section. We assume four NVIDIA K20s are employed and demonstrate some basic rules and possible arrangements. A flowchart is shown in Fig. E.2. The original 3D vector $\mathbf{f}$ is divided into four equal sub-volumes that are distributed among four GPUs ($id = 0, 1, 2, 3$) respectively. Details regarding the multi-GPU implemenation are as follows:

- **Projection data $\mathbf{b}^{data}$**: The projection data $\mathbf{b}^{data}$ are transfered to the global memories of the four GPUs.
- **OS-SART:** The projection-correction step is divided into two individual sub-steps:
  - **Projection step (One kernel function in GPUs):** Each thread launched by the id-th GPU (id=0,1,2,3) simultaneously computes one ray integral through the

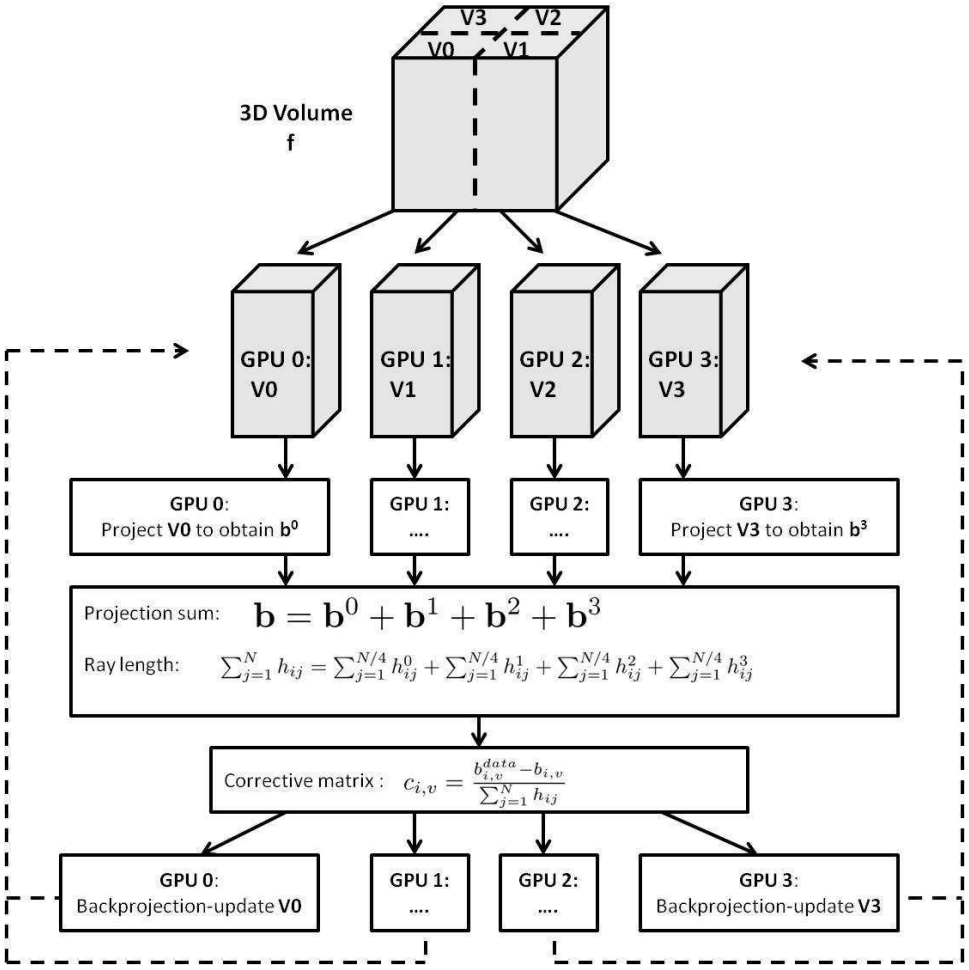

Figure E.2: One simple scheme of four GPUs implementation for OS-SART part in porposed OSSF-TV and/or OSSF-TV-ℓ_1 algorithms

id-th sub-volume as

$$b_{i,v}^{id} = \sum_{j=1}^{N/4} h_{ij,v}^{id} f_{j,v-1}^{id}, \quad \imath = 1, 2, \cdots, M/T; \ id = 0, 1, 2, 3,$$

$$rl_{i,v}^{id} = \sum_{j=1}^{N/4} h_{ij,v}^{id}, \qquad \imath = 1, 2, \cdots, M/T; \ id = 0, 1, 2, 3,$$

where the superscript id indicates the sub-volume, $h_{ij,v}^{id}$ represents the contribution from the jth voxel in the idth sub-volume to the ith ray, and $b_{i,v}^{id}$ represents the ith

ray integral through the idth sub-volume. The notation $f_j^{id,v-1}$ specifies the jth voxel value in the id-th sub-volume at the $(v-1)$-th update in one full OS-SART iteration, and $rl_{i,v}^{id}$ represents the length of the i-th ray that intersected the id-th sub-volume.

– **Correction step (One kernel in GPUs):** In order to calculate the 2D corrective matrix $c_{i,v}$, the ray integrals and ray lengths calculated from all sub-volumes are summed to obtain the values for the full volume as follows:

$$\begin{aligned} b_{i,v} &= b_{i,v}^0 + b_{i,v}^1 + b_{i,v}^2 + b_{i,v}^3, \\ rl_{i,v} &= rl_{i,v}^0 + rl_{i,v}^1 + rl_{i,v}^2 + rl_{i,v}^3, \quad i = 1, 2, \cdots, M/T; \end{aligned}$$

Therefore, the 2D corrective matrix $c_{i,v}$ is computed as

$$c_{i,v} = \frac{b_{i,v}^{data} - b_{i,v}}{rl_{i,v}}, \qquad \imath = 1, 2, \cdots, M/T.$$

Next, the $c_{i,v}$ are copied to the global memory of all GPUs to prepare the last backprojection-update step.

– **Backprojection-update step (One kernel in GPUs):** Similar rules and strategies described in the single GPU implementation are also applicable here. Each thread launched by the id-th GPU is employed to independently update one voxel in the id-th sub-volume as

$$f_{j,v}^{id,k} = f_{j,v-1}^{id,k} + \gamma \frac{\sum_{i \in \phi^{id}} (c_{i,v-1}) h_{ij,v}^{id}}{\sum_{i \in \phi^{id}} h_{ij,v}^{id}}, \quad j = 1, 2, \cdots, N/4;$$

The above equation was essential the same with the Eq. (5.22), but it was performed in each sub-volume by each corresponding GPU.

During each view-update circle, four GPUs are synchronized for the projection step since all four ray integrals $b_{i,v}^{id}$ are required in the corection step. Four sub-volumes are updated once in their respective GPUs for each subset. Similar to the single GPU case, a full iteration for the OS-SART algorithm is performed before solving the TV-proximal problem.

- **TV-proximal problem:** In the OS-SART computation, an intermediate solution $\mathbf{x_g}$ to minimization problem $d(\mathbf{f})$ was obtained and stored as four sub-volumes $\mathbf{x}_g^0$, $\mathbf{x}_g^1$, $\mathbf{x}_g^2$, $\mathbf{x}_g^3$ in four GPUs. Becuase of the element-wise property of four operators in Eq. (C.3), Algorithm 3 was independently executed for each sub-volume in each GPU concurrently. Except when the operators $\mathcal{L}$ and $\mathcal{L}^T$ act on elements of $(\mathbf{r}, \mathbf{s}, \mathbf{t})$ and $\mathbf{x}_g$ located at the boundaries between two sub-volumes, each GPU only needs to access its own memory. However, the number of such elements is small when compared to the number elements inside each sub-volume.

The computation time for the projection operation in the OS-SART step when four GPUs is employed is approximately one quarter of the time required by single GPU implemenation. This is because both the calculation time for ray integrals through one sub-volume in each thread and the number of nonzero ray integral threads in each GPU would be approximately one half of those in single GPU case. The computation time for the backprojection-update step with four GPUs would also be approximately one quarter of the time required by one single GPU, since each GPU only updated one sub-volume data, whose size was only one quarter of the original volume. Moreover, the computation time for the correction step is negligible, since only simple arithmetic operations are involved for small 2D matrices.

In addition, during one full OS-SART iteration, the id-th sub-volume always remains in the memory of the id-th GPU. There is no need to frequently transfer large vectors between GPUs, which minimizes communcation times. Moreover, when solving the TV-proximal problem, since each GPU executed Algorithm 3 for one quarter of the data, the computation time required by four GPUs is approximately one quarter of the time required by a single GPU. The overhead and communication time between GPUs in this operation is minimal. Accordingly, the time reduction factor by adopting a multi-GPU scheme to solve the proposed OSSF-TV algorithm (and OSSF-TV-ℓ1 algorithm) is approximately equal to the number of GPUs employed. The above observations and conclusions generalize to the case where more than four GPUs are employed. This feature is highly attractive and suggests that reconstruction times can be readily reduced by using additional GPUs.

References

[1] M. Abramovitz and I.A. Stegun. Handbook of mathematical functions, 1972.

[2] Abulajiang Abudurexiti, Masashi Kameda, Eiichi Sato, Purkhet Abderyim, Toshiyuki Enomoto, Manabu Watanabe, Keitaro Hitomi, Etsuro Tanaka, Hidezo Mori, Toshiaki Kawai, Kiyomi Takahashi, Shigehiro Sato, Akira Ogawa, and Jun Onagawa. Demonstration of iodine k-edge imaging by use of an energy-discrimination x-ray computed tomography system with a cadmium telluride detector. *Radiological Physics and Technology*, 3:127–135, 2010. 10.1007/s12194-010-0088-8.

[3] M. A. Anastasio, M.A. Kupinski, and X. Pan. Noise propagation in diffraction tomography: Comparison of conventional algorithms with a new reconstruction algorithm. *Nuclear Science, IEEE Transactions on*, 45(4):2216–2223, 1998.

[4] M. A. Anastasio and X. Pan. Region-of-interest imaging in differential phase-contrast tomography. *Optics Letters*, 32(21):3167–3169, 2007.

[5] M.A. Anastasio, M.A. Kupinski, and Xiaochuan Pan. Noise propagation in diffraction tomography: comparison of conventional algorithms with a new reconstruction algorithm. *Nuclear Science, IEEE Transactions on*, 45(4):2216 –2223, aug 1998.

[6] Mark A Anastasio and Patrick La Riviere. *Emerging Imaging Technologies in Medicine*. CRC Press, 2012.

[7] Mark A Anastasio, Daxin Shi, Francesco De Carlo, and Xiaochuan Pan. Analytic image reconstruction in local phase-contrast tomography. *Physics in Medicine and biology*, 49(1):121, 2004.

[8] Mark A Anastasio, Qiaofeng Xu, and Daxin Shi. Multi-spectral intensity diffraction tomography. In *Optical Engineering+ Applications*, pages 707605–707605. International Society for Optics and Photonics, 2008.

[9] Mark A Anastasio, Qiaofeng Xu, and Daxin Shi. Multispectral intensity diffraction tomography: single material objects with variable densities. *JOSA A*, 26(2):403–412, 2009.

[10] AH Andersen and AC Kak. Simultaneous algebraic reconstruction technique (sart): a superior implementation of the art algorithm. *Ultrasonic imaging*, 6(1):81–94, 1984.

[11] Harry H. Barrett and Kyle J. Myers. *Foundations of Image Science*. John Wiley & Sons, Inc., Hoboken, New Jersey, 2004.

[12] H.H. Barrett, K.J. Myers, and S. Dhurjaty. *Foundations of image science*. Wiley-Interscience, second edition, 2003.

[13] Martin Bech, Torben H Jensen, Oliver Bunk, Tilman Donath, Christian David, Timm Weitkamp, Geraldine Le Duc, Alberto Bravin, Peter Cloetens, and Franz Pfeiffer. Advanced contrast modalities for x-ray radiology: Phase-contrast and dark-field imaging using a grating interferometer. *Zeitschrift fuer medizinische Physik*, 20(1):7–16, 2010.

[14] A. Beck and M. Teboulle. Fast gradient-based algorithms for constrained total variation image denoising and deblurring problems. *IEEE Trans. Image Process.*, 18(11):2419–2434, 2009.

[15] Amir Beck and Marc Teboulle. A fast iterative shrinkage-thresholding algorithm for linear inverse problems. *SIAM Journal on Imaging Sciences*, 2(1):183–202, 2009.

[16] Freek J Beekman and Chris Kamphuis. Ordered subset reconstruction for x-ray ct. *Physics in medicine and biology*, 46(7):1835, 2001.

[17] MJ Berger, JH Hubbell, SM Seltzer, J Chang, JS Coursey, R Sukumar, DS Zucker, and K Olsen. Xcom: Photon cross sections database. *NIST Standard reference database*, 8:87–3597, 1998.

[18] M. Bertero. *Introduction to inverse problems in imaging*. Taylor & Francis, 1998.

[19] Junguo Bian, Jeffrey H Siewerdsen, Xiao Han, Emil Y Sidky, Jerry L Prince, Charles A Pelizzari, and Xiaochuan Pan. Evaluation of sparse-view reconstruction from flat-panel-detector cone-beam ct. *Physics in Medicine and Biology*, 55(22):6575, 2010.

[20] Junguo Bian, Jeffrey H Siewerdsen, Xiao Han, Emil Y Sidky, Jerry L Prince, Charles A Pelizzari, and Xiaochuan Pan. Evaluation of sparse-view reconstruction from flat-panel-detector cone-beam ct. *Physics in Medicine and Biology*, 55(22):6575, 2010.

[21] U. Bonse and M. Hart. AN X-RAY INTERFEROMETER WITH LONG SEPARATED INTERFERING BEAM PATHS. *Applied Physics Letters*, 7(4):99–100, 1965.

[22] M. Born and E. Wolf. Principles of Optics, 7-th ed. *Cambridge U. Press, Cambridge, UK*, 1999.

[23] Stephen Boyd, Neal Parikh, Eric Chu, Borja Peleato, and Jonathan Eckstein. Distributed optimization and statistical learning via the alternating direction method of multipliers. *Foundations and Trends® in Machine Learning*, 3(1):1–122, 2011.

[24] J.G. Brankov, M.N. Wernick, Y. Yang, J. Li, C. Muehleman, Z. Zhong, and M. A. Anastasio. A computed tomography implementation of multiple-image radiography. *Medical physics*, 33:278, 2006.

[25] D.J. Brenner and E.J. Hall. Computed tomographyan increasing source of radiation exposure. *New England Journal of Medicine*, 357(22):2277–2284, 2007.

[26] Weixing Cai. *Feasibility study of phase-contrast cone beam CT imaging systems*. PhD thesis, University of Rochester, 2009.

[27] J. Cammin, J. S. Iwanczyk, and K. Taguchi. *Emerging Imaging Technologies in Medicine*, chapter Spectral/Photo-Counting Computed Tomography, pages 23–39. Imaging in Medical Diagnosis and Therapy. CRC Press, 2012.

[28] E.J. Candès, J. Romberg, and T. Tao. Robust uncertainty principles: Exact signal reconstruction from highly incomplete frequency information. *Information Theory, IEEE Transactions on*, 52(2):489–509, 2006.

[29] E.J. Candes, J.K. Romberg, and T. Tao. Stable signal recovery from incomplete and inaccurate measurements. *Communications on pure and applied mathematics*, 59(8):1207–1223, 2006.

[30] Yasmin Carter. Improved compressed sensing-based algorithm for sparse-view ct image reconstruction. *Computational and mathematical methods in medicine*, 2013, 2013.

[31] Yair Censor and Tommy Elfving. Block-iterative algorithms with diagonally scaled oblique projections for the linear feasibility problem. *SIAM Journal on Matrix Analysis and Applications*, 24(1):40–58, 2002.

[32] A. Chambolle. An algorithm for total variation minimization and applications. *J. Math. Imaging Vis.*, 20(1-2):89–97, 2004.

[33] AK Chaniotis and D. Poulikakos. High order interpolation and differentiation using b-splines. *Journal of Computational Physics*, 197(1):253–274, 2004.

[34] D. Chapman, W. Thomlinson, RE Johnston, D. Washburn, E. Pisano, N. Gmür, Z. Zhong, R. Menk, F. Arfelli, and D. Sayers. Diffraction enhanced x-ray imaging. *Physics in Medicine and Biology*, 42:2015, 1997.

[35] Guang-Hong Chen, Nicholas Bevins, Joseph Zambelli, and Zhihua Qi. Small-angle scattering computed tomography (sas-ct) using a talbot-lau interferometer and a rotating anode x-ray tube: theory and experiments. *Optics express*, 18(12):12960–12970, 2010.

[36] Kihwan Choi, Jing Wang, Lei Zhu, Tae-Suk Suh, Stephen Boyd, and Lei Xing. Compressed sensing based cone-beam computed tomography reconstruction with a first-order method. *Medical physics*, 37(9):5113, 2010.

[37] P.L. Combettes and J.C. Pesquet. A proximal decomposition method for solving convex variational inverse problems. *Inverse problems*, 24(6):065014, 2008.

[38] D. P. Cormode, E. Roessl, A. Thran, T. Skajaa, R. E. Gordon, J.-P. Schlomka, V. Fuster, E. A. Fisher, W. J. M. Mulder, R. Proksa, and Z. A. Fayad. Atherosclerotic plaque composition: Analysis with multicolor CT and targeted gold nanoparticles. *Radiology*, 256(3):774–782, 2010.

[39] G. Cowan. *Statistical Data Analysis*. Oxford University Press, 1998.

[40] K. Creath. V phase-measurement interferometry techniques. *Progress in Optics*, 26:349–393, 1988.

[41] Y. Zou D. Shi and A. Zamyatin. Weighted simultaneous algebraic reconstruction techniques. In *11 International Meeting onFully Three-Dimensional Image Reconstruction in Radiology and Nuclear Medicine*, page 157, 2011.

[42] Ingrid Daubechies, Michel Defrise, and Christine De Mol. An iterative thresholding algorithm for linear inverse problems with a sparsity constraint. *Communications on pure and applied mathematics*, 57(11):1413–1457, 2004.

[43] C David, B Nöhammer, H_H Solak, and E Ziegler. Differential x-ray phase contrast imaging using a shearing interferometer. *Applied physics letters*, 81(17):3287–3289, 2002.

[44] TJ Davis, D. Gao, TE Gureyev, AW Stevenson, and SW Wilkins. Phase-contrast imaging of weakly absorbing materials using hard X-rays. *Nature*, 373(6515):595–598, 1995.

[45] FA Dilmanian, Z. Zhong, B. Ren, XY Wu, LD Chapman, I. Orion, and WC Thomlinson. Computed tomography of x-ray index of refraction using the diffraction enhanced imaging method. *Physics in medicine and biology*, 45:933, 2000.

[46] James T Dobbins III. Tomosynthesis imaging: at a translational crossroads. *Medical physics*, 36(6):1956–1967, 2009.

[47] James T Dobbins III and Devon J Godfrey. Digital x-ray tomosynthesis: current state of the art and clinical potential. *Physics in medicine and biology*, 48(19):R65, 2003.

[48] Joyita Dutta, Sangtae Ahn, Changqing Li, Simon R Cherry, and Richard M Leahy. Joint l1 and total variation regularization for fluorescence molecular tomography. *Physics in medicine and biology*, 57(6):1459, 2012.

[49] M. Engelhardt, J. Baumann, M. Schuster, C. Kottler, F. Pfeiffer, O. Bunk, and C. David. High-resolution differential phase contrast imaging using a magnifying projection geometry with a microfocus x-ray source. *Applied Physics Letters*, 90:224101, 2007.

[50] Hakan Erdogan and Jeffrey A Fessler. Ordered subsets algorithms for transmission tomography. *Physics in medicine and biology*, 44(11):2835, 1999.

[51] G.W. Faris and R.L. Byer. Three-dimensional beam-deflection optical tomography of a supersonic jet. *Applied Optics*, 27(24):5202–5212, 1988.

[52] R. Fatehi, M. Fayazbakhsh, and MT Manzari. On discretization of second-order derivatives in smoothed particle hydrodynamics. *International Journal of Natural and Applied Sciences. v3 i1*, pages 50–53, 2008.

[53] J. A. Fessler. Mean and variance of implicitly defined biased estimators (such as penalized maximum likelihood): Applications to tomography. *IEEE Trans. Image Process.*, 5(3):493–506, 1996.

[54] J.A. Fessler. Penalized weighted least-squares image reconstruction for positron emission tomography. *Medical Imaging, IEEE Transactions on*, 13(2):290–300, 1994.

[55] J.A. Fessler, I. Elbakri, P. Sukovic, and N.H. Clinthorne. Maximum-likelihood dual-energy tomographicimage reconstruction. In *Proc. SPIE*, volume 4684, pages 38–49, 2002.

[56] Jeffrey A Fessler. Mean and variance of implicitly defined biased estimators (such as penalized maximum likelihood): Applications to tomography. *Image Processing, IEEE Transactions on*, 5(3):493–506, 1996.

[57] Jeffrey A Fessler and Scott D Booth. Conjugate-gradient preconditioning methods for shift-variant pet image reconstruction. *Image Processing, IEEE Transactions on*, 8(5):688–699, 1999.

[58] Jeffrey A Fessler and W Leslie Rogers. Spatial resolution properties of penalized-likelihood image reconstruction: space-invariant tomographs. *Image Processing, IEEE Transactions on*, 5(9):1346–1358, 1996.

[59] S. Feuerlein, E. Roessl, R. Proksa, G. Martens, O. Klass, M. Jeltsch, V. Rasche, H.-J. Brambs, M. H. K. Hoffmann, and J.-P. Schlomka. Multienergy photon-counting K-edge imaging: Potential for improved luminal depiction in vascular imaging. *Radiology*, 249(3):1010–1016, 2008.

[60] S. Fiedler, A. Bravin, J. Keyriläinen, M. Fernández, P. Suortti, W. Thomlinson, M. Tenhunen, P. Virkkunen, and ML Karjalainen-Lindsberg. Imaging lobular breast

carcinoma: comparison of synchrotron radiation dei-ct technique with clinical ct, mammography and histology. *Physics in medicine and biology*, 49:175, 2004.

[61] Mário AT Figueiredo, Robert D Nowak, and Stephen J Wright. Gradient projection for sparse reconstruction: Application to compressed sensing and other inverse problems. *Selected Topics in Signal Processing, IEEE Journal of*, 1(4):586–597, 2007.

[62] Daniel Gabay. Chapter ix applications of the method of multipliers to variational inequalities. *Studies in mathematics and its applications*, 15:299–331, 1983.

[63] Hao Gao, Hengyong Yu, Stanley Osher, and Ge Wang. Multi-energy ct based on a prior rank, intensity and sparsity model (prism). *Inverse problems*, 27(11):115012, 2011.

[64] Tsutomu Gomi, Hiroshi Hirano, Masahiro Nakajima, and Tokuo Umeda. X-ray digital linear tomosynthesis imaging. *Journal of Biomedical Science & Engineering*, 4(6), 2011.

[65] Joseph W Goodman. *Introduction to Fourier optics*. Roberts and Company Publishers, 2005.

[66] A Groso, R Abela, and M Stampanoni. Implementation of a fast method for high resolution phase contrast tomography. *Optics express*, 14(18):8103–8110, 2006.

[67] Huaiqun Guan and Richard Gordon. A projection access order for speedy convergence of art (algebraic reconstruction technique): a multilevel scheme for computed tomography. *Physics in medicine and biology*, 39(11):2005, 1999.

[68] Huifeng Guan, Qiaofeng Xu, Alfred Garson, and Mark A Anastasio. Investigation of in-line x-ray phase-contrast tomosynthesis. In *SPIE Medical Imaging*, pages 90330H–90330H. International Society for Optics and Photonics, 2014.

[69] TE Gureyev, S. Mayo, SW Wilkins, D. Paganin, and AW Stevenson. Quantitative in-line phase-contrast imaging with multienergy x rays. *Physical Review Letters*, 86(25):5827–5830, 2001.

[70] Jeffrey C Hammonds, Ronald R Price, Edwin F Donnelly, and David R Pickens. Phase-contrast digital tomosynthesis. *Medical physics*, 38(5):2353–2358, 2011.

[71] X. Han, J. Bian, D.R. Eaker, T.L. Kline, E. Y. Sidky, E.L. Ritman, and X. Pan. Algorithm-enabled low-dose micro-CT imaging. *Medical Imaging, IEEE Transactions on*, 30(3):606–620, 2011.

[72] Xiao Han, Junguo Bian, Erik L Ritman, Emil Y Sidky, and Xiaochuan Pan. Optimization-based reconstruction of sparse images from few-view projections. *Physics in Medicine and Biology*, 57(16):5245, 2012.

[73] D. Hanselman and B. Littlefield. *Mastering Matlab 7*. Pearson Education, 2005.

[74] Peng He, Biao Wei, Wenxiang Cong, and Ge Wang. Optimization of k-edge imaging with spectral ct. *Medical physics*, 39:6572, 2012.

[75] Gabor T Herman and Lorraine B Meyer. Algebraic reconstruction techniques can be made computationally efficient [positron emission tomography application]. *Medical Imaging, IEEE Transactions on*, 12(3):600–609, 1993.

[76] G.T. Herman. *Fundamentals of Computerized Tomography: Image Reconstruction from Projections*. Springer Verlag, 2009.

[77] Junzhou Huang, Shaoting Zhang, and Dimitris Metaxas. Efficient mr image reconstruction for compressed mr imaging. *Medical Image Analysis*, 15(5):670–679, 2011.

[78] Z.F. Huang, K.J. Kang, L. Zhang, Z.Q. Chen, F. Ding, Z.T. Wang, and Q.G. Fang. Alternative method for differential phase-contrast imaging with weakly coherent hard x rays. *Physical Review A*, 79(1):013815, 2009.

[79] H Malcolm Hudson and Richard S Larkin. Accelerated image reconstruction using ordered subsets of projection data. *Medical Imaging, IEEE Transactions on*, 13(4):601–609, 1994.

[80] Wonseok Huh and J.A. Fessler. Iterative image reconstruction for dual-energy x-ray ct using regularized material sinogram estimates. In *Biomedical Imaging: From Nano to Macro, 2011 IEEE International Symposium on*, pages 1512 –1515, 30 2011-april 2 2011.

[81] Filip Jacobs, Erik Sundermann, Bjorn De Sutter, Mark Christiaens, and Ignace Lemahieu. A fast algorithm to calculate the exact radiological path through a pixel or voxel space. *Journal of computing and information technology*, 6(1):89–94, 1998.

[82] Xun Jia, Yifei Lou, John Lewis, Ruijiang Li, Xuejun Gu, Chunhua Men, William Y Song, and Steve B Jiang. Gpu-based fast low-dose cone beam ct reconstruction via total variation. *Journal of X-Ray Science and Technology*, 19(2):139–154, 2011.

[83] Min Jiang and Ge Wang. Convergence of the simultaneous algebraic reconstruction technique (sart). *Image Processing, IEEE Transactions on*, 12(8):957–961, 2003.

[84] Ming Jiang and Ge Wang. Convergence studies on iterative algorithms for image reconstruction. *Medical Imaging, IEEE Transactions on*, 22(5):569–579, 2003.

[85] Jakob Heide Jørgensen, Tobias Lindstrøm Jensen, Per Christian Hansen, Søren Holdt Jensen, Emil Y Sidky, and Xiaochuan Pan. Accelerated gradient methods for total-variation-based ct image reconstruction. *arXiv preprint arXiv:1105.4002*, 2011.

[86] A.C. Kak and M. Slaney. *Principles of computerized tomographic imaging*. IEEE Service Center, Piscataway, NJ, 1988.

[87] D Kim, D Pal, JB Thibault, and JA Fessler. Accelerating ordered subsets image reconstruction for x-ray ct using spatially nonuniform optimization transfer. *Medical Imaging, IEEE Transactions on*, 32(11):1965–1978, 2013.

[88] Donghwan Kim, Sathish Ramani, and Jeffrey A Fessler. Ordered subsets with momentum for accelerated x-ray ct image reconstruction. In *Acoustics, Speech and Signal Processing (ICASSP), 2013 IEEE International Conference on*, pages 920–923. IEEE, 2013.

[89] T. Köhler, B. Brendel, and E. Roessl. Iterative reconstruction for differential phase contrast imaging using spherically symmetric basis functions. *Medical Physics*, 38:4542, 2011.

[90] T. Köhler, B. Brendel, and E. Roessl. Iterative reconstruction for differential phase contrast imaging using spherically symmetric basis functions. *Medical Physics*, 38:4542, 2011.

[91] T. Köhler, K.J. Engel, and E. Roessl. Noise properties of grating-based x-ray phase contrast computed tomography. *Medical Physics*, 38:S106, 2011.

[92] I. Koyama, A. Momose, J. Wu, T.T. Lwin, and T. Takeda. Biological imaging by x-ray phase tomography using diffraction-enhanced imaging. *Japanese journal of applied physics. Pt. 1, Regular papers & short notes*, 44(11):8219–8221, 2005.

[93] R. A. Kruger, S. J. Riederer, and C. A. Mistretta. Relative properties of tomography, K-edge imaging, and K-edge tomography. *Med. Phys.*, 4(3):244–249, 1977.

[94] Patrick J La Rivière. Penalized-likelihood sinogram smoothing for low-dose ct. *Medical physics*, 32:1676, 2005.

[95] RA Lewis. Medical phase contrast x-ray imaging: current status and future prospects. *Physics in medicine and biology*, 49(16):3573, 2004.

[96] R.M. Lewitt. Multidimensional digital image representations using generalized Kaiser-Bessel window functions. *JOSA A*, 7(10):1834–1846, 1990.

[97] R.M. Lewitt. Alternatives to voxels for image representation in iterative reconstruction algorithms. *Physics in Medicine and Biology*, 37:705, 1992.

[98] Yanlan Liu, Kelong Ai, Jianhua Liu, Qinghai Yuan, Yangyang He, and Lehui Lu. A high-performance ytterbium-based nanoparticulate contrast agent for in vivo x-ray computed tomography imaging. *Angewandte Chemie International Edition*, 51(6):1437–1442, 2012.

[99] S.C.B. Lo. Strip and line path integrals with a square pixel matrix: A unified theory for computational CT projections. *Medical Imaging, IEEE Transactions on*, 7(4):355–363, 1988.

[100] Michael Lustig, David Donoho, and John M Pauly. Sparse mri: The application of compressed sensing for rapid mr imaging. *Magnetic resonance in medicine*, 58(6):1182–1195, 2007.

[101] J. Ma. Total variation smoothed maximum penalized likelihood tomographic reconstruction with positivity constraints. In *Biomedical Imaging: From Nano to Macro, 2011 IEEE International Symposium on*, pages 1774–1777. IEEE, 2011.

[102] Shiqian Ma, Wotao Yin, Yin Zhang, and Amit Chakraborty. An efficient algorithm for compressed mr imaging using total variation and wavelets. In *Computer Vision and Pattern Recognition, 2008. CVPR 2008. IEEE Conference on*, pages 1–8. IEEE, 2008.

[103] A. Maksimenko, M. Ando, S. Hiroshi, and T. Yuasa. Computed tomographic reconstruction based on x-ray refraction contrast. *Applied Physics Letters*, 86(12):124105–124105, 2005.

[104] Anton Maksimenko, Tetsuya Yuasa, Masami Ando, and Eiko Hashimoto. Refraction-based tomosynthesis: Proof of the concept. *Applied Physics Letters*, 91(23):234108, 2007.

[105] S. Matej and R.M. Lewitt. Image representation and tomographic reconstruction using spherically-symmetric volume elements. In *Nuclear Science Symposium and Medical Imaging Conference, 1992., Conference Record of the 1992 IEEE*, pages 1191–1193. IEEE, 1992.

[106] S. Matej and R.M. Lewitt. Practical considerations for 3-D image reconstruction using spherically symmetric volume elements. *Medical Imaging, IEEE Transactions on*, 15(1):68–78, 1996.

[107] S.A. McDonald, F. Marone, C. Hintermuller, G. Mikuljan, C. David, F. Pfeiffer, and M. Stampanoni. Advanced phase-contrast imaging using a grating interferometer. *Journal of Synchrotron Radiation*, 16(4):562–572, 2009.

[108] A. Momose. Demonstration of phase-contrast X-ray computed tomography using an X-ray interferometer. *Nuclear Instruments and Methods in Physics Research Section A: Accelerators, Spectrometers, Detectors and Associated Equipment*, 352(3):622–628, 1995.

[109] A. Momose. Phase-sensitive imaging and phase tomography using x-ray interferometers. *Optics Express*, 11(19):2303–2314, 2003.

[110] A. Momose. Recent advances in X-ray phase imaging. *Japanese Journal of Applied Physics*, 44(9A):6355, 2005.

[111] A. Momose and J. Fukuda. Phase-contrast radiographs of nonstained rat cerebellar specimen. *Medical Physics*, 22:375, 1995.

[112] A. Momose, S. Kawamoto, I. Koyama, Y. Hamaishi, K. Takai, and Y. Suzuki. Demonstration of X-ray Talbot interferometry. *Japanese Journal of Applied Physics Part 2 Letters*, 42(7B; ISSU 393):866–868, 2003.

[113] A. Momose, T. Takeda, Y. Itai, and K. Hirano. Phase–contrast X–ray computed tomography for observing biological soft tissues. *Nature Medicine*, 2(4):473–475, 1996.

[114] Atsushi Momose, Wataru Yashiro, Yoshihiro Takeda, Yoshio Suzuki, and Tadashi Hattori. Phase tomography by x-ray talbot interferometry for biological imaging. *Japanese Journal of Applied Physics*, 45(6A):5254–5262, 2006.

[115] J.J. Monaghan. Smoothed particle hydrodynamics. *Reports on Progress in Physics*, 68:1703, 2005.

[116] Klaus Mueller, Roni Yagel, and J. Fredrick Cornhill. The weighted-distance scheme: a globally optimizing projection ordering method for art. *Medical Imaging, IEEE Transactions on*, 16(2):223–230, 1997.

[117] GR Myers, SC Mayo, TE Gureyev, DM Paganin, and SW Wilkins. Polychromatic cone-beam phase-contrast tomography. *Physical Review A*, 76(4):045804, 2007.

[118] F. Natterer and F. Wübbeling. *Mathematical Methods in Image Reconstruction*. Monographs on Mathematical Modeling and Computation. SIAM, 2001.

[119] Hung Nien and Jeffrey A Fessler. Combining augmented lagrangian method with ordered subsets for x-ray ct reconstruction.

[120] Masih Nilchian, Cédric Vonesch, Stamatios Lefkimmiatis, Peter Modregger, Marco Stampanoni, and Michael Unser. Constrained regularized reconstruction of x-ray-dpci tomograms with weighted-norm. *Optics Express*, 21(26):32340–32348, 2013.

[121] Masih Nilchian, Cédric Vonesch, Peter Modregger, Marco Stampanoni, and Michael Unser. Fast iterative reconstruction of differential phase contrast x-ray tomograms. *Optics express*, 21(5):5511–5528, 2013.

[122] Tianye Niu, Xiaojing Ye, Quentin Fruhauf, Michael Petrongolo, and Lei Zhu. Accelerated barrier optimization compressed sensing (abocs) for ct reconstruction with improved convergence. *Physics in medicine and biology*, 59(7):1801, 2014.

[123] Tianye Niu and Lei Zhu. Accelerated barrier optimization compressed sensing (abocs) reconstruction for cone-beam ct: Phantom studies. *Medical physics*, 39(7):4588, 2012.

[124] KA Nugent, TE Gureyev, DF Cookson, D. Paganin, and Z. Barnea. Quantitative phase imaging using hard x rays. *Physical review letters*, 77(14):2961–2964, 1996.

[125] T. Obi, S. Matej, R.M. Lewitt, and G.T. Herman. 2.5-D simultaneous multislice reconstruction by series expansion methods from fourier-rebinned pet data. *Medical Imaging, IEEE Transactions on*, 19(5):474–484, 2000.

[126] DM Paganin and X. Coherent. ray optics, 2006.

[127] D. Pan, E. Roessl, J.-P. Schlomka, D. C. Shelton, A. Senpan, M. J. Scott, J. S. Allen, H. Zhang, G. Hu, P. J. Gaffney, E. T. Choi, V. Rasche, S. A. Wickline, R. Proksa, and G. M. Lanza. Computed tomography in color: NanoK-enhanced spectral CT molecular imaging. *Angew. Chem., Int. Ed.*, 49(50):9635–9639, 2010.

[128] Dipanjan Pan, Carsten O Schirra, Angana Senpan, Anne H Schmieder, Allen J Stacy, Ewald Roessl, Axel Thran, Samuel A Wickline, Roland Proska, and Gregory M Lanza. An early investigation of ytterbium nanocolloids for selective and quantitative "multicolor" spectral ct imaging. *ACS Nano*, 6(4):3364–3370, Apr 2012.

[129] X. Pan, E. Y. Sidky, and M. Vannier. Why do commercial CT scanners still employ traditional, filtered back-projection for image reconstruction? *Inverse problems*, 25:123009, 2009.

[130] Justin C Park, Bongyong Song, Jin Sung Kim, Sung Ho Park, Ho Kyung Kim, Zhaowei Liu, Tae Suk Suh, and William Y Song. Fast compressed sensing-based cbct reconstruction using barzilai-borwein formulation for application to on-line igrt. *Medical Physics*, 39:1207, 2012.

[131] KM Pavlov, CM Kewish, JR Davis, and MJ Morgan. A new theoretical approach to x-ray diffraction tomography. *Journal of Physics D: Applied Physics*, 33:1596, 2000.

[132] F Pfeiffer, Martin Bech, O Bunk, Philipp Kraft, EF Eikenberry, Ch Brönnimann, C Grünzweig, and C David. Hard-x-ray dark-field imaging using a grating interferometer. *Nature materials*, 7(2):134–137, 2008.

[133] F. Pfeiffer, T. Weitkamp, O. Bunk, and C. David. Phase retrieval and differential phase-contrast imaging with low-brilliance X-ray sources. *Nature Physics*, 2(4):258–261, 2006.

[134] Z. Qi, J. Zambelli, N. Bevins, and G.H. Chen. A novel method to reduce data acquisition time in differential phase contrast: computed tomography using compressed sensing. In *Proceedings of SPIE*, volume 7258, page 72584A, 2009.

[135] Sathish Ramani and Jeffrey A Fessler. A splitting-based iterative algorithm for accelerated statistical x-ray ct reconstruction. *Medical Imaging, IEEE Transactions on*, 31(3):677–688, 2012.

[136] Ingrid Reiser. X-ray tomosynthesis. In Mark A Anastasio and Patrick La Riviere, editors, *Emerging imaging technologies in medicine*, pages 3–21. CRC Press, Florida, 2012.

[137] V. Revol, C. Kottler, R. Kaufmann, U. Straumann, and C. Urban. Noise analysis of grating-based x-ray differential phase contrast imaging. *Review of Scientific Instruments*, 81:073709, 2010.

[138] Ludwig Ritschl, Frank Bergner, Christof Fleischmann, and Marc Kachelrieß. Improved total variation-based ct image reconstruction applied to clinical data. *Physics in Medicine and Biology*, 56(6):1545, 2011.

[139] E Roessl and C Herrmann. Cramér–rao lower bound of basis image noise in multiple-energy x-ray imaging. *Physics in medicine and biology*, 54(5):1307, 2009.

[140] E. Roessl and C. Herrmann. Cramér-Rao lower bound of basis image noise in multiple-energy x-ray imaging. *Phys. Med. Biol.*, 54(5):1307–1318, 2009.

[141] E. Roessl and R. Proksa. K-edge imaging in x-ray computed tomography using multi-bin photon counting detectors. *Phys. Med. Biol.*, 52(15):4679–4696, 2007.

[142] Ewald Roessl, Bernhard Brendel, Klaus-Juergen Engel, Jens-Peter Schlomka, Axel Thran, and Roland Proksa. Sensitivity of photon-counting based k-edge imaging in x-ray computed tomography. *IEEE transactions on medical imaging*, 30(9):1678, 2011.

[143] JP Rolland and H.H. Barrett. Effect of random background inhomogeneity on observer detection performance. *Journal of the Optical Society of America A*, 9(5):649–658, 1992.

[144] Ken Sauer and Charles Bouman. A local update strategy for iterative reconstruction from projections. *Signal Processing, IEEE Transactions on*, 41(2):534–548, 1993.

[145] C Schirra, E Roessl, T Koehler, B Brendel, A Thran, D Pan, M Anastasio, and R Proksa. Statistical reconstruction of material decomposed data in spectral ct. *IEEE transactions on medical imaging*, 2013.

[146] C. O. Schirra, E. Roessl, T. Koehler, B. Brendel, A. Thran, and R. Proksa. Maximum likelihood CT reconstruction form material-decomposed sinograms using fisher information. In *2011 IEEE Nuclear Science Symposium Conference Record*, pages 4063–4065, 2011.

[147] J. P. Schlomka, E. Roessl, R. Dorscheid, S. Dill, G. Martens, T. Istel, C. Bumer, C. Herrmann, R. Steadman, G. Zeitler, A. Livne, and R. Proksa. Experimental feasibility of multi-energy photon-counting K-edge imaging in pre-clinical computed tomography. *Physics in Medicine and Biology*, 53(15):4031–4047, Aug 2008.

[148] R.L. Siddon. Fast calculation of the exact radiological path for a three-dimensional CT array. *Medical Physics*, 12:252, 1985.

[149] E. Y. Sidky, C.M. Kao, and X. Pan. Accurate image reconstruction from few-views and limited-angle data in divergent-beam CT. *Journal of X-Ray Science and Technology*, 14(2):119–139, 2006.

[150] E. Y. Sidky, C.M. Kao, and X. Pan. Effect of the data constraint on few-view, fan-beam CT image reconstruction by TV minimization. In *Nuclear Science Symposium Conference Record, 2006. IEEE*, volume 4, pages 2296–2298. IEEE, 2006.

[151] E. Y. Sidky and X. Pan. Image reconstruction in circular cone-beam computed tomography by constrained, total-variation minimization. *Physics in medicine and biology*, 53:4777, 2008.

[152] Emil Y Sidky, Xiaochuan Pan, Ingrid S Reiser, Robert M Nishikawa, Richard H Moore, and Daniel B Kopans. Enhanced imaging of microcalcifications in digital breast tomosynthesis through improved image-reconstruction algorithms. *Medical physics*, 36(11):4920–4932, 2009.

[153] A. Snigirev, I. Snigireva, V. Kohn, S. Kuznetsov, and I. Schelokov. On the possibilities of x-ray phase contrast microimaging by coherent high-energy synchrotron radiation. *Review of scientific instruments*, 66(12):5486–5492, 1995.

[154] J. Stricker. Analysis of 3-d phase objects by moiré deflectometry. *Applied Optics*, 23(20):3657–3659, 1984.

[155] Y. Takeda, W. Yashiro, Y. Suzuki, S. Aoki, T. Hattori, and A. Momose. X-ray phase imaging with single phase grating. *Japanese Journal of Applied Physics Part 2 Letters*, 46(1/3):89, 2007.

[156] Henry Fox Talbot. Lxxvi. facts relating to optical science. no. iv. *The London and Edinburgh Philosophical Magazine and Journal of Science*, 9(56):401–407, 1836.

[157] Jun Tan, H Harold Li, Eric Klein, Hua Li, Parag Parikh, and Deshan Yang. Physical phantom studies of helical cone-beam ct with exact reconstruction. *Medical Physics*, 39:4695, 2012.

[158] J.-B. Thibault, K. D. Sauer, C. A. Bouman, and J. Hsieh. A three-dimensional statistical approach to improved image quality for multislice helical CT. *Med. Phys.*, 34(11):4526–4544, 2007.

[159] R. Van de Walle, H.H. Barrett, K.J. Myers, MI Aitbach, B. Desplanques, A.F. Gmitro, J. Cornelis, and I. Lemahieu. Reconstruction of MR images from data acquired on a general nonregular grid by pseudoinverse calculation. *IEEE transactions on medical imaging*, 19(12):1160–1167, 2000.

[160] M.C. van Dijke. Iterative methods in image reconstruction,. *Ph.D. Dissertation*, 1992.

[161] Alexander I Veress, William Paul Segars, Jeffrey A Weiss, Benjamin MW Tsui, and Grant T Gullberg. Normal and pathological ncat image and phantom data based on physiologically realistic left ventricle finite-element models. *Medical Imaging, IEEE Transactions on*, 25(12):1604–1616, 2006.

[162] DJ Vine, DM Paganin, KM Pavlov, J Kraeusslich, O Wehrhan, I Uschmann, and E Foerster. Analyzer-based phase contrast imaging and phase retrieval using a rotating anode x-ray source. *Applied Physics Letters*, 91(25):254110, 2007.

[163] David Wang, Robert Tamburo, and George Stetten. Cumulative gaussian curve fitter for boundary parameterization. *Insight J*, 2005.

[164] Ge Wang and Ming Jiang. Ordered-subset simultaneous algebraic reconstruction techniques (os-sart). *Journal of X-ray Science and Technology*, 12(3):169–178, 2004.

[165] Jing Wang, Huaiqun Guan, and Timothy Solberg. Inverse determination of the penalty parameter in penalized weighted least-squares algorithm for noise reduction of low-dose cbct. *Medical Physics*, 38:4066, 2011.

[166] Z. Wang, A. C. Bovik, H. R. Sheikh, and E. P. Simoncelli. Image quality assessment: From error visibility to structural similarity. *Image Processing, IEEE Transactions on*, 13(4):600–612, 2004.

[167] Zhou Wang, Alan C Bovik, Hamid R Sheikh, and Eero P Simoncelli. Image quality assessment: from error visibility to structural similarity. *Image Processing, IEEE Transactions on*, 13(4):600–612, 2004.

[168] Thomas Weber, Peter Bartl, Florian Bayer, Jürgen Durst, Wilhelm Haas, Thilo Michel, Andre Ritter, and Gisela Anton. Noise in x-ray grating-based phase-contrast imaging. *Medical physics*, 38(7):4133–4140, 2011.

[169] T. Weitkamp, A. Diaz, C. David, F. Pfeiffer, M. Stampanoni, P. Cloetens, and E. Ziegler. X-ray phase imaging with a grating interferometer. *Optics Express*, 13(16):6296–6304, 2005.

[170] M.N. Wernick, O. Wirjadi, D. Chapman, Z. Zhong, N.P. Galatsanos, Y. Yang, J.G. Brankov, O. Oltulu, M.A. Anastasio, and C. Muehleman. Multiple-image radiography. *Physics in Medicine and Biology*, 48:3875, 2003.

[171] SW Wilkins, TE Gureyev, D. Gao, A. Pogany, and AW Stevenson. Phase-contrast imaging using polychromatic hard X-rays. *Nature*, 384(6607):335–338, 1996.

[172] Di Wu, Hui Miao, Yuhua Li, Xizeng Wu, and Hong Liu. In-plane spatial resolution measurements of a phase-contrast tomosynthesis prototype. In *SPIE BiOS*, pages 82240D–82240D. International Society for Optics and Photonics, 2012.

[173] Xizeng Wu and Hong Liu. Clinical implementation of x-ray phase-contrast imaging: Theoretical foundations and design considerations. *Medical physics*, 30(8):2169–2179, 2003.

[174] Q Xu, D Yang, J Tan, and M Anastasio. Su-f-brcd-09: Total variation (tv) based fast convergent iterative cbct reconstruction with gpu acceleration. *Medical physics*, 39(6):3857, 2012.

[175] Qiaofeng Xu, Alex Sawatzky, and Mark A Anastasio. A multi-channel image reconstruction method for grating-based x-ray phase-contrast computed tomography. In *SPIE Medical Imaging*, pages 90330D–90330D. International Society for Optics and Photonics, 2014.

[176] Qiaofeng Xu, Alex Sawatzky, Mark A Anastasio, and Carsten O Schirra. Sparsity-regularized image reconstruction of decomposed k-edge data in spectral CT. *Physics in Medicine and Biology*, accepted, to be appear, 2014.

[177] Qiaofeng Xu, Emil Y Sidky, Xiaochuan Pan, Marco Stampanoni, Peter Modregger, and Mark A Anastasio. Investigation of discrete imaging models and iterative image reconstruction in differential x-ray phase-contrast tomography. *Optics express*, 20(10):10724, 2012.

[178] PS Yadav, Yogesh Kashyap, PS Sarkar, Amar Sinha, and BK Godwal. Study of phase contrast imaging for carbon fiber, polystyrene and lung tissue using monochromatic and polychromatic x-ray sources. *Nuclear Instruments and Methods in Physics Research Section A: Accelerators, Spectrometers, Detectors and Associated Equipment*, 564(1):496–505, 2006.

[179] Wenkao Yang, Jing Wang, and Jing Guo. A novel algorithm for satellite images fusion based on compressed sensing and pca. *Mathematical Problems in Engineering*, 2013, 2013.

[180] J. Zhang, M.A. Anastasio, P.J. La Rivière, and L.V. Wang. Effects of different imaging models on least-squares image reconstruction accuracy in photoacoustic tomography. *Medical Imaging, IEEE Transactions on*, 28(11):1781–1790, 2009.

[181] Li Zhang, MingLi Jin, Zhifeng Huang, Yongshun Xiao, Hongxia Yin, Zhenchang Wang, and Tiqiao Xiao. Phase-contrast tomosynthetic experiment on biological samples with

synchrotron radiation. In *Nuclear Science Symposium Conference Record (NSS/MIC), 2010 IEEE*, pages 1619–1621. IEEE, 2010.

[182] R. Zhang, J.-B. Thibault, C. A. Bouman, K. D. Sauer, and J. Hsieh. A model-based iterative algorithm for dual-energy x-ray CT reconstruction. In *Proceedings of the 2nd International Conference on Image Formation in X-Ray Computed Tomography*, pages 439–443, 2012.

[183] Yiheng Zhang, Heang-Ping Chan, Berkman Sahiner, Jun Wei, Mitchell M Goodsitt, Lubomir M Hadjiiski, Jun Ge, and Chuan Zhou. A comparative study of limited-angle cone-beam reconstruction methods for breast tomosynthesis. *Medical physics*, 33(10):3781–3795, 2006.

[184] S.A. Zhou and A. Brahme. Development of phase-contrast X-ray imaging techniques and potential medical applications. *Physica Medica*, 24(3):129–148, 2008.

[185] Lei Zhu and Lei Xing. Search for imrt inverse plans with piecewise constant fluence maps using compressed sensing techniques. *Medical physics*, 36:1895, 2009.

[186] P. Zhu, K. Zhang, Z. Wang, Y. Liu, X. Liu, Z. Wu, S.A. McDonald, F. Marone, and M. Stampanoni. Low-dose, simple, and fast grating-based x-ray phase-contrast imaging. *Proceedings of the National Academy of Sciences*, 107(31):13576, 2010.

[187] Adam M Zysk, Alfred B Garson, Qiaofeng Xu, Eric M Brey, Wei Zhou, Jovan G Brankov, Miles N Wernick, Jerome R Kuszak, and Mark A Anastasio. Nondestructive volumetric imaging of tissue microstructure with benchtop x-ray phase-contrast tomography and critical point drying. *Biomedical optics express*, 3(8):1924–1932, 2012.

[188] Adam M Zysk, Robert W Schoonover, Qiaofeng Xu, and Mark A Anastasio. Framework for computing the spatial coherence effects of polycapillary x-ray optics. *Optics express*, 20(4):3975–3982, 2012.

[189] Adam M Zysk, Qiaofeng Xu, Luis de Sisternes, Jovan G Brankov, Miles N Wernick, and Mark A Anastasio. Analysis of the spectrum in phase-contrast mammography. In *SPIE Medical Imaging*, pages 72584E–72584E. International Society for Optics and Photonics, 2009.